Fabrication and Characterization of a Dimer Josephson Junction Parametric Amplifier

Master of Science Thesis

Loek van Everdingen

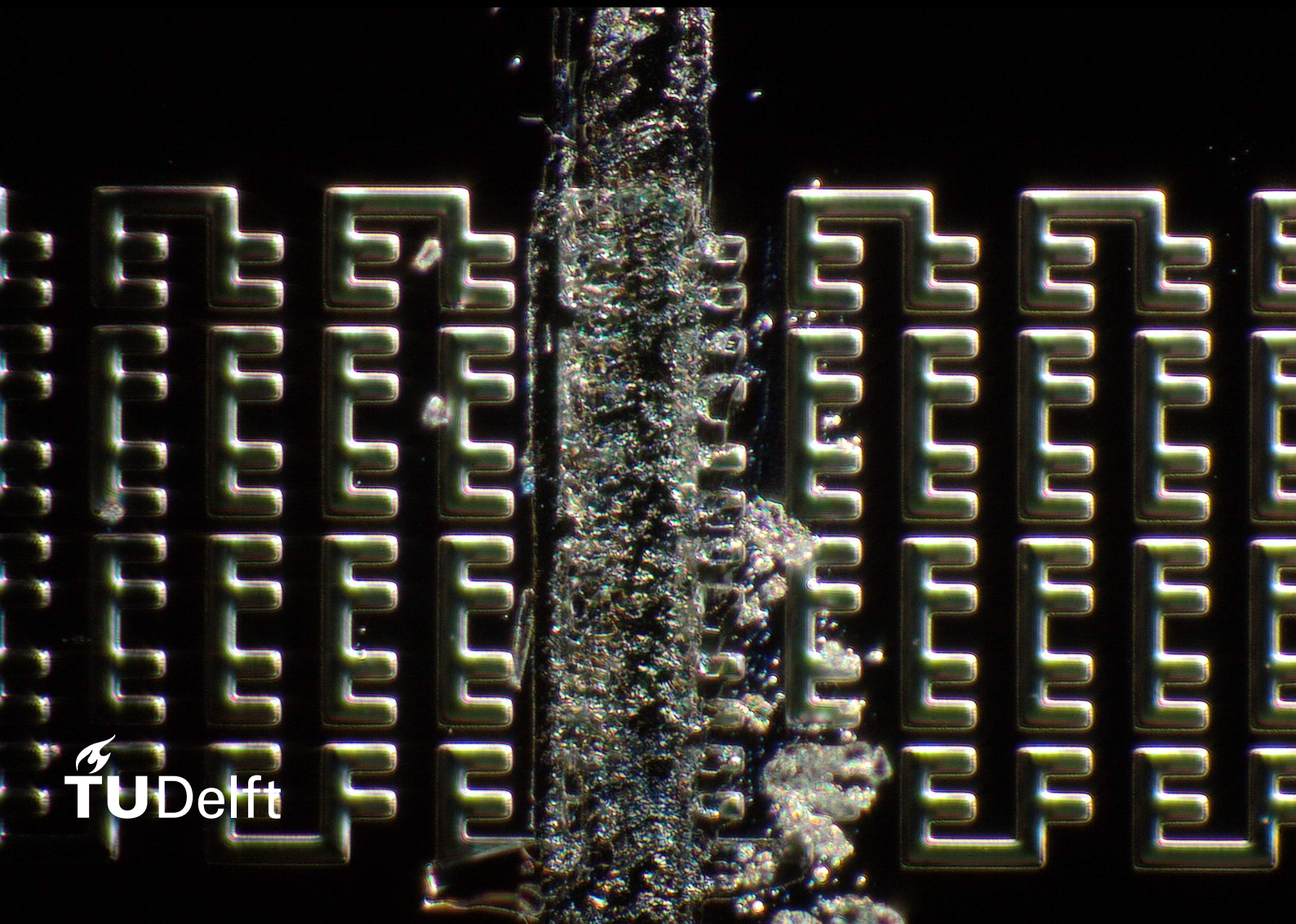

TU Delft

Fabrication and Characterization of a Dimer Josephson Junction Parametric Amplifier

Master of Science Thesis

Loek van Everdingen

to obtain the degree of Master of Science
at the Delft University of Technology,
to be defended publicly on Friday July 7, 2023 at 1:00 PM.

Student number:	4686225	
Project duration:	September 4, 2022 – July 7, 2023	
Thesis committee:	Prof. G. Steele,	TU Delft, supervisor
	Dr. C. A. Potts,	TU Delft, daily supervisor
	Prof. C. K. Andersen,	TU Delft

Cover image: Darkfield image of the bottom electrodes for part of an array of Josephson junctions. The horizontal line at the center of the image is a scratch made with a pair of tweezers, which accidentally destroyed the junctions underneath.

An electronic version of this thesis is available at `http://repository.tudelft.nl/`.

Abstract

Superconducting qubits require a low-noise, high-gain parametric amplifier to overcome the added noise during their readout. Josephson junction arrays are suitable candidates, as they have quantum-limited added noise, large saturation power and a tunable resonance frequency. Dimer Josephson Junction Amplifier Arrays (DJJAAs) have a mode structure, which is engineered in such a way that it exploits the wave mixing processes in JPAs when amplifying incoming signals. The resonant modes in this device form pairs, referred to as dimers. The behaviour of two resonant modes in a DJJAA when a drive tone is applied at an intermediate frequency, is analyzed. A maximum gain $G_{\mathrm{max}} = 43.6$ dB and saturation power $P_{1\mathrm{dB}} = 105.9$ dBm is measured. It is demonstrated that the mode resonance frequency shifts if the mode photon population changes. If the drive power was increased above a threshold, self-oscillations were observed in this device. A fabrication process for DJJAAs using overlap Josephson junctions was carried out iteratively. Several issues in the fabrication process were resolved. In the fabricated DJJAAs it was possible to identify and drive resonant modes for gain $G > 20$ dB. The resonant modes in a fabricated device did not form dimers due to offset in the Josephson inductance from its Josephson junctions compared to the design. Future efforts can improve the quality of fabricated overlap Josephson junctions and on studying nonlinear effects that were observed in the device.

Delft, July 2023

Contents

Acknowledgements

Throughout this project, I experienced what it is like to participate in experimental physics research. I learned about the challenges in cleanroom fabrication, cryogenic measurement and theory. This opportunity was granted to me by the people in the SteeleLab research group, whom I would like to thank here.

Firstly, I would like to thank professor Gary Steele for your supervision during the project. During this project your teachings about many different topics and exciting directions for my project were much valued. More importantly, you also reminded me that sometimes I needed to converge on a topic instead of taking on a new idea. I would also like to thank Clinton, for his daily supervision and for helping me see the connections between theory and the experiments I was doing.

Secondly, I would like to thank the other people in SteeleLab for assisting me through this project. You all helped me to tackle challenges I encountered in cryogenic measurements and cleanroom fabrication. And even more importantly, everybody was always very open to have a chat or a coffee while discussing these challenges. Special thanks goes out to Jean-Paul, Clinton and Sercan for reading the drafts for this thesis and giving me valuable feedback on my writings.

I would like my fellow master students in Steelelab for keeping me motivated during this project. I enjoyed our discussions and support in the student room. Well-deserved coffee with you guys was the perfect way to get new ideas and renewed motivation for my project.

I would like to thank my friends for the welcome distractions and discussions that you provided me with. My parents for the endless support I found with you at home . Last but not least, I would like to thank Milou for your drive to understand the project that I was doing and for all the walks and dinners that kept me motivated.

Loek van Everdingen
Delft, July 2023

1 Introduction

Quantum Computing & Qubits
In 1980 Paul Benioff published a paper which demonstrated that it is theoretically possible to build a computer based on the principles of quantum mechanics [1]. The decade that followed marked the start of the field of quantum computing. It was shown that quantum algorithms have the potential to solve problems that classical computers cannot solve [2, 3]. The reason quantum computers can do this, is found in the manner they process information. The quantum bits (called qubits) in such a computer form superpositions between 0's and 1's, similar to the way that an atom can form a superposition between its ground state and excited states. This property allows to solve a set of problems that was previously unaccesable with classical computers, such as calculation of large prime numbers and simulations of large quantum systems [4–6] . This perspective initiated the development of many different types of qubits [7], such an implementation is shwon in figure 1.1. The processes in these qubits occur at very low energy - typically in the regime $\hbar\omega > k_b T$ [8, 9]. As a consequence, it is necessary to amplify any output signals of these devices during their readout. Two requirements on the amplifier are that it adds little thermal noise and is compatible with the quantum mechanics of the detected signal [9].

Josephson Parametric Amplifiers
Parametric amplifiers provide the solution. These amplifiers modulate the parameters of an oscillator (e.g. a kid on a swing) with a specific frequency to amplify signals[11]. In the parametric amplifiers in this thesis, the oscillator is an LC-resonator. This is a circuit consisting of an inductor and a capacitor that stores energies in currents resonating inside it. The inductor in these LC-resonators is made by Josephson junctions [12], which are a structure composed of two pieces of superconducting metal, separated by a non-superconducting barrier. Two Josephson junctions in parallel function as a tunable, non-linear inductor [13]. The parametric amplifiers that use this geometry are known as Josephson Parametric Amplifiers (JPAs) [14–17].

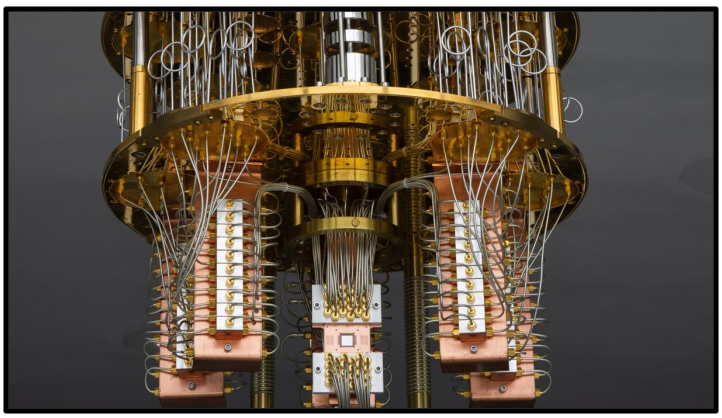

Figure 1.1: An implementation of a quantum computer by IBM. The round golden plate is part of the dilution refrigerator that contains their experimental setup. Figure adapted from [10]

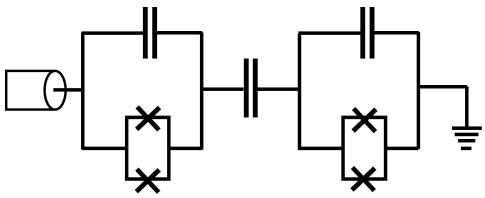

Figure 1.2: Equivalent circuit of the model of a DJJAA. Two *LC*-resonators are coupled through a capacitor. The inductor in each resonator is replaced by two parallel Josephson junctions, which are marked by crosses.

Central to this thesis is a specific type of JPA that is called the dimer Josephson junction array amplifier (DJJAA), which has been developed by Winkel et al.[18]. This design can be modelled as a combination of two *LC*-resonators, which have the same resonance frequencies, connected by a capacitor. This model is shown in figure 1.2. It describes two coupled harmonic oscillators, such as two masses on springs [19]. In both cases the coupling between two resonators results in an opposite shift of their resonance frequencies. The result is that the eigenfrequencies of a DJJAA form pairs, which are called dimers. These dimers are suitable for parametric amplification because they are resonant with the different frequencies that are mixed in this process.

A limitation faced by many JPA designs is the limited signal power that they can process [20]. For a too large input signal power the gain in the output signal disappears, which defeats the purpose of having an amplifier. This issue is known as amplifier saturation. It can be mitigated by using larger Josephson junctions with a corresponding larger critical current I_c. To this purpose, we fabricated DJJAAs using overlap junctions [21]. This Josephson junction avoids deposition of metals under specific angles, as is common in Josephson junction fabrication [22]. The result is that overlap junctions can be made arbitrarily large, making them suitable for JPAs [18].

The motivation of this project is to provide Steelelab with a working JPA that is well-suited for the experiments conducted in the lab. The large flux-tunable range of the DJJAA in combination with its modified mode structure make it a promising candidate. The use of overlap junctions ensures this amplifier has a large saturation power. This thesis project builds on experience with JPA design and fabrication through previous master thesis project in Steelelab [23–26].

Goals of this Thesis
During this thesis project we gratefully accepted the help from the group of Ioan Pop from Karlsruhe Institute of Technology [18], who provided us with a working DJJAA and design files for it. These design files were used during fabrication of DJJAAs in this thesis project.

The first goal of the project is to characterize the DJJAA that was provided by Ioan Pop and assess its performance as an amplifier in the 6-8 GHz range. Most experiments in Steelelab are conducted in this frequency range. We investigated saturation properties of the device and explored different manners of parametric driving.

The second goal is to provide Steelelab with a fabrication recipe for functioning DJJAAs. Part of this is the fabrication of overlap junctions in a cleanroom in Delft. This was a process that required various iterations of the junctions. To assess if the DJJAA that resulted from this process is functioning, basic amplifier characterizations were measured on it.

Thesis Outline
The rest of thesis report is divided in four chapters. The next chapter introduces the theoretical background that is necessary to understand the results of our experiments. The methods that we used in fabrication are then presented in chapter 3. This chapter also discusses our measurements setup and measurement protocols. Chapter 4 gives the result of measurements on our DJJAAs and discusses these measurements. Lastly, in chapter 5 the results are summarized and recommendations for future research are provided.

2

Theoretical background

This chapter presents the theory necessary to understand the results in this thesis. First microwave circuits are explained in section 2.1. The LC-resonator is introduced and it is demonstrated what happens at the resonance frequency of such a device. Then microwave transmission lines and impedance matching are discussed. Section 2.2 introduces the basics of superconductivity, necessary to understand the functioning of the Josephson junction. It is discussed how an arrangement of two parallel Josephson junctions can be used as a tunable-inductor. The concept of parametric driving is presented in section 2.3. It is derived how this can lead to amplification of a signal in an LC-oscillator. Section 2.4 shows how in a JPA, which contains two Josephson junction, this amplification arises due to the Kerr-nonlinearity. Additionally, the concept of amplifier saturation and self-oscillations are discussed. It is demonstrated how Josephson junction arrays can be used to mitigate amplifier saturation in section 2.5 and a model to describe DJJAAs is presented. Lastly, the techniques that are used to fabricate DJJAAs in this thesis are discussed in section 2.6.

2.1. Microwave Circuits

This section introduces concepts from electromagnetic engineering that are useful for understanding the parametric amplifiers and measurement setup that are used throughout this thesis. First the concept of impedance is discussed and then used in a general formalism for understanding the response of electrical systems. In subsection 2.1.2 and 2.1.3 this formalism is applied to two electrical systems, namely the LC-resonator and the transmission line. The derivations underlying the theory in this section are set apart in a clear manner in the book by Pozar [27]. A more in-depth discussion on impedance can be found in [28].

2.1.1. Interpreting the Response of a Circuit

Olivier Heaviside coined the term impedance in the 18th century when referring to the ratio of the complex ratio V/I in the context of AC circuits [29]. The concept turned out to be characteristic to the kind of field and medium to which it was applied. In this we will focus on the electrical impedance, which was defined as V/I, as this definition is useful to the contents of this thesis. We then use it to derive the response of a circuit in terms of reflected waves.

It is generally used in the context of lumped-element circuits which operate with AC currents. For a circuit operating at a frequency ω the three most common circuit elements are the resistor, capacitor and inductor. They respectively have electrical impedances

$$Z_R = R, \qquad Z_c = \frac{1}{i\omega C}, \quad \text{and} \quad Z_L = i\omega L. \tag{2.1}$$

The electrical impedance of these components illustrates how each of them responds to AC currents at different frequencies. In a network circuit, impedances of different elements can be combined according to Kirchoff's laws [27]. Unfortunately, real life circuits are not strictly lumped-element, which makes it hard to directly apply this definition of impedance. For that purpose we introduce a more practical definition of impedance. We consider an electrical circuit at N points, as shown in figure 2.1. On each point n there is an incident electrical wave (V_n^+, I_n^+) and a reflected electrical wave (V_n^-, I_n^-), each with an equivalent voltage and current. These points are generally referred to as ports. The total current at a port i is the sum of the contributions from the individual waves:

$$V_i = V_i^+ + V_i^- \quad \text{and} \quad I_i = I_i^+ + I_i^- . \tag{2.2}$$

This description of a network allows for the definition of an impedance matrix, relating the voltages and currents at the differrent signal ports:

$$\begin{bmatrix} V_1 \\ V_2 \\ \vdots \\ V_N \end{bmatrix} = \begin{bmatrix} Z_{11} & Z_{12} & \cdots & Z_{1N} \\ Z_{21} & \ddots & & \vdots \\ \vdots & & \ddots & \vdots \\ Z_{N1} & \cdots & \cdots & Z_{NN} \end{bmatrix} \begin{bmatrix} I_1 \\ I_2 \\ \vdots \\ I_N \end{bmatrix}. \tag{2.3}$$

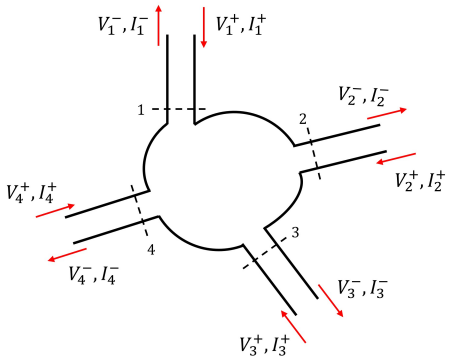

Figure 2.1: An arbitrary N-port device, in this example $N = 4$. At each port the incoming and outgoing current and voltage are labelled. Figure adapted from [27].

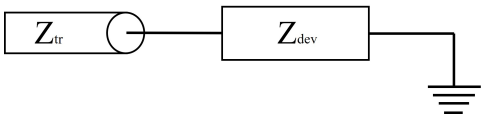

Figure 2.2: A one port device with impedance Z_{dev} coupled to a transmission line with impedance Z_{tr}

The individual matrix elements Z_{ij} can be calculated as:

$$Z_{ij} = \left.\frac{V_i}{I_j}\right|_{I_k=0 \text{ for } k\neq j}. \tag{2.4}$$

This is the definition of input impedance. The numerical value of an element Z_{ij} is found by driving port j with a current I_j and measuring the resulting open-circuit voltage V_i at port i. As it is completely defined by the impedance at the input of our electrical network, this is known as the input impedance. If a circuit consist of purely lumped elements, the input impedance is equal to the electrical impedance.

The matrix representation in equation 2.3 describes an N-port network as a matrix with $N \times N$ independent elements. This number of parameters can be reduced if a network is reciprocal, in which case the impedance matrix becomes symmetric (i.e $Z_{ij} = Z_{ji}$). A reciprocal network has the property that the output at port i due to an input at port j, is the same as an output at port j due to an input at port i.

Measuring voltages and currents involves measuring the amplitude and phase of a travelling wave. At microwave frequencies this causes a problem, as it not possible to unambiguously define an equivalent current and voltage. A solution is provided by instead describing the network in terms of its response to incoming and reflected voltage waves at each port. The matrix relating these two quantities is known as the scattering matrix:

$$\begin{bmatrix} V_1^- \\ V_2^- \\ \vdots \\ V_N^- \end{bmatrix} = \begin{bmatrix} S_{11} & S_{12} & \cdots & S_{1N} \\ S_{21} & \ddots & & \vdots \\ \vdots & & \ddots & \vdots \\ S_{N1} & \cdots & \cdots & S_{NN} \end{bmatrix} \begin{bmatrix} V_1^+ \\ V_2^+ \\ \vdots \\ V_N^+ \end{bmatrix}. \tag{2.5}$$

The scattering parameters S_{ij} can be measured straightforwardly using a vector network analyzer. Each of these elements is defined as the ratio of the incoming voltage wave V_i^+ over the reflected voltage wave V_i^-. This can also be expressed as

$$S_{ij} = \left.\frac{V_i^-}{V_j^+}\right|_{V_j^+=0 \text{ for } k\neq j}. \tag{2.6}$$

Many devices, among which the amplifiers in this thesis, only have a single port from which the input signal is reflected. The signal is transmitted into the device through a transmission line. In this situation, which is illustrated in figure 2.2, the only scattering parameter is S_{11}. The impedances of the different devices have an exact relation to S_{11} in this situation:

$$S_{11} = \frac{Z_{\text{dev}} - Z_{\text{tr}}}{Z_{\text{dev}} + Z_{\text{tr}}}. \tag{2.7}$$

This equation expresses S_{11} in terms of the device and transmission line input impedance, respectively Z_{dev} and Z_{tr}. This reflection coefficient shows that reflections occur at the interface between a device and coupled transmission line if their impedance is different. In general the real part of the input impedance in a one-port network is related to the dissipated power and the imaginary part to the energy stored in the system.

We now have a basic set of tools to analyze networks. As a next step we apply these to two simple networks. The LCR-resonator consists of lumped-elements, whereas the transmission line is a distributed network.

2.1.2. The Response of an LCR-Circuit

When operating a device with oscillating currents, it is important to consider the resonance frequencies of the circuit. At these frequencies the oscillating circuits dissipates power into the environment. In this section we will investigate this property by considering an LCR-resonator circuit.

The simplest resonator circuit, consists of a parallel inductor (L), a resistance (R). A sinusoidal current can be induced in this circuit:

$$I = I_o \cos\left(\omega_0 t + \phi\right), \tag{2.8}$$

where I_0 is the amplitude and ϕ an arbitrary phase offset. ω_0 is the resonance frequency of the circuit. This is the frequency at which the circuit converts energy stored in the electric field of the capacitor C in energy stored in the magnetic field of the inductor L and vice versa. This resonance frequency ω_0 is found to be

$$\omega_0 = \frac{1}{\sqrt{LC}}. \tag{2.9}$$

An LC-resonator is an idealized circuit, as it is lossless. Once oscillations at ω_0 are induced, the circuit will continue resonating forever. To incorporate losses in this circuit, a resistance R is placed in parallel to the inductor and capacitor. This circuit is depicted in figure 2.3 (a).

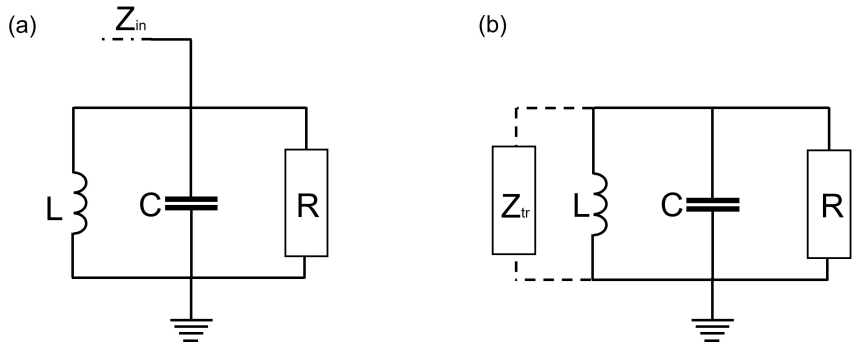

Figure 2.3: Circuit diagram for an LCR-circuit coupled to a transmission line (a). In (b) an equivalent circuit is shown, where the effect of the transmission line is modelled by a parallel resistance.

To understand what happens in this circuit at resonance, we consider its input impedance Z_{in} by application of Kirchoff's law

$$Z_{\text{in}} = \left(\frac{1}{R} + \frac{1}{i\omega L} + i\omega C\right)^{-1}. \tag{2.10}$$

Inspection of equation 2.10 reveals that at the resonance frequency ω_0, the imaginary part of the impedance is equal to zero. The absolute value of the impedance is then minimized and it is purely resistive. Using the definition of impedance, the current amplitude in the circuit can be inferred using the definition of input impedance $I_0 = |I(\omega)| = V/Z_{\text{in}}$. Figure 2.4 reveals that this amplitude has a maximum at the resonance frequency.

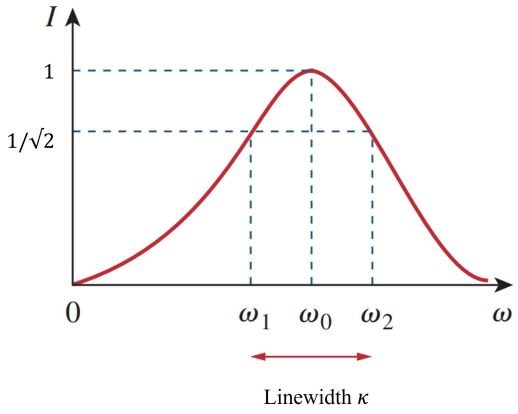

Figure 2.4: Current in an LCR-circuit as a function of frequency ω. At the frequencies ω_1 and ω_2, the current amplitude is $1/\sqrt{2}$ times it maximum. κ is the linewidth between those frequencies. Figure adapted from [30].

The losses from the circuit can be quantified by considering the power dissipated from this circuit. This can be calculated using $P(\omega) = I(\omega)^2 R/2$. It follows that maximum power is dissipated at resonance. As the dissipated power is quadratic in current, half the maximum power is dissipated when $I(\omega) = 1/\sqrt{2} I_{\max}$, for a maximum current $I_{\max}$. The bandwidth along which the current has a value larger than half its maximum is indicated as the linewidth κ.

In a circuit with low losses, the peak in figure 2.4 is narrow and the linewidth κ is smaller. A measure to quantify this is the quality factor Q[30]

$$Q = \frac{\omega_0}{\kappa}. \tag{2.11}$$

The quality factor can be interpreted as the ratio of the peak energy stored in a circuit over the energy dissipated by that circuit at resonance. The linewidth κ is then called the total loss rate.

As a next step the LC-resonator that is considered is coupled to other parts of a larger circuit via a transmission line at its input. The input impedance of this transmission line can be modelled as a parallel impedance, as in done in figure 2.3 (b)[28]. In this case the total loss rate can be split in two parts. The external decay rate κ_{ext} expresses the rate at which photons are carried away into other parts of the circuit (i.e. via the transmission line). The internal decay rate κ_{int} corresponds to losses inside the LC-resonator. The latter is the power dissipated via the resistance [30]. These two decay rates are related to the total loss rate as $\kappa = \kappa_{\text{int}} + \kappa_{\text{ext}}$.

The response of this circuit is determined by its reflection coefficient S_{11}. As this is a complex, frequency-dependent quantity, it is referred to as the system response function. For an LCR-resonator coupled to a transmission line, the system responce function depends on both κ_{int} and κ_{ext}. The ratio between these decay rates is an indicator of the system behaviour. This is reflected in the coupling efficiency $\eta \equiv \kappa_{\text{ext}}/\kappa_{\text{tot}}$. Three regimes can be distinguished for this parameter:

- **Undercoupled**, $\eta < 1$: The losses internal to the resonator are larger than losses to the outside environment
- **Crictially coupled**, $\eta = 1$: Internal and external losses are equal. This allows for maximum power transfer between the resonator and tranmission line.
- **Overcoupled**, $\eta > 1$: the losses to the external environment are larger than those inside the resonator.

The difference between these regimes becomes apparent when considering the phase and amplitude of response function of the system, as is illustrated in figure 2.5.

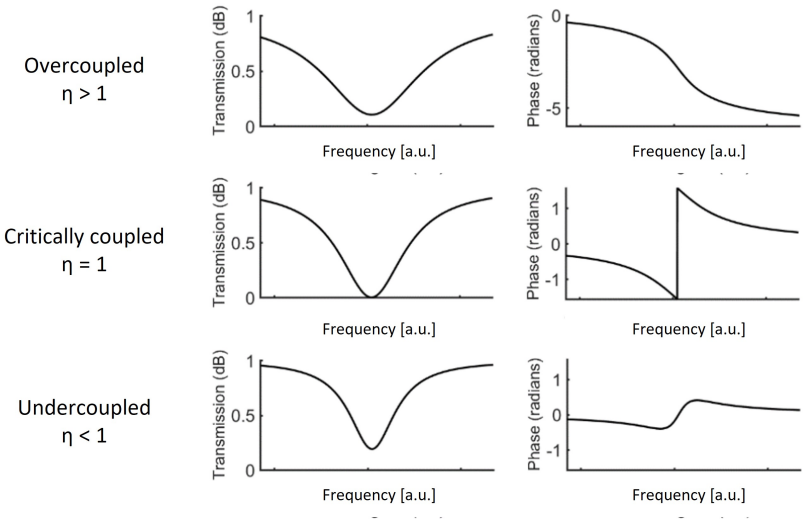

Figure 2.5: Reflection amplitude and phase response of a transmission line coupled to an LC-resonator in different coupling regimes. Figure adapted from [31]

2.1.3. The Microwave Transmission Line

A crucial component for building circuits, is the transmission line. Unlike the components in an LCR-resonator, the size of a transmission line comprises a significant portion of the electrical wavelength. As a result, current and voltage cannot be considered to be constant over the physical dimension of this component. Therefore, the transmission line is considered a distributed element. This subsection discusses how to deal with this class of electrical components and demonstrates their use in minimizing reflections between circuit components.

The finite size of distributed elements has to be taken account of explicitly in our notation. This is generally resolved by using a distinct notation for voltage and current at a specific point and the voltage and current amplitude. The former is a function of position and time and will be denoted as $V(z,t)$ and $I(z,t)$. The latter only is a function of position, such that we can write it as $V_0(z)$ and $I_0(z)$. This notation will be used throughout this entire section.

In 1876, Olivier Heaviside invented the equations to deal with transmission lines, to apply this in design of telegraph cables [32]. He aptly named the resulting equations the telegrapher's equations. They model a transmission line as two parallel wires which carry an opposite current $I(z,t)$. Between these cables there is a voltage difference $V(z,t)$. The model considers a piece Δz of the cable length, which can be considered by an equivalent lumped-element circuit shown in figure 2.6. A section of a transmission line is considered to be a series resistor R and inductance L, which are shunted with conductance G and a capacitor C. The shunted conductance G represents electrical losses along the line.

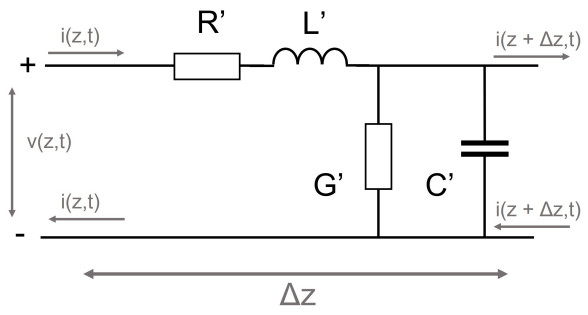

Figure 2.6: Circuit model of a piece of transmission line with length Δz using the telegraphers model.

By application of Kirchoff's laws, we can construct two relations between the voltage and currents along the portion Δz:

$$V(z,t) - R\Delta z I(z,t) - L\Delta z \frac{\partial I(z,t)}{\partial t} - V(z+\Delta z,t) = 0,$$

$$I(z,t) - G\Delta z V(z+\Delta z,t) - C\Delta z \frac{\partial V(z+\Delta z,t)}{\partial t} - I(z+\Delta z,t) = 0.$$

This set of equations can be converted to a set of differential equations if the length of the segment Δz is considered to be infinitesimal:

$$\frac{\partial V(z,t)}{\partial z} = -RI(z,t) - L\frac{\partial I(z,t)}{\partial t}, \tag{2.13a}$$

$$\frac{\partial I(z,t)}{\partial z} = -GV(z,t) - C\frac{\partial V(z,t)}{\partial t}. \tag{2.13b}$$

These are the telegraphers equations in time-domain form. In the applications considered in this thesis, transmission lines are often superconducting. This allows us to consider them to be lossless, which means that $R \approx G^{-1} \approx 0$. In this approximation, only the derivative terms in equations 2.13 remain. This makes it possible to derive two wave equations from them:

$$\frac{1}{LC}\frac{\partial^2 V(z,t)}{\partial z^2} = \frac{\partial^2 V(z,t)}{\partial t^2}, \tag{2.14a}$$

$$\frac{1}{LC}\frac{\partial^2 I(z,t)}{\partial z^2} = \frac{\partial^2 I(z,t)}{\partial t^2}. \tag{2.14b}$$

The general solutions to this set of equations are plane waves. Their amplitude can be separated from their time-dependence as $v(z,t) = V_0(z)e^{i\omega t}$ and $I(z,t) = I_0(z)e^{i\omega t}$. The solutions for the current $I(z)$ and voltage $V(z)$ amplitude are of the general form

$$V_0(z) = V_0^+ e^{-S_{11}z} + V_0^- e^{S_{11}z}, \tag{2.15a}$$

$$I_0(z) = I_0^+ e^{-S_{11}z} + I_0^- e^{S_{11}z}. \tag{2.15b}$$

The superscripts + and − denote the direction of the traveling wave. The subscript 0 denotes the complex amplitude of the respective quantity. $S_{11} = \alpha + i\beta$ is the complex propagation constant of the travelling waves. The real part of this constant α is associated with dissipation of energy along the transmission line and thus is equal to 0 due to the approximation that our transmission lines are lossless. The imaginary part can be derived from equation 2.14 and turns out to be equal to $\beta = \omega\sqrt{LC}$ [27].

It is possible to determine the wavelength of these traveling waves by considering the distance between two maxima of the traveling waves. This becomes apparent from the exponents in the time-domain solution $V(z,t)$:

$$\big(\omega t + \beta z\big) - \big(\omega t + \beta(z+\lambda)\big) = 2\pi \quad \longrightarrow \quad \lambda = \frac{2\pi}{\beta}. \tag{2.16}$$

The measurements considered in this thesis are at microwave frequencies. The wavelength of the currents that are considered is on the order of millimeters. This wavelength is large enough that we cannot consider transmission lines to be strictly lumped elements. They are thus considered as distributed elements. In the next section we will consider the effect of the length of a transmission lines on reflections.

2.1.4. Reflected Waves at an Interface

In section 2.1.1 it was shown that reflections can occur at the interface between a device and transmission line. As the transmission line is a distributed element, this can lead to standing wave patterns inside it. In this section we consider the effect of the length and impedance of a transmission line impedance on these standing wave patterns.

We first need an expression for the input impedance of the transmission line. By plugging the plane wave solution for the voltage $V_0(z)$ from equation 2.15a into equation 2.13a, the ratio of the travelling current over voltage can be determined

$$Z_{\text{tr}} = \frac{V_0^+}{I_0^+} = \frac{-V_0^-}{I_0^-} = \sqrt{\frac{L}{C}} \tag{2.17}$$

This ratio Z_{tr} is commonly referred to as the characteristic impedance of the transmission line. Now we can consider the interface between a transmission line which is terminated in a load Z_{dev}, such as the one-port device in figure 2.2. The reflections at the interface between the device and transmission line are described by the S_{11} parameter from equation 2.7. The numerical value for S_{11} indicates how much power is reflected back into the transmission line at the interface. Only if the characteristic impedance of the transmission line is equal to that of the device, all power is transmitted into the device. In the latter situation the device is said to be impedance matched.

We can use the S_{11} parameter from equation 2.7 to rewrite the voltage and current amplitude from equation 2.15a and 2.15b in terms of an incoming and a reflected wave

$$V_0(z) = V_0^+ \left(e^{-i\beta z} + S_{11} e^{i\beta z}\right), \tag{2.18a}$$

$$I_0(z) = \frac{V_0^+}{Z_0} \left(e^{-i\beta z} - S_{11} e^{i\beta z}\right). \tag{2.18b}$$

Clearly, the reflected wave disappears in case of perfect impedance matching ($S_{11} = 0$). This is an ideal case. In practice there is a reflected wave present. The reflected wave causes standing waves inside the transmission line. The remainder of this section shows how these standing waves can be mitigated by transforming the impedance. To this purpose we first define the positive distance from the input of the load $l = -z$. We can use this to rewrite the magnitude of the voltage waves from equation 2.18a in terms of l

$$|V_0(z)| = |V_0^+| \left|1 + S_{11} e^{2j\beta z}\right| = |V_0^+| \left|1 + S_{11} e^{-2j\beta l}\right|. \tag{2.19}$$

This result simplifies to $|V(z)| = |V_0^+|$ in the absence of reflections ($S_{11} = 0$). The distance between two voltage maxima from this equation is $l = 2\pi/2\beta = \pi\lambda/2\pi = \lambda/2$, where λ is the wavelength on this particular transmission line. And the difference between a minimum and a maximum is $l = \pi/2\beta = \lambda/4$.

This result already demonstrates how the magnitude of the voltage waves is related to the distance away from the load impedance. However, the reflection coefficient in equation 2.19 is only defined at the input of the load impedance ($l = 0$). We can generalize this effect by adding a l-dependent phase shift

$$S_{11}(l) = \frac{V_0^- e^{-i\beta l}}{V_0^+ e^{i\beta l}} = S_{11}(l = 0) e^{-2i\beta l}. \tag{2.20}$$

Equation 2.20 demonstrates how the voltage of the reflected wave oscillates when increasing the travelled distance along the transmission line. We now recombine these results to see how the input impedance, seen when looking to the load from a distance $l = -z$, varies when moving along the transmission line:

$$Z_{\text{in}} = \frac{V_0(-l)}{I_0(-l)} = \frac{V_0^+ \left(e^{i\beta l} + S_{11} e^{-i\beta l}\right)}{V_0^+ \left(e^{i\beta l} - S_{11} e^{-i\beta l}\right)} Z_0 = \frac{1 + S_{11} e^{-2i\beta l}}{1 - S_{11} e^{-2i\beta l}} Z_0. \tag{2.21}$$

With this result, we can design the transmission line at the input of the device in such a way, that the input impedance of the load is minimized for electrical waves entering it. This result can be applied to engineer amplifier circuits such that their operational bandwidth is much increased [15]. During measurements on JPAs, different parts of the measurement setup are connected via transmission lines. Understanding the wave patterns that can arise due to impedance mismatches at the interfaces is useful for the interpretation of the measurement.

2.2. Superconductor Physics

When some metals, such as aluminium or mercury, are cooled below their critical temperature they loose their electrical resistance. This effect was first observed by Heike Kamerlingh Onnes in 1911 and dubbed superconductivity shortly after [33]. A microscopic explanation of this effect was given in 1956 by Bardeen, Cooper and Schieffer (BCS) [34]. BCS-theory starts of from a weak attractive interaction between electrons due to vibrations of the atomic lattice. If the temperature decreases below a critical temperature T_c, this interaction becomes stronger than Coulomb repulsion. As a result electrons form pairs with net charge $2e$ and no spin, known as Cooper pairs. As Cooper pairs have no spin, they behave as bosons.

The amplifiers that are considered in this thesis, derive gain from a structure called the Josephson junction. To understand this structure, the wave function of Cooper pairs in a superconductor is introduced first. This wave function was derived in the phenomenological theory of superconductivity that Ginzburg and Landau derived in 1959 [35]. Then the relations governing the voltage-current relation of the Josephson junction are derived. This is followed by the introduction of the superconducting quantum interference device. Finally subsection 2.2.5 explains how this device is used in JPAs. The discussion on superconductivity in this chapter serves to understand the superconducting structures in JPAs. A more complete overview of the topic is given by Richard Feynman [13] and Thinkham [36].

2.2.1. The Wave Function in Superconductors

As a first step, we want to understand how Cooper pairs are distributed inside a superconductor. As they are bosons, Cooper pairs form a bosonic condensate and display a collective wave function $\psi(\vec{r})$. From the theory of Ginzburg and Landau it follows that the Cooper pair density $n_c(t)$ is correlated with the magnitude of this wave function: $|\psi(\vec{r})|^2 \propto n_c(t)$. This assumes that Cooper pairs are uniformly distributed throughout the superconductor. The wave function describing this collective state is known as the order parameter and can now be described as[35]:

$$\psi(\vec{r}) = \sqrt{n_c} e^{i\theta(\vec{r},t)}, \tag{2.22}$$

with $\theta(\vec{r},t)$ the phase of the condensate. From equation 2.22 it is clear that if this phase increases by a multiple of 2π the value of the wave function is identical. From this observation it follows that if a superconductor has a hole in it (e.g. a circular piece of superconductor), the phase of the condensate can change by $2\pi n$ for any integer value of n [37].

2.2.2. The Josephson Effect

We now turn to a specific situation, which was first studied by Brian Josephson in 1962 [12]. The situation consists of two superconductors, which are separated by a thin insulating barrier. This structure is known as a Josephson junction. Individual electrons cannot pass this barrier classically, but we will prove that Cooper pairs can quantum mechanically. This leads to a rather surprising current relationship, which we will analyze by looking at the wave functions inside both superconductors.

A Josephson junction is illustrated schematically in figure 2.7. The amplitude of encountering a Cooper pair in each superconducting metal is described by a wave function of the form in equation 2.22. These wave functions are $\psi_A = \sqrt{n_A} e^{i\theta_A}$ and $\psi_B = \sqrt{n_B} e^{i\theta_B}$. The subscripts A and B indicate the wavefunction in superconductors on opposite sides of the insulating barrier. The lower part of figure 2.7 shows the amplitude of both wave functions as a function of position. If we apply a voltage $V(t)$ across the junction, the resulting potential across the barrier equals $2eV$, due to the charge of the Cooper pairs. The rate at which Cooper pairs tunnel through the barrier is captured in the coupling constant K. We define the zero of energy halfway across the barrier. We now have sufficient information to draw up the Schrödinger equation for both wave functions of this system

$$i\hbar \frac{\partial \psi_A}{\partial t} = eV\psi_A + K\psi_B, \tag{2.23a}$$

$$i\hbar \frac{\partial \psi_B}{\partial t} = -eV\psi_B + K\psi_A. \tag{2.23b}$$

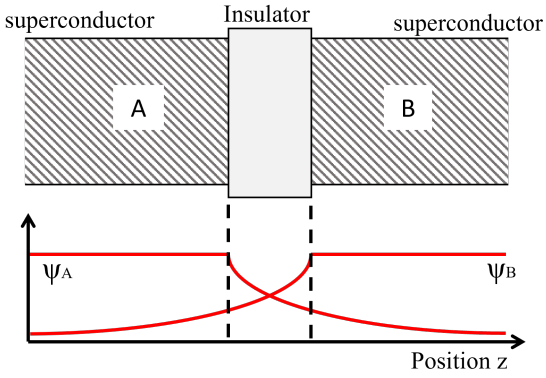

Figure 2.7: The upper part of the figure shows a schematic illustration of a Josephson junction. The graph in the lower part of the images illustrates the behaviour of the wave functions ψ_A and ψ_B as a function of position z. Two dotted lines mark the position of the insulating barrier.

In both equations the potential difference is equal to eV, because we defined the zero of energy to be halfway at the barrier. We can rewrite these equations more conveniently in matrix form

$$i\hbar\frac{d}{dt}\begin{bmatrix}\sqrt{n_a}e^{i\theta_a}\\ \sqrt{n_b}e^{i\theta_b}\end{bmatrix}=\begin{bmatrix}eV & K\\ K & -eV\end{bmatrix}\begin{bmatrix}\sqrt{n_A}e^{i\theta_A}\\ \sqrt{n_B}e^{i\theta_B}\end{bmatrix} \tag{2.24}$$

This is a set of two coupled differential equations. To find a solution, we first write out the time-derivative of both wave functions

$$\frac{\partial\psi_A}{\partial t}=\left(\dot{\sqrt{n_A}}+i\sqrt{n_A}\dot{\theta_A}\right)e^{i\theta_A}, \tag{2.25a}$$

$$\frac{\partial\psi_B}{\partial t}=\left(\dot{\sqrt{n_B}}+i\sqrt{n_B}\dot{\theta_B}\right)e^{i\theta_B}, \tag{2.25b}$$

In the righthand-side of both equations, the time derivative of a quantity is indicated with a dot above it. We can plug those time-derivatives in equation 2.23a and 2.23b and multiply with respectively $e^{-\theta_A}$ and $e^{-\theta_B}$

$$\left(\dot{\sqrt{n_A}}+i\sqrt{n_A}\dot{\theta_A}\right)=\frac{1}{i\hbar}\left(eV\sqrt{n_A}e^{i\theta_A}+K\sqrt{n_B}e^{i\delta}\right), \tag{2.26a}$$

$$\left(\dot{\sqrt{n_B}}+i\sqrt{n_B}\dot{\theta_B}\right)=\frac{1}{i\hbar}\left(-eV\sqrt{n_B}+K\sqrt{n_A}e^{-i\delta}\right). \tag{2.26b}$$

The Josephson phase $\delta=\theta_B-\theta_A$ is the phase difference across the junction. The most straightforward approach to solving these equations is by taking their real and imaginary part. We start with the imaginary part of both equations:

$$\dot{n_A}=+\frac{2}{\hbar}K\sqrt{n_A}\sqrt{n_B}\sin(\delta), \tag{2.27a}$$

$$\dot{n_B}=-\frac{2}{\hbar}K\sqrt{n_A}\sqrt{n_B}\sin(\delta). \tag{2.27b}$$

This gives us equations for the charge density in both superconductors. If we now combine these time-derivatives, we can find an expression for the electric current amplitude I across the junction. This is the DC Josephson relation

$$I=\frac{\partial(n_B-n_A)}{\partial t}=\frac{K}{\hbar}\sqrt{n_A}\sqrt{n_B}\sin(\delta)=I_c\sin(\delta) \tag{2.28}$$

The second equality is used to define the junction critical current I_c. We now turn to the real part of equation 2.26a and 2.26b:

$$\dot{\theta_A}=-\frac{K}{\hbar}\frac{n_B}{n_A}\cos(\delta)-\frac{eV}{\hbar} \tag{2.29a}$$

$$\dot{\theta_B} = -\frac{K}{\hbar}\frac{n_A}{n_B}\cos(\delta) + \frac{eV}{\hbar} \tag{2.29b}$$

We can use this to find the time-derivative of the Josephson phase, which turns out to be

$$\dot{\delta} = \frac{\partial(\theta_B - \theta_A)}{\partial t} = \frac{2eV}{\hbar}. \tag{2.30}$$

This is known as the AC Josephson relation. From the AC and DC Josephson relations a current-voltage characteristic can be inferred, which is illustrated in figure 2.8. The Josephson relations state, that if no voltage is applied the current amplitude can take any value between $-I_c$ and I_c. Equation 2.30 states that an applied DC voltage causes a linear slope in the phase. Since the prefactor $\frac{2e}{\hbar} \gg 1$, a small voltage causes rapid oscillations in the current amplitude. As $\langle \sin(t) \rangle = 0$, the resulting net current equals zero. If the voltage becomes larger than the energy required to break up Cooper pairs, a current will start flowing once again. This causes the linear slope far away from zero in figure 2.8. This linear slope depicts Ohm's law.

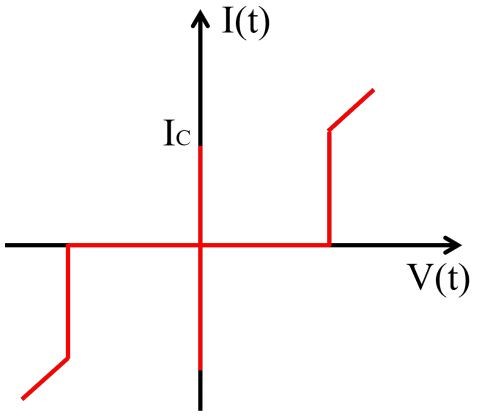

Figure 2.8: The IV-characteristic of a Josephson junction

2.2.3. Flux Quantization

In section 2.2.1 it was observed that the phase θ of the superconductor wave function must vary with an integer value when moving around a loop. We can use this property to derive that the flux through a superconducting loop must be quantized.

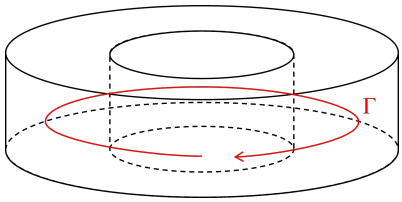

Figure 2.9: A superconducting piece of metal with the contour Γ in red.

To this purpose we consider a loop consisting of superconducting metal, as is illustrated in figure 2.9. A contour Γ can be followed around this loop. The superconducting phase can be influenced by two things: by the momentum of the Cooper pairs along the loop, with velocity $\vec{v}_c$ and mass m_c, and by any applied magnetic field, with a vector potential $\vec{A}$. The spatial gradient of the phase can be expressed as [37]

$$\nabla\theta = \frac{1}{\hbar}\left(m_c\vec{v}_c + 2e\vec{A}\right), \tag{2.31}$$

where $2e$ is the charge of a Cooper pair. The movement of charged particles can be expressed using a current density. As this current is the result of the superconductivity of the loop, it is called a supercurrent density. We will indicate supercurrent density with symbol $\vec{J} = 2en_c\vec{v}_c$. If we now integrate $\nabla\theta$ around the loop, using the supercurrent density $\vec{J}$, we find

$$\oint_\Gamma \nabla\theta d\vec{l} = \frac{m_c}{2en_c\hbar}\oint_\Gamma \vec{J}d\vec{l} + \frac{2e}{\hbar}\oint_\Gamma \vec{A}d\vec{l} = 2\pi n, \tag{2.32}$$

for an integer number n. The second equality stems from the requirement that the phase θ varies with a multiple of 2π when moving around a ring. The integral over the vector potential $\vec{A}$ is equal to the external magnetic flux Φ penetrating the loop. Equation 2.32 can be divided by e and rewritten as

$$\Phi + \mu_0\lambda^2\oint_\Gamma \vec{J}d\vec{l} = 2n\Phi_0, \tag{2.33}$$

where $\lambda^2 = \frac{m_c}{4e^2\mu_0 n_c}$ is the London penetration depth with μ_0 the magnetic permeability [38].This is a measure of the ability of the vector potential to penetrate the bulk of a superconductor [13]. The constant $\Phi_0 = \hbar/2e$ is called the magnetic flux quantum. We will now interpret 2.33 to understand the response of a superconducting loop to magnetic fields. If a magnetic field induces a flux through the loop while it is superconducting, a screening current will arise to counter the magnetic flux penetrating the ring. This follows from Faraday's law. The total flux through the loop is then zero. Now we invert the situation and assume a magnetic field already induces a flux through the loop when it is cooled below its critical temperature. If the magnetic is now removed while the loop is superconducting, a supercurrent starts flowing to ensure that the amount of flux through the loop remains the same. From equation 2.33 it follows that the flux trapped in this loop must be equal to an integer multiple of Φ_0 [13]. This phenomenon is known as flux quantization.

2.2.4. The DC SQUID

The superconducting quantum interference device (SQUID) is a crucial component for creating gain in JPAs. There are two flavors of SQUIDs: the DC SQUID and the RF SQUID. We will limit our discussion to the DC SQUID, as these are utilized in the JPA devices discussed in this thesis.

A DC SQUID is composed of two parallel-connected Josephson junctions, which form a loop in between them. The device is illustrated in figure 2.10. In a DC SQUID there is - as its name suggests - interference between the currents that pass through both Josephson junctions.

To better understand the applicability of the DC SQUID, we will now understand the relation between the current amplitude and the flux through the SQUID loop. For this relation, we first return to equation 2.31 and rewrite it in terms of the elementary flux quantum Φ_0. This relates the vector potential $\vec{A}$ to the gradient of the phase:

$$\hbar\left(\nabla\theta - 2\pi\vec{A}/\Phi_0\right) = 0.$$

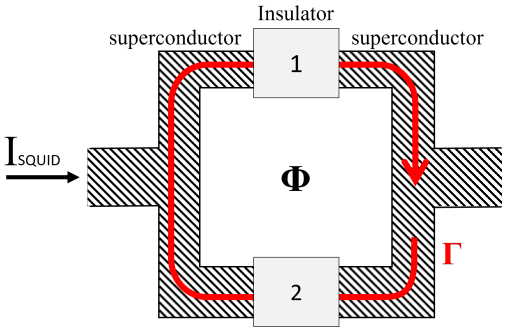

Figure 2.10: A schematic figure of a DC SQUID. The respective Josephson Junctions are labelled 1 and 2. Modified from ref. [13]

Far inside the body of the superconductor the supercurrent density $\vec{J}$ goes to zero [13]. The phase drop across the junctions thus has to be considered separately and will be denoted as $\Delta\theta_{1,2}$ for both junctions. By combining the junction's phase drop with equation 2.33 we can determine the phase drop around a contour Γ, shown in figure 2.10,

$$\Delta\theta_1 + \int_{upper} \vec{A}\cdot d\vec{s} - \Delta\theta_2 + \int_{lower} \vec{A}\cdot d\vec{s}, \tag{2.34}$$

where the subscripts $upper$ and $lower$ respectively denote the respective parts of the loop. One can combine these integrals to find a single integral of the vector potential $\vec{A}$ around the closed contour Γ. This integral equals the magnetic flux Φ enclosed by the SQUID loop. It follows that

$$2\pi\frac{\Phi}{\Phi_0} = \Delta\theta_2 - \Delta\theta_1. \tag{2.35}$$

For simplicity of notation we introduce an average phase drop $\delta_{\text{avg}} = (\Delta\theta_2 + \Delta\theta_1)/2$. The resulting expressions for both phase drops are

$$\Delta\theta_1 = \delta_{\text{avg}} + \pi\frac{\Phi}{\Phi_0},$$

$$\Delta\theta_2 = \delta_{\text{avg}} - \pi\frac{\Phi}{\Phi_0}.$$

The total current can now be written as the sum of the current through the two individual junctions. This is equal to

$$I_{SQ} = I_c\left[\sin\left(\delta_{\text{avg}} + \pi\frac{\Phi}{\Phi_0}\right) + \sin\left(\delta_{\text{avg}} - \pi\frac{\Phi}{\Phi_0}\right)\right] = 2I_c\sin\left(\delta_{\text{avg}}\right)\cos\left(\pi\frac{\Phi}{\Phi_0}\right), \tag{2.37}$$

where the second equality follows from the product sum relation

$$\sin(a+b) + \sin(a-b) = 2\sin(a)\cos(b), \tag{2.38}$$

for two scalars a and b. The average phase drop cannot be determined, but as it is contained in a sine, it can never exceed the critical current. For that reason, equation 2.37 is typically expressed as

$$I_{SQ} = 2I_c\left|\cos\left(\pi\frac{\Phi}{\Phi_0}\right)\right|. \tag{2.39}$$

A different formulation of this equation writes it in terms of the energy stored in the Josephson junction. This requires the definition of the Josephson Energy E_J:

$$E_J = \frac{I_c\Phi_0}{2\pi} \tag{2.40}$$

This formulation can be used to describe the energy stored in a SQUID in a Hamiltonian

2.2.5. Josephson Inductance

In an LC-resonator, a SQUID can be used as an inductor. In this section we derive the inductance from a SQUID and show that this inductance can be tuned by changing the magnetic flux through the SQUID loop. We use equation 2.39 for the critical current of a SQUID. We start by inspecting the definition of inductance

$$\frac{dI(t)}{dt} = \frac{1}{L}V(t). \tag{2.41}$$

We can take the time-derivative of the current across a SQUID from equation 2.39 and plug it in this equation. The derivative of $\sin\left(\delta_{\text{avg}}\right)$ can be accounted for using the AC Josephson relation 2.29a

$$\frac{dI_{SQ}}{dt} = 2I_c\left|\cos\left(\pi\frac{\Phi}{\Phi_0}\right)\right|\cos\left(\delta_{\text{avg}}\right)\frac{2ev(t)}{\hbar}. \tag{2.42}$$

This result matches the definition of an inductance. From the small angle approximation it follows that $\cos\left(\delta_{\text{avg}}\right) \approx 1$. Operating SQUIDs as flux-tunable inductors thus requires that the phase difference δ_{avg} across the junctions is small. The expression for the SQUID inductance now becomes

$$L_{SQ} = \frac{1}{4eI_c\hbar}\frac{1}{\left|\cos\left(\pi\frac{\Phi}{\Phi_0}\right)\right|}. \tag{2.43}$$

This expression can be simplified by introducing the Josephson bare inductance $L_j = \frac{1}{4eI_c\hbar}$. In a typical LC-resonator, a DC SQUID is connected in parallel to a capacitor C. The corresponding resonance frequency is

$$\omega_0(\Phi) = \frac{1}{\sqrt{CL_{SQ}(\Phi)}}. \tag{2.44}$$

As a result, the resonance frequency ω_0 becomes a function of the magnetic flux Φ. Section 2.3 shows that this result can be to tune the resonance frequency of a parametric amplifier.

2.3. General Principles of Parametric Driving

In section 2.1 the LC-resonator was presented and discussed what resonance is. In this section we will discuss how parametric driving can induce amplification of a signal in such a resonant circuit. We will first illustrate how parametric driving works with an example. This is followed by a discussion on the different properties of parametric driving. A clear example that uses a LC-resonator circuit for parametric driving is given by Reed [39].

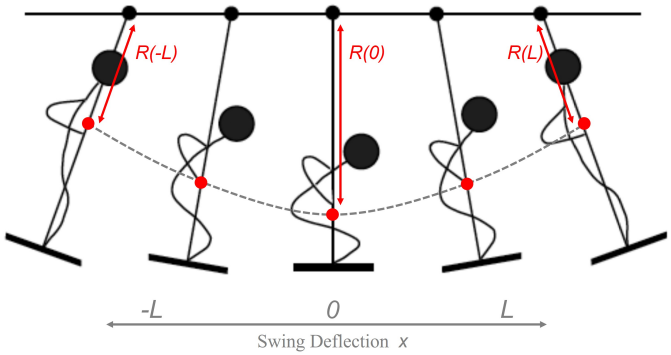

Figure 2.11: A child on a swing can increase the swing's deflection by squatting and standing up. By doing this it modulates the distance $R(x)$ between the hinge and the center of mass. This increases the swings beyond the initial distance L. Figure adapted from [40].

Parametric amplification can be understood by imaginings a child on a swing. The swing has length R. between the hinge and the center of mass of the combination of child and swing. The child can change this length by alternatingg its stance. The surrounding air does not cause any resistance. Initially the child is seated on the swing and just swings back and forth. We will call the position of the swing x. The motion of the swing initially is between $-L$ and L. As their is no air resistance, the child will continue swinging the same distance forever. This situation is illustrated in figure 2.12 (a).

At some point the child wants to swing higher. The child can increase the motion of the swing by alternating its stance. Each time the swing is at its maximum deflection $x = \pm L$ the child stands up and when the swing passes through the center at $x = 0$ the child squats again. By repeating this motion throughout each swing the child will increase the deflections of the swing. This situation is illustrated in figure 2.12 (b) By moving its weight, the child essentially modulates the length of the swing $R(x)$. This modulation is usually referred to as the 'drive' of the amplification. By driving the length of the swing, the child performs mechanical work that is converted in motion of the swing. This is the essence of parametric amplification: periodic variation of a single system variable that is used to amplify oscillations in another variable.

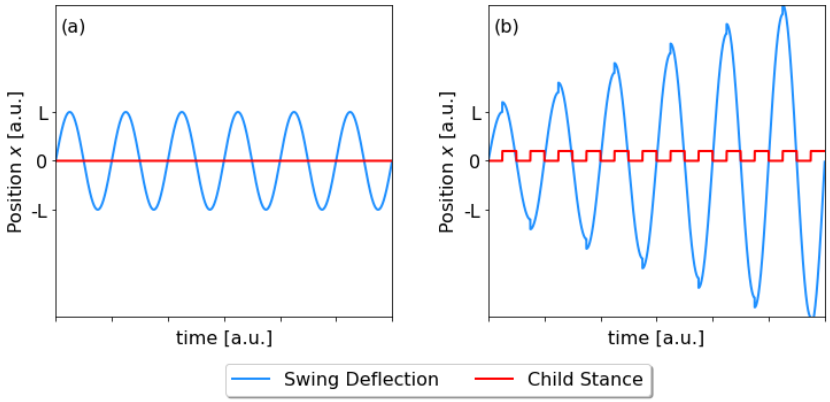

Figure 2.12: Schematic depiction of the swing position over time. In panel (a) the child is squated all the time and the amplitude of the swing movement stays equal to L. In panel (b) the child alternates its stance between squatting and standing up. The red line indicates the child's stance. This modulation of the length of the swing causes the amplitude of the deflections of the swing to increase over time.

In figure 2.12 (b) the child alternates two times between squatting and standing up during every period of the swing motion. That is to say, the frequency ω_d at which it modulates the length $R(x)$ is twice that of the swing motion. The frequency of the signal is normally called the signal frequency. Imagine now that the driving is delayed with half of its phase: the child would have been squatted when the swing has maximum deflection $x = \pm L$ and been standing up when it passes through the center $x = 0$. This would have decreased the amplitude of the swing deflections. The signal amplification is thus dependent on the phase of the driving. This relation between the drive and signal frequency, in which $\omega_d \approx 2\omega_s$, is called degenerate.

The example above showed us how periodic modulation of a system variable can lead to amplification of a signal. In the JPAs in this thesis parametric amplification is induced in circuits equivalent to LC-resonators. This is worked out mathematically in the next subsection. Then the relation between signal and drive frequency is discussed in more depth in subsection 2.3.2. Subsection 2.3.3 discusses the mixing of input at different frequencies that occurs in parametric amplification. Lastly, subsection 2.3.4 then elaborates on noise in parametric amplification.

2.3.1. Parametric Driving of an LC-Resonator

The example in the previous section demonstrated how parametric driving can increase the amplitude of oscillations in a system. We will now derive this mathematically in a driven LC-resonator. It has a capacitor C, an inductor L. A current source induces a sinusoidal current in this circuit with frequency ω. This current serves as the signal that is amplified in parametric amplification. The current in this system can be described with a differential equation

$$\frac{\partial^2 I(t)}{\partial t^2} + \omega_0^2 I(t) = 0. \tag{2.45}$$

In section 2.1.2 we found that the resonance frequency $\omega_0^2 = 1/LC$. We will now start parametrically driving the circuit. The resonance frequency of this circuit is modulated at twice the current frequency ω. The manner in which this occurs does not matter - both the capacitance or the inductance can be alternated. The applied drive oscillates with twice the signal frequency, that is to say $\omega_d = 2\omega$. The result is that the resonance frequency of the circuit becomes time-dependent

$$\omega_0^2(t) = \omega_0^2\left(1 + \alpha \sin\left(\omega_d t + \phi\right)\right), \tag{2.46}$$

where the constant α determines the amplitude of the modulations. α is assumed to be much smaller than 1. The driving happens with a phase offset ϕ with respect to the phase of the current $I(t)$. Plugging equation 2.46 into equation 2.45 gives

$$\frac{\partial^2 I(t)}{\partial t^2} + \omega_0^2\left(1 + \alpha \sin\left(\omega_d t + \phi\right)\right) I(t) = 0. \tag{2.47}$$

The solution of this differential equation is expected to be an oscillating current. We will propose an Ansatz. In this Ansatz we will separate the quickly-varying time-dependencies (via ωt in the sine and cosine) and slowly-varying time-dependencies (via $A(t)$ and $B(t)$). Our Ansatz reads

$$I(t) = A(t)\cos(\omega t) + B(t)\sin(\omega t). \tag{2.48}$$

The quantities $A(t)$ and $B(t)$ in this equation are referred to as the signal quadratures. We stated that this current oscillates with frequency ω. This frequency is assumed to be near, but not necessarily equal to, the resonance frequency of the circuit ω_0. As a next step, the individual terms in equation 2.47 are expanded in terms of this Ansatz. First the double-derivative is done

$$\frac{\partial^2 I(t)}{\partial t^2} = \left(\ddot{A}(t) + 2\omega\dot{B}(t) - \omega^2 A(t)\right)\cos(\omega t) + \left(\ddot{B}(t) - 2\omega\dot{A}(t) - \omega^2 B(t)\right)\sin(\omega t). \tag{2.49}$$

The double-derivatives of $\ddot{A}(t)$ and $\ddot{B}(t)$ are discarded, as $A(t)$ and $B(t)$ vary slowly with time. Next we expand the term $\sin\left(2\omega t + \phi\right) I(t)$ using the Ansatz from equation 2.48

$$\alpha\omega_0^2 \sin\left(\omega_d t+\phi\right)\left(A(t)\cos\left(\omega t\right)+B(t)\sin\left(\omega t\right)\right)= \\ \frac{\alpha\omega_0^2}{2}A(t)\left(\sin\left(\omega t+\phi\right)+\sin\left(3\omega t+\phi\right)\right)+\frac{\alpha\omega_0^2}{2}B(t)\left(\cos\left(\omega t+\phi\right)-\cos\left(3\omega t+\phi\right)\right). \quad (2.50)$$

Product-to-sum relations were used to expand the terms on the right-hand side of this equation. After the equality sign, we used that $\omega_d = 2\omega$ to simplify the resulting expression. This makes it apparent that the current frequency ω is mixed with the parametric driving frequency $\omega_d = 2\omega$. The result contains terms at ω and 3ω. The terms at 3ω are far away from the resonance ω_0 of the LC-resonator and thus strongly attenuated. They are discarded in the rest of this derivation. The terms oscillating with frequency ω effectively acts as a driving force. As ω is near to ω_0 this driving force is expected to increase the amplitude of the current oscillations. In equation 2.50 we can split the terms oscillating with ωt from the phase offset ϕ by using product-to-sum relations again

$$\frac{\alpha\omega_0^2}{2}A(t)\sin\left(\omega t+\phi\right)+\frac{\alpha\omega_0^2}{2}B(t)\cos\left(\omega t+\phi\right)= \\ \frac{\alpha\omega_0^2}{2}A(t)\left(\sin\left(\omega t\right)\cos\left(\phi\right)+\sin\left(\omega t\right)\sin\left(\phi\right)\right)+\frac{\alpha\omega_0^2}{2}B(t)\left(\cos\left(\omega t\right)-\sin\left(\omega t\right)\sin\left(\phi\right)\right)= \\ \frac{\alpha\omega_0^2}{2}\left(A(t)\cos\left(\phi\right)-B(t)\sin\left(\phi\right)\right)\sin\left(\omega t\right)+\frac{\alpha\omega_0^2}{2}\left(A(t)\sin\left(\phi\right)+B(t)\cos\left(\phi\right)\right)\cos\left(\omega t\right). \quad (2.51)$$

After the second equality sign the terms are grouped depending on their dependence on $\cos(\omega t)$ or $\sin(\omega t)$. As a next steps we will combine the expanded terms from equation 2.49 and 2.51 in the differential equation 2.47

$$\left(2\omega\dot{B}(t)+\left(\omega_0^2-\omega^2\right)A(t)+\frac{\alpha\omega_0^2}{2}\left(A(t)\sin\left(\phi\right)+B(t)\cos\left(\phi\right)\right)\right)\cos\left(\omega t\right)+ \\ \left(-2\dot{A}(t)+\left(\omega_0^2-\omega^2\right)B(t)+\frac{\alpha\omega_0^2}{2}\left(A(t)\cos\left(\phi\right)-B(t)\sin\left(\phi\right)\right)\right)\sin\left(\omega t\right)=0. \quad (2.52)$$

Terms in this equation are grouped based on their dependence on $\cos(\omega t)$ or $\sin(\omega t)$. As $\cos(\omega t)$ and $\sin(\omega t)$ never are 0 at same time, a solution for equation 2.52 requires that the quantities within large brackets are zero for all t. In this derivation the losses that are present in an LC-resonator have not been modelled. We will include those by adding a term that depends on the loss rate κ in the next step. This leads to two differential equations for A and B

$$\dot{A}(t)=+2\frac{\omega_0^2-\omega^2}{\omega}B(t)+\alpha\frac{\omega_0}{\omega}\left(A(t)\cos\left(\phi\right)-B(t)\sin\left(\phi\right)\right)-\kappa A(t), \quad (2.53a)$$

$$\dot{B}(t)=-2\frac{\omega_0^2-\omega^2}{\omega}A(t)-\alpha\frac{\omega_0}{\omega}\left(A(t)\sin\left(\phi\right)+B(t)\cos\left(\phi\right)\right)-\kappa A(t). \quad (2.53b)$$

This is a set of two coupled differential equations that describe the evolution of the signal quadratures $A(t)$ and $B(t)$ over time. To find a general solution requires to decouple those equations. This general solution is derived in [23]. The dynamics of the evolution of the signal quadratures depend on the relation between the signal and drive. This relation can be described using the phase offset ϕ and the detuning between the signal and half the drive frequency $\Delta\omega = \omega_0 - \omega_d/2$. We will consider the situation that the driving is degenerate, i.e. $\Delta\omega = 0$. We solve equations 2.53a and 2.53b if the phase offset $\phi = 0$

$$A(t)=A_0 e^{(\alpha-\kappa)t}, \quad (2.54a)$$

$$B(t)=B_0 e^{(-\alpha-\kappa)t}. \quad (2.54b)$$

We can plug the solution for both quadratures in the Ansatz from equation 2.48. The magnitude from the current grows over time, if the drive amplitude α is large than the total loss rate κ. This means the signal is

amplified. The increase in the squared magnitude at a frequency due to the parametric driving is referred to as the gain G at that frequency.

In equations 2.54a and 2.54b, quadrature $A(t)$ increases over time, whereas quadrature $B(t)$ decreases. If we solve equations 2.53a and 2.53b for a phase offset $\phi = \pi$, we find that the inverse happens. In that case quadrature $A(t)$ decreases over time, whereas quadrature $B(t)$ increases. The difference illustrates that degenerate amplification is sensitive to the phase difference between the drive and signal frequency.

In the derivation above, we considered that the detuning $\Delta\omega$ between the signal frequency and half of the drive frequency was equal to zero. In practice this is not always the case. The situation where $\Delta\omega \neq 0$ is discussed in the next subsection.

2.3.2. Nondegenerate Amplification

If parametric driving is degenerate the signal frequency ω_s is equal to half the drive frequency ω_d. If this is not the case, the parametric is called nondegenerate. We will first consider nondegenerate driving in an LC-resonator such as discussed in section 2.3.1, where only a single resonance frequency ω_0 is used to amplify a signal.

In nondegenerate driving, the phase offset ϕ between the drive frequency and the signal frequency is not a constant any more. This is the result of the detuning $\Delta\omega$ between the signal and half the pump frequency. The rate at which the phase offset varies is dependent on the detuning $\Delta\omega$. If the detuning is large enough, both quadratures cannot reach the steady-state gain they reached under degenerate driving. In this case, the gain in both quadratures is effectively equal to the mean value of the quadrature amplitude integrated over the phase. The observed gain now appears to be independent of the phase of the parametric drive. For this reason nondegenerate gain is also referred to as phase-preserving.

If the detuning between signal frequency and half the drive frequency is $\Delta\omega$, then the idler frequency ω_i is the frequency with opposite detuning $-\Delta\omega$ with respect to half the drive frequency. This is illustrated in figure 2.13 (a). In this case it follows that $\omega_s + \omega_i = \omega_d$. It can be proven that if the gain at the signal frequency is $\sqrt{G}$, then the gain at the idler frequency is $\sqrt{G-1}$ [41].

In the previous paragraph we considered nondegenerate driving in a device with a single resonance frequency. However, it is also possible to have a device which has more than one resonant mode. In that case it is possible that the relation between signal, idler and drive frequency is $\omega_s + \omega_i = 2\omega_d$. This is illustrated in figure 2.13 (b). This requires that the dispersion relation of the device is modified in such a way that both the signal and idler frequency correspond with different resonance frequencies of the device [18].

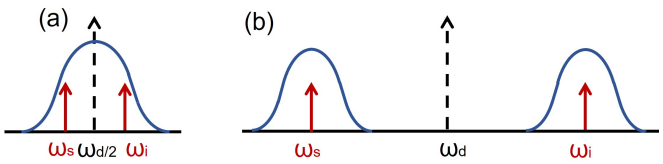

Figure 2.13: Relation between the half drive frequency (black dashed arrow), signal frequency (red arrow) and idler frequency (red arrow) during nondegenerate driving. The signal and idler are detuned opposite from each other with respect to half the drive tone. A dark blue line indicates the resonance with corresponding width in which a signal is amplified. In panel (a) signal and idler are contained in the same resonant mode. In panel (b) the signal and idler are in a separate mode.

2.3.3. Three- and Four-wave Mixing

Up to this point, we discussed parametric amplification in terms of currents and voltages in an LC-resonator. However, for the next part of our discussion it is more convenient to think in terms of single quanta of energy. We will adopt some vocabulary from quantum optics, in specific the term photon, which is a single quantum of an electromagnetic radiation $\hbar\omega$ [42, 43]. In the microwave signals that we are considering, these frequencies are in the gigahertz range. With that in mind we can consider the mixing processes in parametric

interactions. There are two cases to be considered: three-wave mixing and four-wave mixing.

In the three-wave case, a single drive photon interacts with a photon a the signal frequency (ω_s) and a photon at the idler frequency (ω_i), as is illustrated in figure 2.14 (a). This relation can be written as $\omega_d = \omega_s + \omega_i$. In 3-wave mixing processes the signal and idler frequency are typically close $\omega_s \approx \omega_i$. This implies that the drive frequency is approximately at twice the signal frequency $\omega_d \approx 2\omega_s$. In fig 2.14 (b), an LC-circuit in which three-wave mixing occurs. The inductor in this formed by a SQUID, as explained in section 2.2.5. The three-wave mixing occurs by driving the magnetic flux through the SQUID-loop, to change the SQUID inductance. This is called flux-pumping.

As its name suggests, the four-wave case involves four photons: two at the pump frequency, one at the signal frequency and one at the idler frequency. This is illustrated in figure 2.14 (c). It follows $2\omega_p = \omega_s + \omega_i$. The pump frequency in four-wave mixing process is in between the signal and idler frequency. Figure 2.14 (d) demonstrates a circuit in which four-wave mixing occurs. In this circuit, the LC-resonator is driven with an AC current through a transmission line. This is called current-pumping.

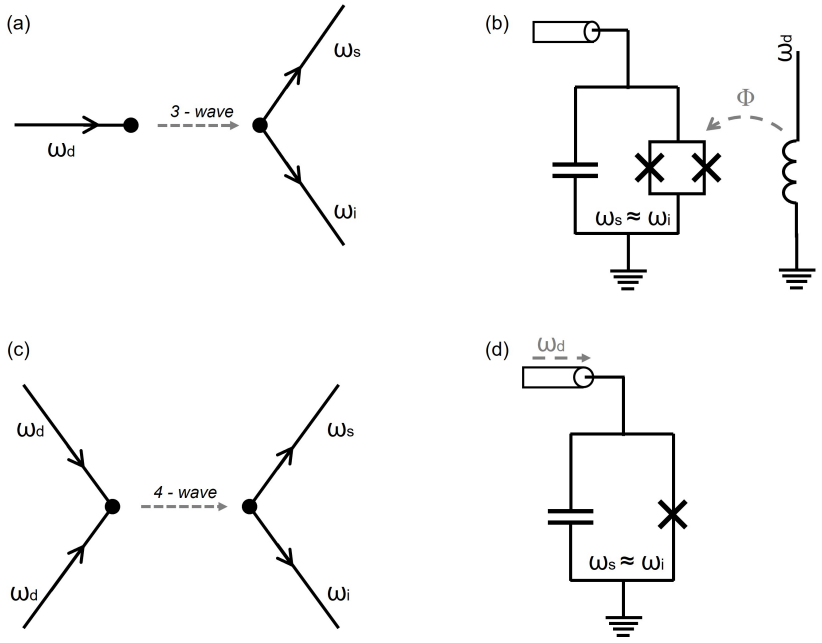

Figure 2.14: Panel (a) shows the relation between incoming drive photons ω_d and outgoing signal (ω_s) and idler (ω_i) photons in a three-wave mixing. Panel (b) demonstrates how three-wave mixing can be realized by applying a time-varying magnetic flux Φ ('flux pumped'). In panel (c) the relation between drive, signal and idler photons in four-wave mixing. Panel (d) shows a circuit model in which four-wave mixing is achieved by applying an AC current at the input transmission line.

2.3.4. Noise in Amplification

Every amplification process adds some degree of noise to an amplified signal. The added noise is defined as all the stochastic fluctuations that are added to a signal. In this section we will consider the basics of noise in parametric amplification. A more thorough discussion is found in [41, 42].

In section 2.1.2 it was demonstrated that the power emitted by an LC-resonator at resonance is purely resistive in nature. Any resistive process adds thermal noise, due to the random motion of electrons in the resistor. The kinetic energy added by this random motion has a kinetic energy, which is proportional to the temperature T of the process. The variance of this process can be expressed as a voltage $V_n(T)$

$$\langle V_n(T)^2 \rangle = 4k_b \Delta f T. \tag{2.55}$$

where k_b is the Boltzmann constant and Δf the frequency bandwidth over which the noise is measured. The power P_n added to the output of the process by thermal noise can now be calculated as

$$P_{\mathrm{n}} = \frac{V_n(T)^2}{2R} = k_{\mathrm{b}} T \Delta f, \tag{2.56}$$

where we defined the process to have a resistance R. Using equation 2.56 we can now define the added noise temperature T_{n}

$$T_{\mathrm{n}} = \frac{P}{\Delta f}. \tag{2.57}$$

This quantity is useful to express the noise characteristics of an amplifier. The noise temperature is the temperature at which the thermal noise would have had the same noise power as all noise added by the amplifier.

In equation 2.55 we made the implicit assumption that we are in the classical limit ($k_{\mathrm{b}} T \gg \hbar\omega$). However, for the JPAs considered in this thesis, this approximation does not hold as they are operated at very low temperatures and at very high frequency. This can be corrected for by multiplying the variance $\langle V_n(T)^2 \rangle$ of the noise with a correction factor $\gamma(\omega)$

$$\gamma(\omega) = \frac{\frac{\hbar\omega}{k_{\mathrm{b}} T}}{e^{\frac{\hbar\omega}{k_{\mathrm{b}} T}} - 1}. \tag{2.58}$$

In the classicial limit of high-temperature and low-frequency, this factor is approximately 1. However, in the experiments in this thesis ($\omega \approx 7$ GHz, $T \approx 300$ mK) it follows that $\gamma(\omega) \approx 1/2$. This correction is large enough that it cannot be neglected.

A Chain of Amplifiers

In a practical measurement setup multiple amplifiers are used to read out a microwave signal. We will demonstrate why in such a chain it is important that the first amplifier adds much gain G to a signal.

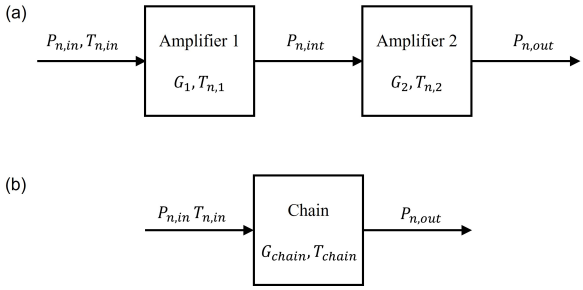

Figure 2.15: A chain of two amplifiers, which are illustrated as square boxes. In panel (a) both amplifiers are shown separately. In figure (b) they are combined and considered as a single amplifier. Figure adapted from [27].

To demonstrate this, we consider a cascade of two amplifiers. This chain is shown schematically in figure 2.15 (a). The amplifiers have gain G_1, G_2 and an added noise temperature $T_{\mathrm{n},1}, T_{\mathrm{n},2}$. An input signal with added noise power $P_{\mathrm{n,in}}$ and noise temperature $T_{\mathrm{n,in}}$ is presented at the input of the chain. In order to calculate the noise power in at the output, we first want to calculate the noise power $P_{\mathrm{n,int}}$ after the signal has passed through the first amplifier

$$P_{\mathrm{n,int}} = G_1 k_{\mathrm{b}} T_{\mathrm{n,in}} \Delta f + G_1 k_{\mathrm{b}} T_{\mathrm{n},1} \Delta f, \tag{2.59}$$

where the noise power is measured over a bandwidth Δf. This is the noise power present at the input of the second amplifier. The noise at the output of the chain now becomes

$$P_{\mathrm{n,out}} = G_2 P_{\mathrm{n,int}} + G_2 k_{\mathrm{b}} T_{\mathrm{n},2} \Delta f = G_1 G_2 k_{\mathrm{b}} \Delta f \left(T_{\mathrm{n,in}} + T_{\mathrm{n},1} + \frac{T_{\mathrm{n},2}}{G_1} \right). \tag{2.60}$$

We now considered both amplifiers in the chain individually. However, we can also consider the chain as a single amplifier, with gain $G_{\mathrm{chain}} = G_1 G_2$ and added noise temperature T_{chain}. This is illustrated in figure 2.15 (b). The output noise power can now be expressed as

$$P_{\mathrm{n,out}} = G_1 G_2 k_\mathrm{b} \Delta f \left(T_{\mathrm{n,in}} + T_{\mathrm{chain}}\right). \tag{2.61}$$

This equation should give the same result as equation 2.60. It follows that $T_{\mathrm{chain}} = T_{\mathrm{n},1} + T_{\mathrm{n},2}/G_1$. The added noise power of the second amplifier is thus suppressed by the gain of the first amplifier. This result can be generalized to a chain of an arbitrary number of amplifiers. The added noise temperature now becomes

$$T_{\mathrm{chain}} = T_{\mathrm{n},1} + \frac{T_{\mathrm{n},2}}{G_1} + \frac{T_{\mathrm{n},3}}{G_1 G_2} + \cdots, \tag{2.62}$$

The added noise temperature is thus suppressed by the gain of all previous amplifiers. The same holds for the added noise power. For this reason, having a first amplifier with a low added noise temperature is crucial in order to have low added noise power.

Noise in Wave Mixing Processes

In section 2.3.3 we considered the wave-mixing processes that are necessary to amplify a signal in JPAs. We will now consider the noise in these processes. The argument is discussed more thorough in [43].

We consider process in which an input at a signal frequency ω_s and idler frequency ω_i are mixed. It is assumed that the idler frequency falls outside the measured bandwidth Δf. The process occurs at low temperature and microwave frequencies, such that $k_\mathrm{b} T \ll \hbar\omega_s$. In this regime the added noise power becomes a frequency-dependent quantity. The added noise power $P_{\mathrm{n,\,out}}$ is now determined by the relation [43]

$$\hbar\omega_s P_{n,\mathrm{out}} = \hbar\omega_s G P_{\mathrm{n,in}}(\omega_s) + \hbar\omega_s (G-1) P_{\mathrm{n,in}}(\omega_i), \tag{2.63}$$

where G is the gain of the process. The added noise in this process comes from the mixing with input at the idler frequency. In absence of any signal, this has variance noise power $P_{\mathrm{n,in}}(\omega_i) = 1/2$[43]. The minimum added noise temperature T_n of the process now becomes

$$T_\mathrm{n} = \frac{\hbar\omega_s (G-1) P_{\mathrm{n,in}}(\omega_i)}{k_\mathrm{b} G} = \frac{\hbar\omega_s}{2k_\mathrm{b}}, \tag{2.64}$$

under the assumption that $G \gg 1$. The minimum added noise of wave mixing processes is thus equal to half a photon of energy at the signal frequency.

2.4. Kerr-Nonlinearity in a Josephson Parametric Amplifier

In the previous section the concept of parametric amplification was discussed. By parametrically driving an LC-resonator a signal current can be amplified. As a next step we will show how parametric amplification in a JPA occurs. We will first derive the Kerr Hamiltonian for a simple JPA starting from a circuit model in terms of charge and phase operators. Subsequently, it will be shown that the amplification in this JPA is due to its Kerr-nonlinearity. Lastly, we will discuss two effects limiting this gain that occur due to the presence of this Kerr-nonlinearity. This part of the discussion follows the approach set out by Eichler [20] and Planat [44].

To start our discussion, we return to the essence of parametric amplification. In section 2.3, we saw that parametric amplifiers create gain by modulating a single parameter of a system.

2.4.1. The Kerr Hamiltonian

A simple JPA consists of a SQUID parallel to a capacitor C. The SQUID has a flux-tunable inductance $L(\Phi)$, as was shown in section 2.2.5. This circuit is effectively an LC-resonator, which is connected to a transmission line. The resonance frequency of this circuit is $\omega_0 = 1/\sqrt{L(\Phi)C}$. In section 2.3.1 it was demonstrated that periodic variation of the resonance frequency of such a resonator can amplify a signal. In this JPA this is done by modulating the SQUID inductance with a time-varying magnetic field. We will derive how a signal is amplified in this device, which is depicted in figure 2.16. We start from a circuit model in terms of charge and phase operators.

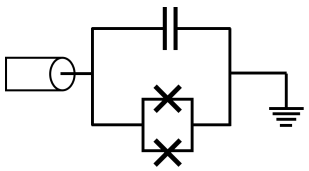

Figure 2.16: The circuit model of a simple JPA consisting of a SQUID shunted by a capacitor.

The Hamiltonian is the sum of the kinetic and potential energy stored in a system. We can write the Hamiltonian of this JPA in terms of charge $\hat{q}$ and flux $\hat{\varphi}$ operators

$$\hat{H} = \frac{\hat{q}^2}{2C} + E_J \cos\hat{\varphi}. \tag{2.65}$$

The first term on the right side represent the energy stored in the capacitor and the second term is the potential energy stored in the Josephson junction. E_j is defined using equation 2.40. This potential is nonlinear, which is enables the parametric driving. The operators $\hat{q}$ and $\hat{\varphi}$ can be understood as the quadratures of a signal from 2.3.1. Together they form a non-conjugate pair, that is to say $[\hat{q},\hat{\varphi}] = -2ie$.
To understand the amplification process, we will rewrite the Hamiltonian in terms of the creation (annihilation) operator $\hat{a}$ ($\hat{a}^\dagger$). The creation (annihilation) operator increases (decreases) the number of photons inside the JPA by 1. They can thus be used to describe the electromagnetic field inside the JPA. The creation and annihilation operators are related to the flux and charge operators by

$$\hat{q} = q_{zpf}(\hat{a} + \hat{a}^\dagger), \tag{2.66a}$$

$$\hat{\varphi} = \varphi_{zpf}(\hat{a}^\dagger - \hat{a}), \tag{2.66b}$$

where $q_{zpf} = \sqrt{\frac{\hbar\omega C}{2}}$ and $\varphi_{zpf} = \sqrt{\frac{\hbar}{2\omega C}}$. The subscript zpf stands for zero-point fluctuations. This is the variance of the vacuum fluctuations of the respective operator, when it is in its ground state. It is possible to substitute these relations in the Hamiltonian of equation 2.65. However, due to the cosine potential the resulting equation contains many terms and higher-order terms have to be neglected. As these steps are mathematically tedious, they are omitted here. The interested reader is referred to [44]. The resulting Hamiltonian is

$$\hat{H} = \hbar\omega_0 \hat{a}^\dagger \hat{a} + \hbar\frac{K}{2}\hat{a}^\dagger \hat{a}\hat{a}^\dagger \hat{a}. \tag{2.67}$$

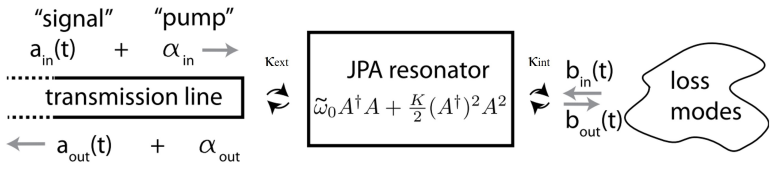

Figure 2.17: Schematic depiction of the input-output model. The JPA is modelled as a Kerr-oscillator with the corresponding Hamiltonian. On the left side it is coupled to a transmission line with coupling κ_{ext}. Through this line an input field $\hat{a}_{\text{in}} + \alpha_{\text{in}}$ enters the JPA and an output field $\hat{a}_{\text{in}} + \alpha_{\text{in}}$ comes out. On the right side the losses internal to the JPA are modelled with decay rate κ_{int}. Figure adapted from [20].

The first term on the right can be recognised as the energy levels of a quantum harmonic oscillator. The second term is known as the Kerr-nonlinearity. The chosen expression for the Kerr-term, expresses the non-linearity up to the third order. We introduced the effective Kerr constant $K = -\frac{E_J}{2\hbar}\left(\frac{\phi_{zpf}}{\Phi_0}\right)^4$ to simplify our notation. The Kerr-nonlinearity is necessary to demonstrate how amplification occurs in this system.

The Hamiltonian in equation 2.67 describes the fields inside the JPA in terms of photon number. To see this we consider that the photon number operator is equal to $\hat{n} = \hat{a}^\dagger \hat{a}$. To understand how gain arises in this JPA, we want to model its output field when due to an input field. This can be done via the input-output formalism. The solutions that we obtain using this approach are referred to as resonant modes, which are periodic distributions of the electromagnetic field.

The approach is schematically shown in figure 2.17. An input field A_{in} is presented at the entrance of the JPA. This input field affects the field inside the JPA A which behaves as described by the Hamiltonian 2.67. This intra-JPA field can be considered as the currents resonating inside the LC-resonator. The JPA then sends an output field A_{out} into the transmission line. This field is determined by the field inside the JPA $\hat{a}$. The internal losses will be neglected in the rest of this derivation, because they are much smaller than the coupling of the JPA to the transmission line. This coupling is described by the decay rate κ_{ext}. Losses internal to the JPA are described by κ_{int}. The internal losses κ_{int} of the JPA are assumed to be much smaller than the coupling via κ_{ext}. Therefore it follows that the decay rate $\kappa \approx \kappa_{ext}$.

The three fields in figure 2.17 can respectively be written as

$$\begin{aligned} A_{in} &= \alpha_{in} + \hat{a}_{in}(t), \\ A &= \alpha + \hat{a}(t), \\ A_{out} &= \alpha_{out} + \hat{a}_{out}(t) \end{aligned} \tag{2.68}$$

Equations 2.68 shows that the input, output and intra-JPA field each consist of two parts. A classical field part $(\alpha_{in}, \alpha_{out}, \alpha)$ and a quantum signal $(\hat{a}_{in}, \hat{a}_{out}, \hat{a})$. The classical field part of A_{in} is considered to be due to the parametric driving at frequency ω_d. The quantum field can be considered to be the signal that we want to amplify. We assume that the power of the drive field $|\alpha_{in}|^2$ is much larger than the power of the input signal $\langle \hat{n}_{in} \rangle = \langle \hat{a}_{in}^\dagger \hat{a}_{in} \rangle$ and output $\langle \hat{n}_{in} \rangle = \langle \hat{a}_{out}^\dagger \hat{a}_{out} \rangle$ signal field. This is known as the stiff pump approximation [20]. This approximation allows us to consider the strength of the pump field to be constant for the entire amplification process.

The dynamics of the intra-JPA field A can now be described by an equation of motion [44]

$$\dot{A} = -i\omega_0 A - jKA^\dagger AA - \frac{\kappa}{2}A + \sqrt{\kappa}A_{in} \tag{2.69}$$

In this equation the coupling κ to the transmission line shows up twice: photons from the input field are added to the intra-JPA field and photons from the intra-JPA field are added to the output field A_{out}. The output field A_{out} appears when we introduce a boundary condition at the interface of the JPA with the transmission line. There it should hold that

$$\sqrt{\kappa}A = A_{out} + A_{in}. \tag{2.70}$$

We can now solve the input-output equation 2.69 for the signal part of these fields. The The complete derivation is lengthy and is not relevant for the purpose of this thesis. Therefore, only the result is presented. The full derivation is presented by Eichler [20]. The approach followed in this derivation is set apart briefly.

The approach followed by Eichler is to first solve equation 2.69 for a classical field α when no quantum signal is present ($\langle \hat{a} \rangle = 0$). The solution to this is an operating point for the pump field strength and frequency. The next step in finding the gain of the JPA is to linearize the input-output equation 2.69 around this operating point. The linearized input-output equation can then be solved for the weak quantum signal field. This gives a relation between $\hat{a}_{out}$ in terms of $\hat{a}_{in}$.

The dynamics of this relation are determined by four quantities, which are made dimensionless by scaling them with the decay rate κ of the JPA. These quantities are

$$\delta \equiv \frac{\omega_d - \omega_0}{\kappa}, \quad \tilde{\alpha}_{in} \equiv \frac{\sqrt{\kappa}\alpha_{in}}{\kappa}, \quad \xi \equiv \frac{K|\tilde{\alpha}_{in}|^2}{\kappa}, \quad n \equiv \frac{|\alpha|^2}{\tilde{\alpha}_{in}}. \tag{2.71}$$

The parameter δ is the dimensionless detuning between the drive frequency and resonance frequency of the JPA, $\tilde{\alpha}_{in}$ is the dimensionless drive amplitude, ξ is the product of input drive power and Kerr-nonlinearity and l n is the mean number of photons in the classical part of the intra-JPA field relative to the input drive power.

The resulting equation that links the input and output field is expressed in terms of their frequency content. That is to say, $\hat{a}_{in}(\omega)$ and $\hat{a}_{out}(\omega)$ are functions of frequency. The equation linking them is [20]

$$\hat{a}_{out}(\Delta) = g_s \hat{a}_{in}(\Delta) + g_i \hat{a}^{\dagger}_{in}(-\Delta), \tag{2.72}$$

with $\Delta = (\omega_\mathrm{d} - \omega_\mathrm{s})/2$ the detuning between signal and pump, normalized by the linewidth κ. g_s and g_i are the gain at respectively signal and idler frequency. This equation shows that the output field at the signal frequency is the result of mixing the input at the signal and the idler frequency, which are amplified with their respective gain. This kind of wave mixing processes was introduced in section 2.3.3. The gain at both signal and idler can be expressed in terms of the pump parameters from equation 2.71

$$g_s = -1 + \frac{i(\delta - 2\xi n - \Delta) + \frac{1}{2}}{(i\Delta - \lambda_-)(i\Delta - \lambda_+)}, \tag{2.73a}$$

$$g_i = \frac{-i\xi n \exp^{2i\phi}}{(i\Delta\omega - \lambda_-)(i\Delta - \lambda_+)}, \tag{2.73b}$$

where $\lambda_\pm = \frac{1}{2} \pm \sqrt{(\xi n)^2 - (\delta - 2\xi n)^2}$ is used to simplify both expressions. The four dimensionless quantities from equation 2.71, together with the detuning Δ, determine the dynamics of equations 2.73a and 2.73b. The gain of the input at the signal and idler is typically expressed in terms of the the magnitude $|g_s|^2$ and $|g_i|^2$. The presence of an idler reveals that this is phase-preserving gain, as discussed in section 2.3.2. The detuning of signal and idler are mirrored around the drive frequency, revealing that this is a four-wave mixing process.

The gain in this model is derived from the Kerr-nonlinearity. This can be observed from the parameter ξ. If this parameter is zero, then g_i becomes zero as well and the mixing breaks down. In that case it follows from equation 2.72 that an output field the signal frequency is only due to an input at the signal frequency. The parameter ξ also reveals that small Kerr-nonlinearity can be compensated by increasing the strength of the pump field. This is approximation that can be made due to the stiff approximation. However, the stiff pump approximation breaks down if the signal field becomes too large. The consequence is that at too large signal power, the gain starts to decrease. This is called amplifier saturation. Section 2.4.2 explores this phenomenon.

Another limiting case of the operation of our JPA stems from the zero-point fluctuations that are present at the signal and idler frequencies. If the drive strength of the JPA is sufficiently strong, these fluctuations will be amplified. The result is that it appears as if the device spontaneously emits microwave radiation [43]. In this regime the resonant mode is said to be self-oscillating. Self-oscillations are discussed in section 2.4.3

2.4.2. Mechanisms of Amplifier Saturation

Until now, we assumed that input signals to our JPA were small enough to prevent amplifier saturation. However, in practice amplifier saturation cannot always be avoided and should thus be considered. The power at which saturation set in, is defined as the power at which the maximum signal gain decreases by 1 dB. This power is aptly named the 1dB-compression point P_{1dB}. There are two mechanisms responsible for amplifier saturation. It is not our goal to give an in depth discussion on these saturation mechanisms, for that purpose the reader is referred to [44–46]. Here the discussion is limited to giving a qualitative explanation of both mechanism and we will focus on a strategy for mitigating them.

The first mechanism is rather intuitive. We discussed the assumption that the power of the drive field could be considered to be constant, because it was much larger than that of the signal field. If the input signal becomes sufficiently large, this does not hold any more and the stiff pump approximation breaks down. We have seen that our flux-pumped JPA was a four-wave mixing amplifier. That is to say that two photons at the drive frequency are converted in a photon at the signal and idler frequency: $2\omega_p = \omega_s + \omega_i$. For an amplification process with a signal gain of N photons, this requires $2N-1$ pump photons. Consequently, if the signal strength is too large (and thus contains too many signal photons), there are not enough photons to keep the amplification process ongoing.

The second mechanism is more fundamental and originates from the Kerr-nonlinearity. It is generally agreed upon that this is the more dominant mechanism in JPA saturation [20, 44, 45]. The input-output equation 2.69 described the dynamics of the drive field in our flux-driven JPA. In this approach Kerr-terms that took into account the number of signal photons in the field $A(t)$ inside the JPA - that is to say depend on $\hat{n} = \langle \hat{a}^\dagger \hat{a} \rangle$ - were neglected while solving the input-output equation. We will now consider the effect of two terms, that were previously neglected, that take into account this intra-JPA field, namely $2iK\langle \hat{a}^\dagger \hat{a} \rangle \alpha$ and $iK\langle \hat{a}^2 \rangle \alpha^*$ [20]. Adding these terms to equation 2.69 allows to compute the intra-cavity photon number $\hat{n}$ as a function of the input signal field. This can be done computationally, as is done in [44] and [45]. This results in a shift Δf_0 of the JPA-resonance frequency towards lower frequencies. Consequently, the optimal drive frequency is also shifted and the achieved gain decreases. For an input power of n_s signal photons, this shift $\Delta\omega_0 \approx 2\pi n_s \cdot K/\kappa$. For an explanation in physical terms, we turn to the expression we found for the resonance frequency in section 2.4.1: $\omega_0 = 1/\sqrt{L(\Phi)C}$. We also consider that a large input signal, also leads to a large current across the SQUID. In our expression for the Josephson inductance $L_{SQ}(\Phi)$ of a SQUID, we considered that the phase jump φ across the SQUID would be small. However, once the current through the Josephson junction approaches the critical current, the phase jump δ_{avg} increase proportionally. This results in a lower $L_{SQ}(\Phi)$ and consequently a lower resonance frequency.

In summary, there are two mechanisms behind amplifier saturation. The first mechanism is the depletion of the number of photons at the drive frequency. This disables the four-wave mixing process. The second mechanism is a downward frequency shift Δf_0 of the resonance frequency of the JPA if the population of the intra-JPA field increases. This shift is induced by the Kerr-nonlinearity.

2.4.3. Bifurcation and Self-Oscillations

In our treatment of the JPA we assumed that any output of the device is the result of input at the signal and idler frequency. However, it is possible that the input field at these frequencies is approximately zero. The response of a system in absence of any input is referred to as self-oscillations [1]. Different manifestations of the phenomenon are investigated theoretically in [43] and [47]. This section wil briefly discuss the origin and characteristics of self-oscillations.

To understand the origin of self-oscillations, we remind the reader that our JPA is a damped, driven nonlinear oscillator. A resonant mode of this system is driven below its resonance frequency. Initially the driving is weak and results in a small oscillation. Next the drive amplitude is increased slowly in a gradual manner. At a certain drive strength the system becomes unstable, causing it to switch to a high amplitude oscillation. The minimum drive strength of this switch is known as the bifurcation threshold. Its naming indicates that above this threshold, the system is bistable and can exhibit either high or low amplitude oscillations [48]. The high

[1] In some literature the same phenomenon is referred to as parametric oscillations.

amplitude oscillations are what we call self-oscillations.

Kamal et al. [43] proved that the bifurcation threshold coincides with a maximum in the emitted noise power integrated over the oscillator bandwidth. This suggest that a wave mixing process of noise at the signal and idler frequencies, is the origin of self-oscillations. Once the system is self-oscillating the amplified noise provides an external channel at the mode resonance at which the mode leaks drive power. Once a JPA resonant mode is self-oscillating, the amplitude of the self-oscillations grows with drive power [49]. The complex phase at the signal and idler frequencies is evenly distributed between $-\pi$ and π. However, the sum of the phases at signal and idler frequencies is fixed. The sum-value is determined by the drive strength and the decay rate of the mode [47].

In this thesis self-oscillations are investigated in the context of JPAs. The bifurcation threshold forms a limit to the drive strength that can be used to drive our JPA. Above this limit, the device emits radiation at its resonance frequency and does not function purely as an amplifier. However, the emitted radiation has a limited bandwidth. This can make it a potential source of electromagnetic radiation at cryogenic temperatures.

2.5. Engineering the Mode Structure of Josephson Junction Arrays

In section 2.4.2 the mechanisms that cause saturation of gain in JPAs were discussed. Naturally, the question arises how we can mitigate saturation effects in JPAs. An evident approach is to decrease the phase jump φ across the SQUID. It turns out that this is possible by replacing the single SQUID in our JPA by an array of N SQUIDs with the same Josephson inductance. This section investigates the resonant modes in such an array. First the mode structure and Kerr-nonlinearity in a SQUID array are discussed. The next subsection 2.5.2 discusses how this mode structure can be engineered.

The motivation for studying SQUID arrays as JPAs is that they mitigate the effects of amplifier saturation. It was discussed in section 2.4.2 that the phase jump φ over a single SQUID induced this effect. In a SQUID array total phase jump φ_{tot} across the array stays equal, but the phase jump across each SQUID is now $\varphi = \varphi_{tot}/N$. The effect of this approach is increased if the Josephson junctions in the array have an N times larger critical current I_c. The phase jump is then decreased by N^2 even [18, 44]. The smaller phase jump over each SQUID causes amplifier saturation to set in at higher drive power.

2.5.1. Resonant modes in SQUID arrays

To understand the behaviour of SQUID arrays as JPAs, we want to understand the mode structure inside these devices. To this purpose we consider an array of SQUIDs and model each one as an individual LC oscillator, described by an inductance L_J and capacitance C_J. The aim of this approach is to find the mode structure of this SQUID array. However in contrast to the single SQUID JPA, the spatial length of a SQUID array is not negligible. As a result, the electromagnetic fields in this array form a standing wave pattern, consisting of currents oscillating at different resonance frequencies. The total length of the array is comparable to the wavelength of the individual modes, which is similar to how electromagnetic fields behave in a transmission line from section 2.1.3

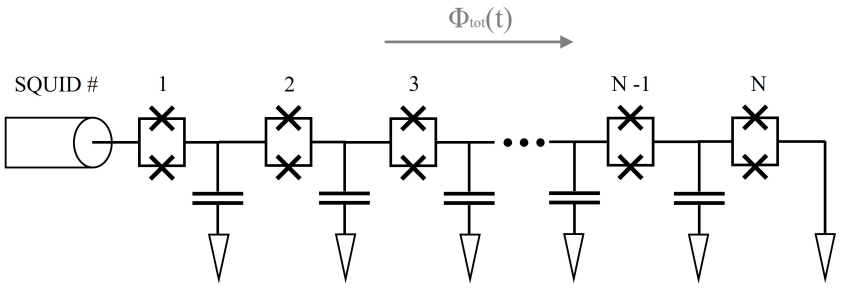

Figure 2.18: Circuit model of a JPA consisting of an array of N SQUIDs. Each SQUID is shunted to ground via a capacitance C_g. In parallel to each SQUID is a capacitance C_{SQ}, which is not shown. A magnetic flux Φ_{tot} pierces the combined SQUIDs in the array.

The circuit model for a SQUID array consisting of N SQUIDs in series is illustrated in figure 2.18. The SQUIDs are labelled $i = 1, 2...N-1, N$. All SQUIDs have the same SQUID inductance $L_{SQ}(\Phi)$ and Josephson Energy E_j. In parallel to each SQUID is a capacitance C_{SQ}. Additionally, each SQUID is coupled to ground via a capacitance C_g. A total flux Φ_{tot} is distributed evenly through the SQUID loops. The Hamiltonian of the circuit can again be found by summing the kinetic and potential energy in the circuit [50]

$$\hat{H} = \sum_{i=1}^{N} \frac{\hat{q}^2}{2C_{SQ}} + \sum_{i=1}^{N-1} E_j \cos\left(\hat{\varphi}_{i+1} - \hat{\varphi}_i\right), \tag{2.74}$$

where the operator $\hat{q}$ correspond to the charge on the capacitor C_{SQ}. The operator $\hat{\varphi}_i$ is the phase over each SQUID. As the SQUIDs are all equal, the phase jump over each SQUID is the same as well. This reveals that the phase over each resonator is indeed $1/N$ times the phase jump over the complete array. This equation bears similarity to the Hamiltonian from equation 2.65. The array is in fact considered as an array of N LC-resonators. Each of those resonators is a distribution of the electromagnetic field, which we will refer to as a mode. The individual resonators can be compared to the simple JPA from section 2.4.

We want to express this Hamiltonian in equation 2.74 in terms of creation (annihilation) operators $\hat{a}$ ($\hat{a}^\dagger$) to demonstrate the form of the Kerr-nonlinearity in this array. This full derivation can be found in [50, 51]. Here we will present the result. This Hamiltonian in terms of creation and annihilation operators reads

$$\hat{H} = \sum_{i=0}^{N-1} \hbar\omega_i \hat{a}_i^\dagger \hat{a}_i - \sum_{i=0}^{N-1} \frac{\hbar}{2} K_{i,i}\omega_i \hat{a}_i^\dagger \hat{a}_i \hat{a}_i^\dagger \hat{a}_i - \sum_{i,j=0}^{N-1} \frac{\hbar}{2} K_{i,j}\omega_i \hat{a}_i^\dagger \hat{a}_i \hat{a}_j^\dagger \hat{a}_j \tag{2.75}$$

The creation and annihilation operators are labelled using index i to indicate to which mode they respectively add or remove a photon. The first term on the right-hand side is the energy stored in N quantum harmonic oscillators, that resonate at their respective mode frequencies ω_i. The second term is dependent on depend on the self-Kerr coefficient $K_{i,i}$ of a mode i. This is the nonlinearity equivalent to the Kerr-nonlinearity in the Hamiltonian of equation of equation 2.67. The third term also depends on a Kerr-nonlinearity. However, this is the cross-Kerr nonlinearity $K_{i,j}$ of a mode i acting on mode j. The Kerr-coefficients $K_{i,i}$ and $K_{i,j}$ can be expressed as [44]

$$\begin{aligned} K_{i,i} &= \frac{2\hbar\pi^4 E_J \eta_{ii}}{\Phi_0^4 C_{\mathrm{SQ}}^2 \omega_i^2}, \\ K_{i,j} &= \frac{4\hbar\pi^4 E_J \eta_{ij}}{\Phi_0^4 C_{\mathrm{SQ}}^2 \omega_i \omega_j}. \end{aligned} \tag{2.76}$$

The expressions for both Kerr-nonlinearities bear resemblance to each other. The primary difference is that the cross-Kerr nonlinearity depends on the resonance frequencies of two different modes i and j, whereas the Self-Kerr nonlinearity only depends on a single mode i. They both depend on a dimensionless factor $\eta_{i,j}$. This is a geometric factor that describes the spatial distribution of the modes in terms of the capacitances C_{g} and C_{SQ}. The appearance of this geometric factor in the Kerr-nonlinearoty, reflects that we cannot neglect the total spatial length of the SQUID array. The different modes ω_i can still be considered as individual LC-resonators. However, the oscillating currents corresponding to each mode ω_i are not spatially localized in a single SQUID, but distributed over the whole array instead. As a result the frequencies of each mode can be found by solving an eigenvalue problem that depends on the array parameters C_{g}, C_{SQ} and L_{SQ} [51].

In subsection 2.4.2 it was discussed that if the photon population of a resonant mode ω_i increases, the Kerr-nonlinearity induces a negative frequency shift of the resonance frequency of this mode. The self-Kerr nonlinearity induces this shift in the modes of a JPA array when their population increases. The cross-Kerr nonlinearity induces a shift of the mode frequency ω_i that increases linearly with the photon number in mode ω_j [51]. The dependencies of the mode frequencies have to be taken into account when parametrically driving a SQUID array. If the drive power becomes to large, the mode will shift away. As a result the wave mixing condition for parametric gain is not met anymore and an incoming signal is not amplified. In the next section a method to engineer the distribution of the resonant modes frequencies is discussed.

2.5.2. The Dimer Josephson Junction Amplifier Array

In the first part of this chapter we developed a formalism to discuss the processes that occur in JPAs and we saw how a signal is amplified in such a device. It was then explained how JPAs consisting of arrays of SQUIDs can mitigate effects of amplifier saturation. The JPA design that is central to this thesis is a modified SQUID array JPA. The crucial modification is the addition of a large capacitor C_c that splits the array in two halves. Figure 2.19 shows how this capacitor fits in the circuit diagram of a SQUID array. The resulting device is called a Dimer Josephson Junction Array Amplifier (DJJAA) [18]. The purpose of adding this capacitor to engineer the mode structure and Hamiltonian of the device compared to the SQUID array from the previous section. This section will discuss how this is done.

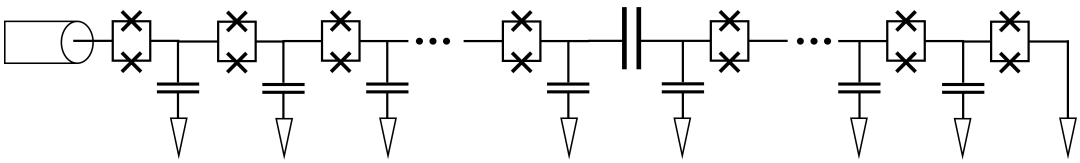

Figure 2.19: The circuit model for a DJJAA. The black crosses represent a Josephson junction. The circuit model resembles that of a SQUID array. The difference is the addition of a central capacitor in series C_c, which is shown in the middle of the figure.

If we derive the Hamiltonian of this circuit from its Lagrangian, we find that the Hamiltonian is similar to that of a SQUID array, with the Hamiltonian from equation 2.76. The gain around the individual mode frequencies can be described using equation 2.72 for this device. To understand the engineering of the mode structure, we model the DJJAA as two separate SQUID arrays, which have the same number of SQUIDs. They are coupled through the center capacitor. Each array can be replaced by an equivalent LC-resonator circuit, where we consider the inductor L to be a SQUID. This model is shown in figure 2.20 (a). Both LC-resonators in this model have the same resonance frequency. The capacitative coupling between both resonators can be described using an interaction term in the Hamiltonian [19]

$$H_{int} = -\hbar g\left(\hat{a}^\dagger \hat{b} + \hat{a}\hat{b}^\dagger\right), \tag{2.77}$$

where the notation $\hat{a}$ ($\hat{a}^\dagger$) and $\hat{b}$ ($\hat{b}^\dagger$) are use to distinguish between the creation (annihilation) operators corresponding to the two different resonators. g is a constant that captures the strength of the coupling between the resonators. This interaction Hamiltonian is known as the beamsplitter Hamiltonian. It describes two coupled harmonic oscillators. It follows from this Hamiltonian that the two cavities exchange photons at a high rate. [19]. The result is that the resonant modes of both resonators with same frequency are shifted. The resonant frequency of the first resonator is shifted slightly upward, whereas that of the second is shifted slightly downwards. The two modes now have a limited separation in frequency. The resulting mode structure is shown in figure 2.20 (b) . It can be seen that the modes are divided in pairs, which from hereon we will refer to as dimers. Each dimer can be driven to create nondegenerate gain, in which both signal and idler experience significant amplification, as illustrated in the inset of figure 2.20 (c).

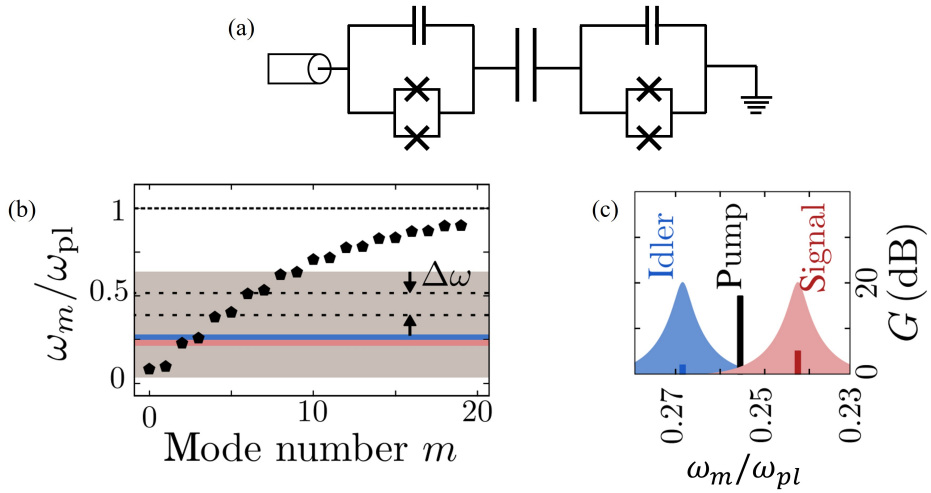

Figure 2.20: (a) shows a DJJAA modelled as two separate LC-resonators. This model shows how capacitative coupling between two resonators is used to engineer there mode structure such that they form dimers. In (b) the mode structure of a DJJAA is plotted. The resonance frequency of a mode m is plotted normalized to the plasma frequency. Plot (c) shows how nondegenerate gain can be created by placing a pump tone between the signal (blue) and idler (red). This is illustrated for the modes marked by the dotted lines in (b). Figure (b) and (c) are adapted from [18].

2.6. Fabrication

So far, the discussion focussed on the theoretical concepts behind JPA's. However, the scope of this thesis project was to produce a working DJJAA. Therefore, this section introduces the theory behind the different fabrication techniques that were used in the DJJAA recipe in section 3.2.1. The structures on a DJJAA have dimensions of several microns. These structures are fabricated on a solid basis, called the substrate or bulk. The device is then build in an additive manner: the comprising structures are deposited on the substrate layer-by-layer. These layers are called thin films, indicating that their thickness is much smaller than that of the substrate. To deposit a single thin film, several different technologies are necessary. In the case of DJJAAs, these technologies are optical lithography, evaporation and ion beam etching. In the following subsections we will discuss all three technologies separately. The chapter is then concluded with a section about inspection of junctions. The book by Fransilla [52] served as a useful reference for writing this chapter.

2.6.1. Optical Lithography

Optical lithography is a means to reproduce the geometrical patterns in chip design data as physical structures. In case of optical lithography this is often done by exposing a photo-sensitive polymer to ultraviolet (UV) light. This exposure changes the chemical properties of the polymer, which allows its removal at designated areas. These photo-sensitive polymers are commonly called photoresist. Photoresist comes in two flavours: positive and negative resist. The difference is illustrated in figure 2.21. A positive resist becomes soluble in developer once it has been exposed. In contrast, in a negative photoresist the exposed polymer is hardened by forming crosslinks between polymer chains. The choice for a particular resist is dependent on the geometries that one wants to pattern. The type of resist used during fabrication of DJJAAs is discussed in section 3.2.2.

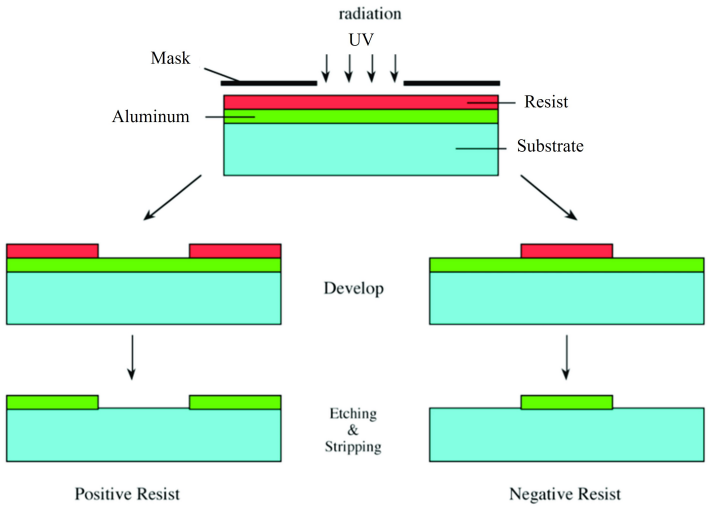

Figure 2.21: The difference between positive and negative photoresist. Figure adapted from [53].

The thickness of the photoresist layer influences the parameters of the exposure: a thicker resist layer requires a higher UV intensity. To ensure that the exposure is equal everywhere, it is thus essential that the thickness is uniform across the substrate. To create a uniform resist layer, a technique called resist spinning is applied. This is done by first placing the sample on a chuck, which can clamp the sample using a vacuum. Then one can apply resist onto the sample surface until the whole sample is covered. However, the resist is not uniform yet. Therefore, the chuck is rotated at a high speed, typically up to 6000 rpm. The result is a very uniform resist layer. The thickness can be controlled by varying the total rotation time and speed. The resist still contains solvent. To drive out the solvent from the resist, the sample is baked for several minutes after spinning.

One typically wants to create well-defined structures onto the sample. To properly define those, exposure is typically done with a laser. The laser draws the pattern where resist has to be removed if a positive resist is used. If a negative resist is used, the laser follows the areas where resist has to remain on the sample.

2.6.2. Physical Vapor Deposition

Physical Vapor Deposition (PVD) is the process of material ejection from a solid target, which is placed in a crucible. The ejected material is then transported through a vacuum to the substrate surface, onto which the material is deposited. PVD is used to create the thin films that together form a DJJAA. Methods for PVD differ in their means of removing atoms from the solid target. Here we will focus on a method called evaporation. In evaporation the crucible consists of a metal, which is heated locally with an electron beam gun. The process takes place in a high vacuum. The electron beam heating causes the metal to vaporize. Transport to the substrate is realized by the high vapor pressure of metals: The metal atoms in the vapor experience a high pressure near the solid target and move to the substrate along the resulting pressure gradient. Evaporation is shown schematically in figure 2.22. The mean-free path is the distance which vapor atoms move without collisions. This distance is typically much larger than the vacuum chamber in which the process takes place.

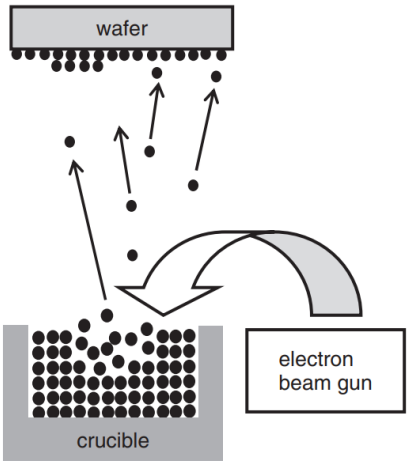

Figure 2.22: A schematic depiction of evaporation, which was adapted from [52].

Evaporation is a PVD method which can be carried out with a vacuum chamber at low temperature. Heating only occurs at the crucible. This low deposition temperature and the small transport distance of the atoms, makes evaporation a directional process. This means that evaporation only occurs at the substrate surface and not on sidewalls of edges and holes. The directionality of evaporation is exploited in fabrication of Josephson junctions, which often requires deposition under specific angles.

2.6.3. Ion Beam Etching

Ion beam etching is a means of mechanically cleaning a surface. This technique bombards a surface with ions to remove unwanted material. Atoms of unwanted material are knocked out of the lattice due to momentum and energy transfer with the impending ions. A typical ion beam etching setup is shown in figure 2.23. The process is carried out in a vacuum chamber under high vacuum. Gas atoms enter via an inlet and are then ionized using a hot filament. They are then directed towards the substrate by means of an electric field [54].

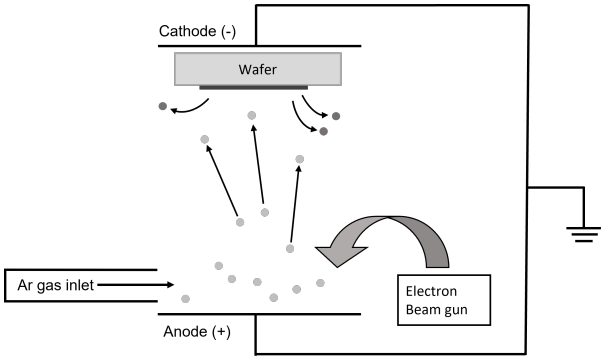

Figure 2.23: A schematic of an argon milling setup

The efficiency of the process is measured in terms of the number of knocked out atoms per incoming ion. This is called sputter yield. The sputter yield can be influenced by various parameters. The energy of incoming ions is varied by changing beam energy, typically between several hundred to thousand Volts [54]. Too low energy prevents removal from any material atoms from their lattice, too high energy causes substrate damage. During ion beam etching the sample is typically rotated, to decrease the influence of the ion angle of incidence on the sputter yield.

In this report, ion beam etching is done using an argon gas to remove native oxides from aluminum. This is called argon milling. It requires careful calibration, as aluminum is etched away approximately ten times faster then native oxides [55]. Argon milling for too long thus causes material damage to aluminum on samples. Section 3.2.3 discusses the calibration of Argon milling for the DJJAA fabrication in this thesis.

2.6.4. Inspection of Josephson Junctions

The JPA devices that were discussed in the previous chapter, require Josephson Junctions to create gain. Section 2.2.5 introduced the SQUID inductance L_{SQ} and showed its relation to the critical current I_c. Fabricating a JPA with a specified operating frequency thus requires fabricating SQUIDs with a specific critical current.

Unfortunately, there is no superconductivity at room temperature. This is unpractical, since one wants to inspect fabricated devices before mounting them in a measurement setup. The solution was derived by Vinay Ambegaokar and Alexis Baratoff [56] in the form of an exact equation

$$I_c = \frac{\pi\Delta(T)}{2R_n e}\tanh\left(\frac{\Delta}{2k_B T}\right). \tag{2.78}$$

This equation relates the resistance R_n of Josephson junctions at room temperature to their critical current I_c. e is the charge of an electron and k_B the Boltzmann constant. The function $\Delta(T)$ describes the superconducting energy gap of the junction as a function of temperature T. The relation is often approximated by assuming a linear dependence of $\Delta(T)$ on T [36]. Equation 2.78 can then be simplified to

$$I_c \approx \frac{2.34\pi k_B}{eR_n}(T - T_c), \tag{2.79}$$

where T_c is the critical temperature of the used superconductor. It is now possible to find the critical current of a Josephson Junction, by simply measuring its resistance at room temperature. Relation 2.79 provides us with a means to test if fabricated junctions have approximately the Josephson inductance that they were designed for, as is discussed in section 3.1.

3

Methods

In this chapter we present the experimental techniques that were used in the experiments during this thesis project. The chapter can be split in two parts. The first part discusses all methods that are necessary before the actual experiment, which are design, fabrication and assembly of DJJAAs. The second part focuses on the actual measurements and consists of a discussion on the experimental setup and measurement techniques.

In section 3.1 the amplifier design and the resulting device parameters are presented. In the next section our fabrication recipe for DJJAAs is discussed. Central to this in the fabrication are overlap Josephson junctions and the issues that are involved in producing them. The first part of this chapter then concludes on the assembly of a DJJAA in its sample holder. This is followed by an introduction of the measurement setup in the Entropy cryostat in section 3.4. The last section in this chapter discusses the measurement techniques necessary for DJJAA measurements.

3.1. DJJAA design

The design for the DJJAA, was kindly shared by Ioan Pop et al. [57]. The design comprises an array of 2×800 SQUIDs with a large central capacitor. The complete design is shown in figure 3.1. The array is meandering, with a single meander containing six SQUIDs. The reader should note that it is important that both halves of the array have an equal number of SQUIDs. If this is not the case the arrays have different resonance frequencies and will not dimerize as a consequence, as discussed in section 2.5.2.

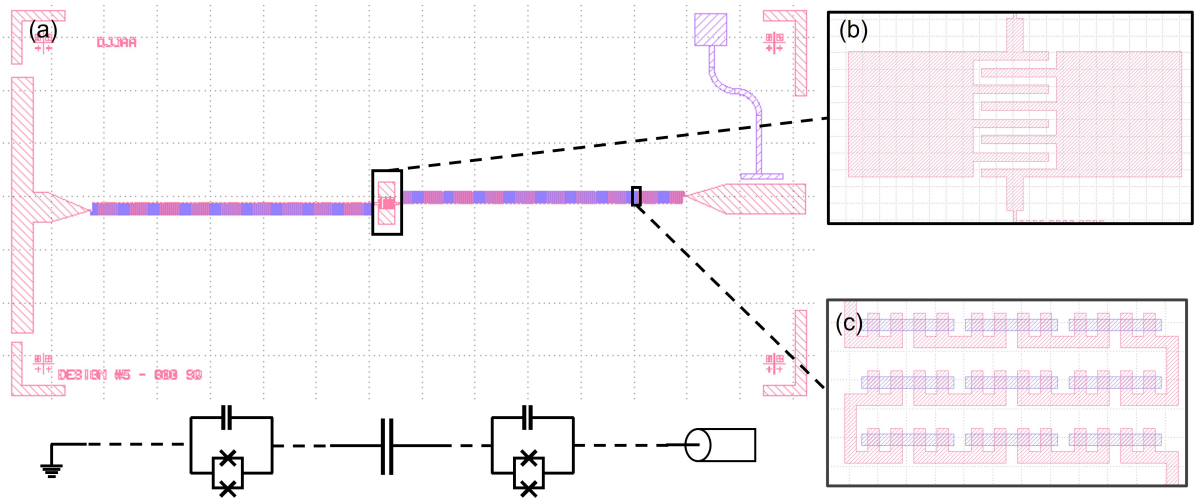

Figure 3.1: The design for a DJJAA is shown horizontally in panel (a). The bottom of the image maps how the different parts of the design are related to an equivalent circuit model. The insets show the central capacitor (panel (b)) and three meanders consisting of six SQUIDs each (panel (c)). The crosses in the cornes of the design are alignment markers for optical lithography.

Before the design was built, simulations were done to understand the frequency behaviour of the DJJAA. The necessary simulations were also shared by Ioan Pop et al.[58]. This section first discusses the inductance participation ratio, which is an important design parameter. Then mode structure and Kerr coefficients resulting from these simulations are summarized. Lastly, we discuss the values for the normal state resistance that flow from the design.

For completeness the inductance participation ratio γ will be discussed. This ratio is a means of comparing the inductance of the SQUID L_{SQ} to the geometric inductance L_{geo} added by the leads of the microstrip

$$\gamma = \frac{L_{\mathrm{SQ}}}{L_{\mathrm{SQ}} + L_{\mathrm{geo}}}. \tag{3.1}$$

This ratio matters for the design, as it affects to what extent the resonance frequencies are flux-tunable. The resonance frequency of a DJJAA can be calculated using

$$f_0 = \frac{1}{\sqrt{LC}} = \frac{1}{\sqrt{(L_{\mathrm{SQ}} + L_{\mathrm{geo}})C}}. \tag{3.2}$$

This resonance frequency can be changed by flux-tuning the SQUID inductance L_{SQ}. However, the geometric inductance L_{geo} is static and cannot be changed. It is thus important that the SQUID inductance is the dominant contribution, which implies that $\gamma \to 1$.

The resonance frequencies and Kerr-coefficients of the modes in our design were calculated numerically. The chosen approach uses 2×2 transfer matrices to calculate these parameters [27]. The resulting parameters are listed in table 3.1. The modes are labelled after the dimer pair they are in. $f_{i,\pm}$ refers to a mode in dimer pair $i = 0, 1, 2, 3$. The subscripts $-$ and $+$ refer to respectively the lower and upper mode of a dimer.

Table 3.1: Overview of the resonance frequencies of the DJJAA design for the first three dimers. In the third row the Kerr self-Kerr coefficients K_{self} for this mode are listed. The fourth row contains value for the decay rate κ of each mode.

Mode index	1	2	3	4	5	6
Mode label	$f_{0,-}$	$f_{0,+}$	$f_{1,-}$	$f_{1,+}$	$f_{2,-}$	$f_{2,+}$
Frequency	1.495 GHz	1.701 GHz	4.565 GHz	5.061 GHz	7.644 GHz	8.129 GHz
Self-Kerr K_{self}	0.482 kHz	0.744 kHz	5.058 kHz	6.274 kHz	13.985 kHz	15.357 kHz
κ	124.2 MHz	163.6 MHz	123.7 MHz	144.2 MHz	106.4 MHz	127.7 MHz

From the simulations, we also extra values related to inspection of fabricated arrays. Section 2.6.4 discussed how the normal state resistance of a Josephson junction can be used to estimate its critical current by using the Ambegaokar-Baratoff formula [56]. The per SQUID resistance in our design is $R_n = 37.5\ \Omega$. This value does not yet take into account the resistance of the aluminium microstrip that connect the junctions. This parameter R_{leads} is calculated for half the junction array. In table 3.2 parameters related to the normal state resistance of a complete DJJAA array are shown. R_{leads} and R_{leads} refer to the resistance of the top (left) and bottom (right) half of the junction array. They can be interpret-ted as the normal state resistance of the resonator before and after the center capacitance in the model presented in section 2.5.2.

Table 3.2: Design parameters related to inspection of the fabricated DJJAA arrays.

# of SQUIDs	R_{leads}	R_{top}	R_{bot}
2×800	5133Ω	35.13 kΩ	34.55 kΩ

3.2. Device Fabrication

Part of this thesis project was focused on fabrication of DJJAAs for future use in the Steele lab. The major challenge in DJJAA fabrication, is making reproducible Josephson junctions within their design specifications. This starts with choosing a suitable type of junction. The most common types of Josephson junction are Dolan bridgde and Manhattan junctions [22]. Both evaporate aluminum at a 45° angle. This is done to prevent evaporation on areas in the shadow of the applied resist layer. A drawback of this technique, is that this angle cannot be kept constant along the entire wafer, resulting in offsets in junction area from design [22]. Therefore, it was decided to instead use overlap Josephson junctions [21]. This type of junction has a fabrication process that involves evaporation of aluminum at a 0° angle, which improves the accuracy and reproducibility. The fabrication process for Manhattan and Dolan bridge junctions is discussed extensively in [22].

In the next section we will discuss all steps involved in the recipe for fabrication of DJJAAs. Subsections 3.2.2, 3.2.3 and 3.2.4 will then delve into specific steps of this recipe that required calibration. The resulting device is shown in section 3.2.5.

3.2.1. Implementation of the Fabrication Recipe

Fabrication was done by using the facilities of the Kavli NanoLab. This section first discusses the overall fabrication process and the steps involved. The recipe was followed is based on a DJJAA recipe that was developed in Karlsruhe by Pop et al.[57]. It was altered in such a way that it could be reproduced reliably in the Kavli Nanolab. Carrying out the whole fabrication recipe takes approximately three days and as a result the recipe could be iterated. In the next subsections the challenges involved in this recipe are discussed. First we discuss the liftoff process that was used and then present a calibration of the utilized argon milling process.

The fabrication of DJJAAs in our recipe is done by depositing two layers of aluminum on a substrate using liftoff. In between deposition of these layers, a thin aluminum-oxide layer is grown on the sample to serve as the insulating barrier in the Josephson junctions. Throughout subsequent fabrication steps, the sample is inspected with an optical microscope to catch potential defects and irregularities early-on. Additionally, at several points in the process, cleaning steps are performed to remove resist residuals and other forms of pollution. The following paragraphs elaborate on the different steps during fabrication, which are also depicted graphically in figure 3.2.

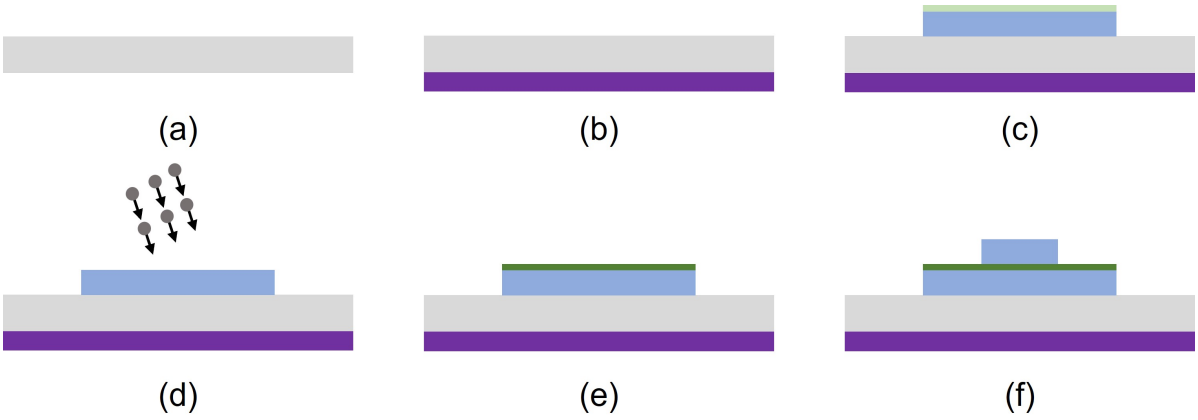

Figure 3.2: Schematic depiction of the different layers that are deposited during fabrication of overlap junctions. Step (a) shows the bare sapphire substrate, in step a complete overlap junctions is fabricated. Applied resist layers before deposition steps are not shown. Step (d) displays the argon milling during fabrication. Different colours correspond to: gray - sapphire substrate, blue - aluminum, dark purple - platinum, light green - native oxides, dark green - regrown oxide barrier.

The substrate that is used, is an 8 x 8 mm insulating Double-Side Polished (DSP) sapphire chip, which has a thickness of 330 µm. A 150 nm platinum coating with a 5 nm titanium sticking layer was deposited on the chip in a Temescal FC-2000 evaporation system [59]. This coating serves as the ground plane in the design

and as such is done at the backside of the chip.

After deposition of the ground plane, a resist bilayer is spun on the sapphire substrate. First a layer LOR-5B is spun [60]. Then immediately after a second resist layer is spun. The type of the second resist is AZ5214 [61]. The pattern for the first layer is written with a µMLA Heidelberg laserwriter [62]. The resist is then developed by submerging it in MF321 for 75s. Any undesired resist residuals are removed with an O_2 descum in a PVA Tepla 300 [63]. A first aluminum layer is then deposited on the entire chip in a Plassys FC-2000 evaporation system [64]. liftoff with a positive resist requires that the thickness of the deposited metal layer (t_{Al} = 30nm) is much thinner than of the bilayer resist ($t_{resist} \approx 1.4\mu m$). The remaining resisted is then stripped from the chip by submerging it in MF321 overnight. As a result, only the aluminum that was deposited directly onto the sapphire remains.

For the second aluminum layer, a LOR-5B and AZ5214 resist bilayer is spun again. During the exposure in the µMLA laserwriter, alignment of both layers with respect to one another, was done by using alignment markers that are present in the first layer. A development and O_2 descum step were done in the same manner as for the first layer. The process differs once the sample is loaded in the Plassys evaporator. Before deposition, the aluminum surface is in situ cleaned of native oxides with Ar^+ ion milling and subsequently a layer of aluminum oxides is grown under controlled circumstances. The details of the latter two processes are described in subsection 3.2.3 and 3.2.4. The second layer of aluminum is then deposited on the chip. This layer is 40 nm thick. liftoff is performed again by submerging the sample in MF321 overnight.

3.2.2. Choosing a Liftoff Resist

The patterns for the DJJAA are made by depositing an aluminum thin film on a sapphire substrate by the Plassys. As this deposition covers the entire substrate, it is necessary to remove deposited aluminum at places where it is unwanted. This is done using a liftoff process. Liftoff requires that a layer of photoresist that was patterned using lithography, is dissolved in a liquid resist stripper. As a result, only the aluminum that is deposited directly onto the substrate remains. aluminum deposited on the photoresist layer is left in the liquid. At the chosen spin speed the photoresist AZ5214 has a thickness of approximately 1.4 µm [61]. The deposited layer of aluminum is only 30 nm thick.

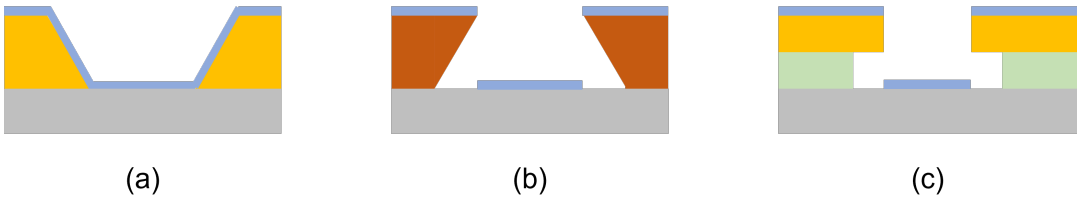

Figure 3.3: Inclincation of the side walls for positive (a), negative (b) and bilayer (c) resist. aluminum covers different areas with each type of resist. The colors correspond to: gray - sapphire substrate, light orange - AZ5214 (positive), dark orange - AR-N 4450.10 (negative), light green - LOR-5B (liftoff), blue - aluminum.

aluminum has a strong self-adhesive properties, which complicates liftoff. When using a positive resist (AZ5214) , the resist walls have a positive inclination, as shown in figure 3.3 (a). This caused aluminum to be also deposited on the sidewalls, forming a connection between aluminum on top of the photoresist and on the substrate. Due to these connections, aluminum will remain on the substrate at unwanted areas. In figure 3.4a, this effect is photographed using optical microscopy. On places where liftoff was successful, features show 'dog ears', which are signs of breakage near feature edges. This is aslo visible in figure 3.4a.

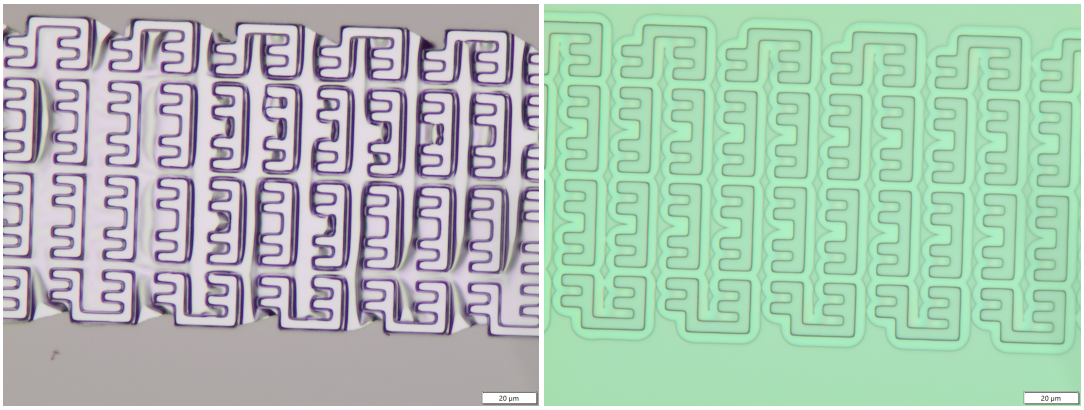

(a) (b)

Figure 3.4: Figure (a) shows deposited aluminum after liftoff. Between structures large aluminum flakes are still visible. Additionally, damages are visible around edges of structures ('dogears'). Figure (b) shows the double edge around structures that is visble when using a bilayer resist.

The solution is to use a resist which has a negative inclination or undercut at the sidewalls. This can be done in two ways: by using a negative resist (figure 3.3 (b)) or by using a resist bilayer (figure 3.3 (c)), containing a specific combination of two resist types. Both solutions were attempeted in this thesis project. However, the chosen negative resist (AR-N 4450.10 [65]) caused issues in fabrication and will not be considered further. The chosen resist bilayer consisted of a bottom layer LOR-5B and a top layer AZ5214. LOR-5B is a resist that is not sensitive to light exposure [60]. It does however develop in the chosen resist developer MF321. The development speed of LOR-5B can be tuned by varying the time and temperature of a bake after resist spinning. The development speed of LOR-5B was tuned to be much faster than that of AZ5214, in order to create an undercut. Figure 3.4b is taken after this resist bilayer was developed. A double line is visible near the edges of all features, indicating an undercut in the resist stack.

3.2.3. Calibration of Argon Milling

The insulating barrier in overlap junctions is formed by a thin oxide layer in between both Al evaporations. In order to target the correct normal state resistance and critical current for these junctions. Before this oxide barrier is grown, one has to remove any native oxides that are present on the substrate. Native oxides grow uncontrolled due to exposure to atmosphere in the cleanroom. For this reason, an argon mill is performed before oxidation. This step removes material using Ar^+ ions. It requires careful calibration. As explained in section 2.6.3 the etch rate of this process for aluminum is much higher than for aluminum oxides. Argon milling for too long introduces anisotropy in our thin films, which result in a lower junction quality. The process also affects deposited resist, making features wider and roughening their edges [55].

Calibration was done by argon milling on aluminum for different periods of time and then measuring the height. Argon milling was done in the load lock of the Plassys with 90 V acceleration for the Ar^+ ions. The height was measured using a white light interferometer (WLI, Bruker ContourX-500 [66]), which is an optical technique to measure surfaces. The precision of this type of height measurements was estimated to be around ±2nm for the given structures and sapphire substrate. Transferring the measured samples from the Plassys to the WLI exposed the sample to the cleanroom atmosphere. It is assumed that a native oxide barrier grows instantaneously once the sample is exposed to the cleanroom atmosphere. As a result, each argon milling step requires etching through a similar native oxide barrier before aluminum is etched away.

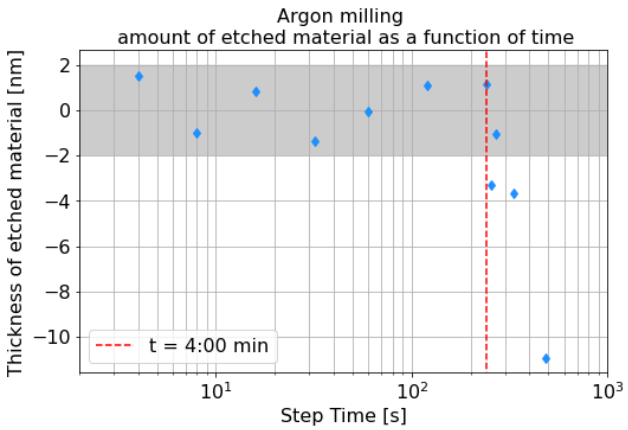

Figure 3.5: Decrease in aluminum thickness after argon milling for different times. The shaded gray area indicates the height imprecision of the WLI around 0 nm.

The calibration is shown in figure 3.5. Each data point indicates the amount of material that is milled away after argon milling for a specific amount of time. After $t = 4:00$ min, the amount of etched material increases sharply. This indicates that etching through the native oxide barrier requires around 4:00 min of etching. Hence the argon milling step in our junction recipe is chosen to last 4:00 minutes.

3.2.4. Oxidation of the Josephson Barrier

The previous section elaborated on removing native oxides from the Al thin films. Now we will focus on in situ regrowing an oxide barrier for our Josephson junctions. The barrier is grown by flowing O_2 at a given pressure in the vacuum chamber of the Plassys. There are three relevant parameters in this process: the oxidation time t_{ox}, the junction surface area A and the oxidation pressure p_{ox}. Section 2.6.4 demonstrated the relation between normal state resistance R_n and the critical current of Josephson junctions. This relation is used to calibrate the thickness of the oxide barrier of fabricated junctions. In literature, one can find an empirical relation between normal state resistance R_n and the parameters t_{ox} and A [21]

$$R_n \propto \sqrt{t_{\mathrm{ox}}}, A^{-1}. \tag{3.3}$$

For the oxidation pressure p_{ox} this relation could not be stated in such a straightforward form.

Calibration was done by depositing junctions while varying oxidation time and then measuring the normal state resistance at a probe station with a voltage source. During initial tests, the oxidation pressure was kept at a constant value of $p_{\mathrm{ox}} = 1.3$ mbar. This value was based on the experience of other users, who fabricate Josephson junctions using the same Plassys system. The normal state resistance from our junction design is $R_{\mathrm{ox}} = 37.5\Omega$ per SQUID. Figure 3.6 (a) shows the result of this calibration. The spread in measured resistance for constant oxidation time is attributed to underexposure of structures. This results in variations in junction area. The measured resistance per SQUID in this calibration was too low. We conjectured that due to the large junction size in our design ($A_{design} = 16$ µm), there was O_2-depletion near the junction surface at $p_{\mathrm{ox}} = 1.3$ mbar.

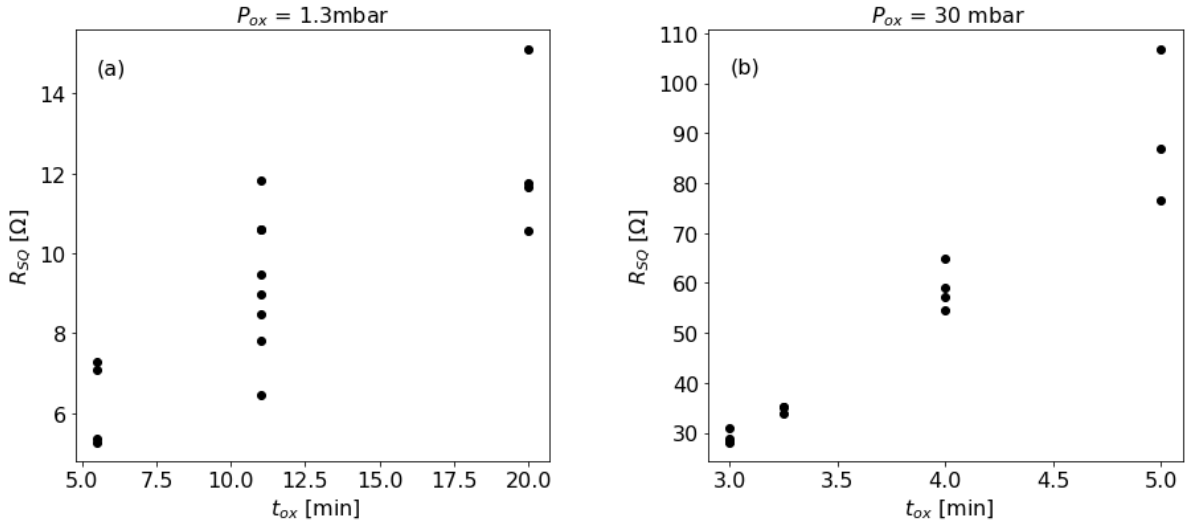

Figure 3.6: Calibration of the oxidation step in junction fabrication. normal state resistance R_n is shown as a function of oxidation time t_{ox} in figure (a) and of oxidation pressure p_{ox} in figure (b).

A similar calibration of oxidation time t_{ox} at higher oxidation pressure was necessary. It was chosen to do this at $p_{\mathrm{ox}} = 30$ mbar. The result of this calibration is shown in figure 3.6 (b). At this oxidation pressure, the measured normal state resistance R_{ox} is close to the target value after oxidizing for 3:15 min. When oxidizing for longer, the measured R_{ox} increased to approximately three times the target value within two minutes. At this oxidation pressure, small variations in oxidation time can lead to large variations in the resulting normal state resistance. This is an indication that a lower oxidation pressure is preferable. Unfortunately, it was not possible to calibrate this due to time constraints. Therefore it was chosen to perform oxidation of the Josephson barrier at $p_{\mathrm{ox}} = 30$ mbar for $t_{\mathrm{ox}} = 3{:}15$ min.

3.2.5. Fabrication Results

By combining the lessons that were learned throughout our iterations of the DJJAA fabrication process, we produced a final set of devices. Multiple DJJAAs were made on a 2-inch DSP sapphire wafer. The DJJAAs on this wafer were produced using the recipe from section 3.2.1. Once this was done, the wafer was diced in 4.2 x 8.1 mm die. Each die contains one single DJJAA.

Inspection of the fabricated devices was done in two ways: first a visual inspection was done to find potential defects using optical microscopy. Second a measurement of the normal state resistance was done to check the quality of the Josephson barrier in the junctions. During the latter, attention was paid that the normal state resistance of the top and bottom half of the array was as close as possible. Along the wafer there were large variations in the measured normal state resistance of DJJAA arrays. Normal state resistances in the range between $42.5k\Omega$ and2 $148.2k\Omega$ were measured on arrays consisting of 800 SQUIDs.

Due to time constraints it was not possible to measure and characterize 39 DJJAAs. Therefore, a single best device was chosen. Photos taken from this device using optical microscopy are shown in figure 3.7. The measured normal state resistance for the top and bottom half of the array are respectively $R_{\mathrm{top}} = 51.95k\Omega$ and $R_{\mathrm{bot}} = 57.89k\Omega$.

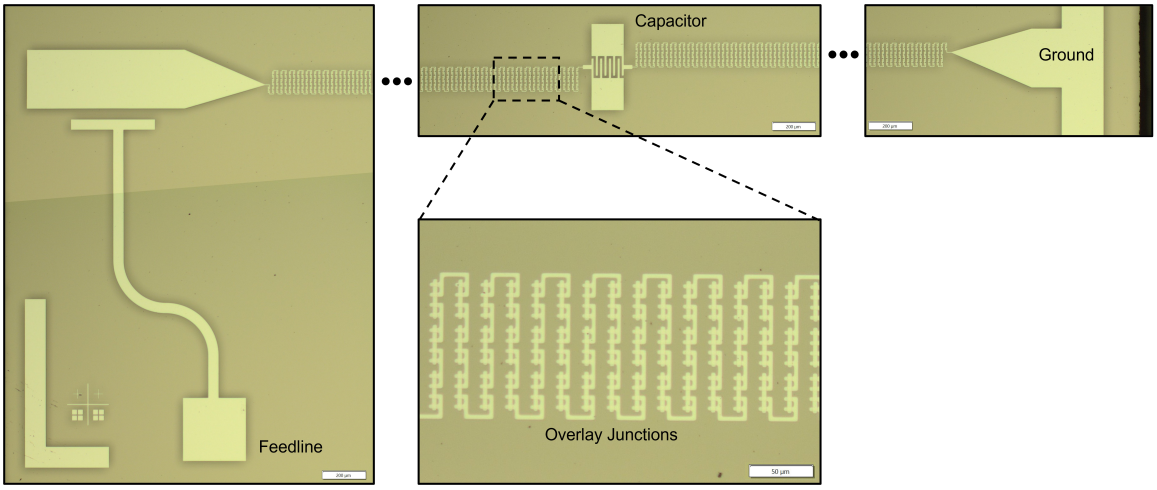

Figure 3.7: Optical microscopy of a fabricated DJJAA. The black dots indicate where parts of the junction arrays are left out. The different structures are labelled. The dashed lines indicate a zoom-in.

3.3. Assembly

In order to be able to operate the DJJAA as a parametric amplifier, it has to be packaged in a way that it fits in a cryogenic measurement setup. To do this it was mounted on a copper sample holder and connected to Printable Circuit Board (PCB). This sample holder was designed by Winkel et al. [18]. This section describes the procedure for mounting the DJJAA.

During the mounting procedure, the PCB is first screwed to the copper sample holder. Two SMA-antenna connectors are screwed on the sides of this sample holder. Both SMA-antennas are then soldered to the PCB. In the next step the DJJAA is glued directly onto the sample holder. As mentioned in section 3.2.1, the ground-plane of a DJJAA is on the backside of a chip. It is important that the connections between this ground plane and the sample holder are electrically-conductive. To that purpose, it was chosen to glue the DJJAA to the sample holder using EPO-TEK H20e [67], which is an electrically-conductive silver-epoxy. The DJJAA chip is then connected to the PCB using aluminium wirebonds. Figure 3.8 (a) shows a zoom in on the wirebonds on the DJJAA chip and figure 3.8 (b) shows the complete DJJAA in the sample holder.

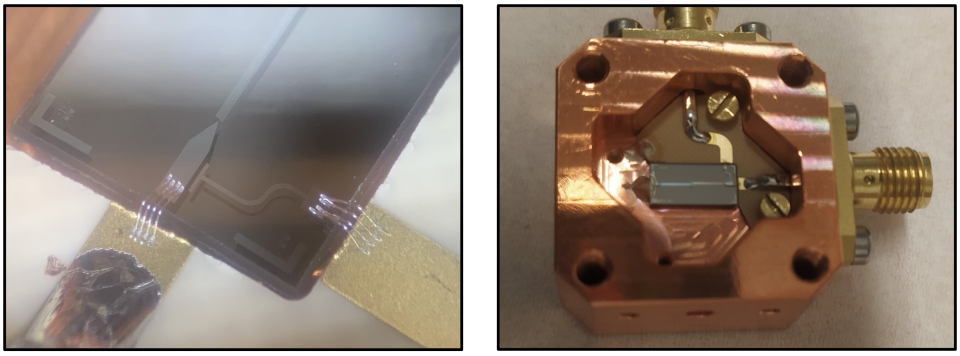

(a) (b)

Figure 3.8: Figure (a) shows the wirebonds on the DJJAA chip. The golden lines at the bottom of the image are the drive line and input line on the PCB. In figure (b) the DJJAA chip can be seen in the sample holder once it has been mounted.

Once the DJJAA is mounted, the lid can be screwed on the sample holder. This lid contains a coil that can be used to flux-tune the DJJAA. The closed sample holder is shown in figure 3.9 (a). The complete sample holder is then placed inside a magnetic shield to protect it from stray magnetic fields. Figure 3.9 (b) shows the magnetic shield.

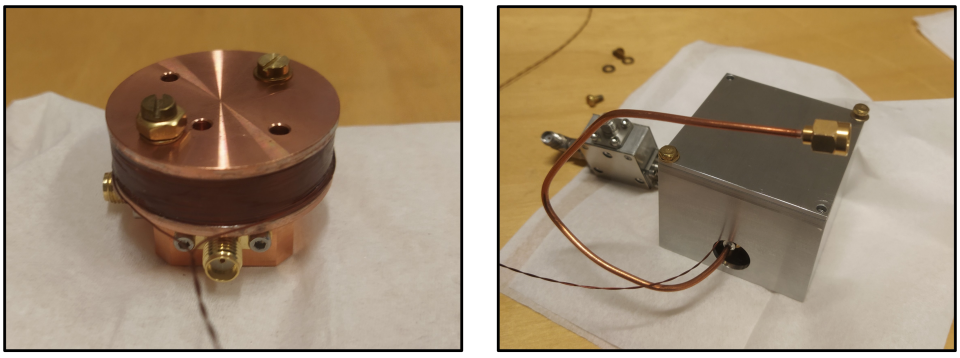

(a) (b)

Figure 3.9: Figure (a) shows closed sample holder. The round lid contains a coil to flux-tune the DJJAA. In figure (b) the sample holder has been placed inside a magnetic shield. The copper wire in front is connected to the drive line of the device.

3.4. Measurement Setup

To measure a superconducting device, requires a measurement setup below the critical temperature of the respective superconducting metal. Therefore, all measurements in this thesis were performed at the 300mK plate of a Entropy He7 cryostat [68]. This system has a base temperature of 4K and performs a measurement cycle in which the system cools to 300mK for a hold time of 4 to 8hrs. The total hold time depends on the applied heat load throughout a cycle.

Most measurement apparatus is operated at room temperature, whereas the device under test (DUT) is operated at cryogenic temperatures. Consequently, the cryostat has four AC lines, which connect the 300 mK plate to the environment outside the fridge. Three of these lines can be used to send in an input signal (line 2., 3. and 4.). The last line (1.) is used to retrieve the output signal. The input lines are connected to the output line through a microwave switch (Radiall R591763600).

The large temperature difference between the in- and outside of the fridge, is accompanied by large differences in thermal noise. To minimize the effect of these thermal noise differences on measurements, each line is equipped with multiple attenuators. These attenuators bring the thermal noise temperature at a stage, close to the temperature of the respective stage. All measurements discussed in this thesis were carried out at the 300 mK stage of the Entropy He7, unless indicated otherwise.

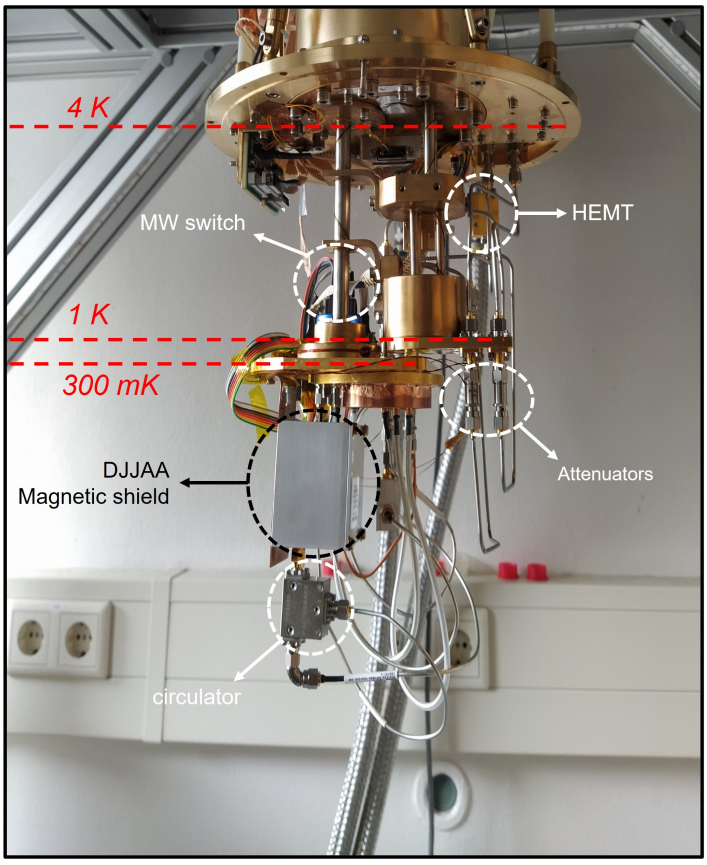

Figure 3.10: This figure shows the measurement setup that is schematically depicted in figure 3.11. The labels indicate where interesting parts of the measurement setup are located. Red dashed lines indicat the temperature of the different plates in the cryostat. These lines are indicated as well in figure 3.11.

The measurement setup is shown in figure 3.10. In figure 3.11 a schematic of the measurement setup is shown, that will be used as a guide to understand our measurements. The room temperature measurement equipment is a vector network analyzer (VNA, Keysight ENA E5080A). A signal is generated at the VNA and is then send into the fridge through input line 3. It is attenuated by 40 dB, before it reaches the 300 mK stage. At the 300 mK stage, a circulator (Pasternack PE2204-20) passes an input signal to the DJJAA (port 1 to 2) and re-

flects output signals from the DJJAA to the output lines (port 2 to 3). The signal is then sent to the output line through the microwave switch. At the output line, a circulator prevents any signal from being back-reflected into the DJJAA. The signal is then amplified by a HEMT ((Low Noise Factory LNF-LNC48C) and a room temperature amplifier (L3 Narda-MITEQ AFS3-04000800-07-10P-4) before it is returned to the second port of the VNA.

Line 4. of the VNA is used to supply an AC pump signal to the DJJAA. A directional coupler (Pasternack PE2204-10) is used to combine the signals coming from two AC power sources (Keysight MXG N5183B) in the fridge. Line 4. is also equipped with 40dB of attenuation before it reaches the 300 mK plate. The DJJAA can also be flux biased using a separate coil. This coil is connected to a DC current source (Stanford RS CS580) through the loom. The DC current then travels out of the fridge through a different line of the loom.

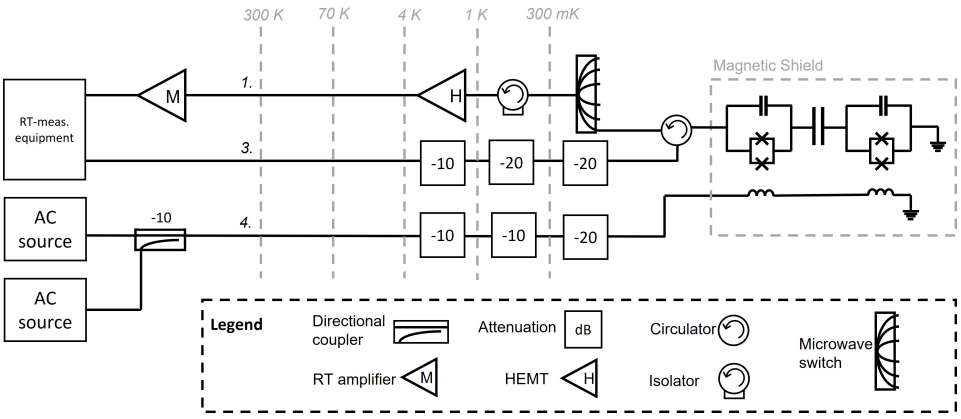

Figure 3.11: Schematic depiction of the measurement setup in the He7 Entropy for the measurements in this thesis. AC line 2. is not shown as it was not used during measurements. The circuit inside the grey box is an equivalent circuit to a DJJAA.

During this project, two types of Room-Temperature (RT) measurement equipment are used. The setup is changed depending on the type of measurement. The first setup is shown in figure 3.12 (a). Only the VNA is connected at RT. It is connected directly to the input and output line of the fridge. In the second RT-setup the output is connected to a spectrum analyzer (SA,Rohde & Schwarz FSV), as is shown in figure 3.12 (b). The signal to the VNA is now routed via a directional coupler, which attenuates it with -10 dB. The input line is still connected directly to the VNA.

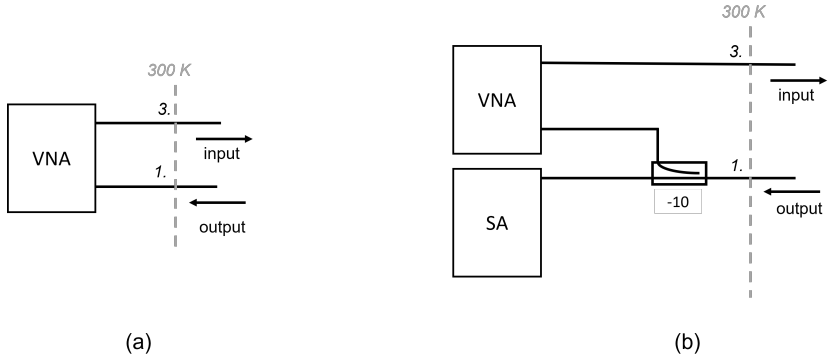

Figure 3.12: The measurement equipment at Room-Temperature (RT) that is connected to line 3. (input) and 1. (output) of the Entropy cryostat. Two setups are used: a setup where only the VNA is connected at RT (panel (a)) and a setup where the output of the fridge is connected to the spectrum analyzer (panel (b)). The VNA is connected to the output via a directional coupler.

3.5. Measurement Protocols

Once a DJJAA is mounted inside the measurement setup of the previous section, its performance can be characterized. This section introduces the measurement protocols that are necessary to do this. First subsection 3.5.1 introduces a protocol to find the resonant modes of the device. Then subsection 3.5.2 discusses two ways of using these resonant modes to amplify a signal. Lastly in subsection 3.5.3 different benchmarks are discussed that are used to quantify the performance of a DJJAA.

In section 3.4, the path that a microwave signal follows through our measurement setup was discussed. The signal start at port 1 and returns to port 2 of the VNA. We thus do a S_{21} measurement (using the S-parameter introduced in section 2.1). The input signal from the VNA has signal power P_{VNA}. The measurement is turned out in a bias magnetic field Φ_{DC}, which can be tuned by changing the bias current.

3.5.1. Flux-modulation of Dimer Modes

As a first step towards creating gain, we determined the resonance frequencies of the DJJAA modes. We operated the SQUIDs in the DJJAA as flux-tunable inductors by changing the DC flux bias. Due to the changing SQUID inductance, the resonance frequencies of the different modes shift. When no DC bias is present, DJJAA modes can still be tuned away from their design value due to stray magnetic fields. To account for this, we simply measure the frequencies of each mode for a range of DC flux biases. At each bias, we sweep a range of frequencies with a probe signal from the VNA. This measurement is called a DC flux-sweep. The result is that the dimer resonance frequencies follow an arc-shaped path for increasing flux-biases. Figure 3.13 shows an example measurement, where a dimer is flux-modulated. If the resonant modes are tuned towards the top of the arc, the device is said to be at its flux sweet spot. Ideally, the measured and design resonance frequency are the same.

An additional benefit of doing a flux-sweep, is that it also informs us about the frequency range on which we can tune each dimer. This is known as the tunable bandwidth of the dimer. This parameter is gives us direct information about the frequency range on which we can amplify signals.

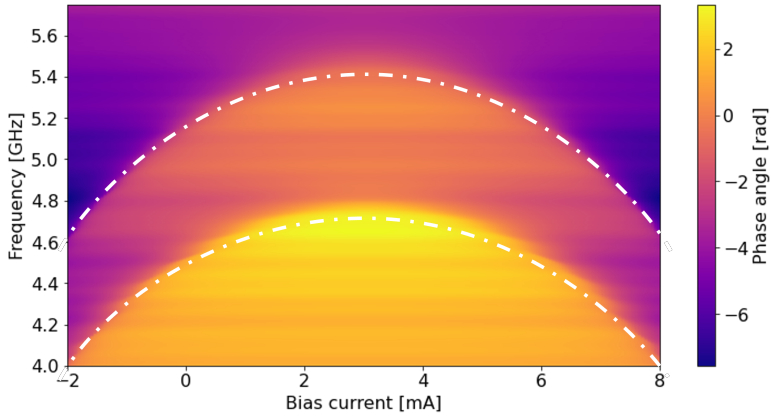

Figure 3.13: The phase response of two resonant modes in a dimer when changing the DC flux bias. The white lines indicate the path that the resonance frequencies of each dimer mode follow under changing flux biases.

3.5.2. RF Driving Schemes

To create signal gain, we drive the resonant modes of the DJJAA. We do this by placing an AC drive tone using an RF generator. This tone has two parameters that we can vary: It has an amplitude P_{drive} and a drive frequency f_{drive}. The frequency of the drive tone is chosen such that the three- or four-wave mixing condition from section 2.3.3 is fullfilled. Based on that two driving schemes were derived. The first scheme is shown in figure 3.14 (a). This is referred to as the dimer drive. It amplifies signals in both modes of a dimer at once. In this scheme an AC drive tone is applied at a frequency exactly between the two modes of the dimer by the RF generator.The dimer drive fullfills the four-wave mixing condition. The second scheme only amplifies a single resonant mode. It is called the bichromatic drive and is shown in figure 3.14 (b). The bichromatic

drive applies two AC drive tones, which are respectively red- and blue-detuned from the resonant mode by an equal amount. Signals in the resonant mode in between both drive tones are amplified. The applied detuning between both drives and the resonant mode is around 100 MHz.

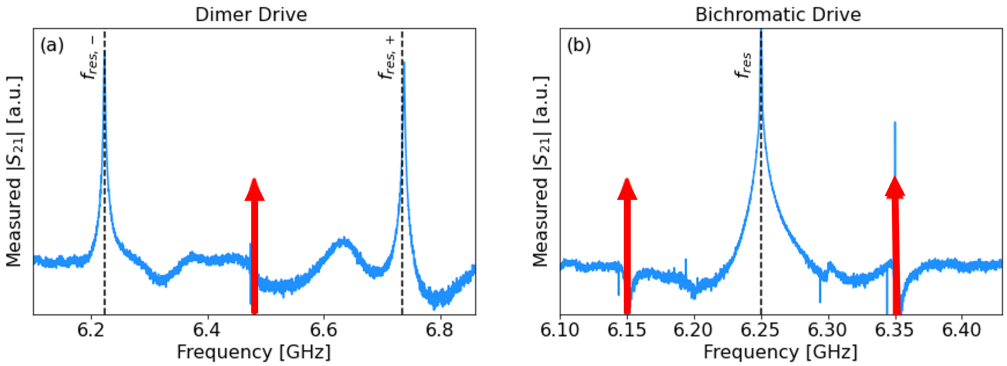

Figure 3.14: Frequencies of the AC flux pumps with respect to the resonant modes of the DJJAA when driving with the dimer drive (in panel (a)) and bichromatic drive (in panel (b)). Red arrows indicate the frequencies of the separate drive tones.

3.5.3. Device Characterization

The performance of an amplifier can be judged on four areas: gain performance, operational bandwidth, saturation power, and noise performance [69]. In order to make a meaningful comparison with other amplifiers, benchmarks can be defined to assess each of these areas. This section introduces the benchmarks that were used during the measurements in this thesis. The complications in measuring each benchmark are also discussed. In the results chapter of this thesis, these benchmarks are used throughout measurements on two DJJAAs.

Maximum Gain

The first benchmark that we discuss is gain performance. This is measured using the maximum achievable gain G_{max}. The maximum gain is defined as the maximum increase in signal amplitude at a frequency when an AC drive tone is applied to the amplifier. This thus requires to measure the background in the absence of an AC drive tone as well.

A complication arises due to measurement setup: due to imperfections in input and output lines, signals at some frequencies are transmitted better than others. This result in a background that is not flat when no signal is present. A solution to this problem can be to do an Short-Open-Load (SOL) calibration. Such a calibration was not done during this project, but is carried out in [26]. A different approach was taken here. In order to report an indication of G_{max}, measurements of the driven DJJAA are complemented with separate measurements of the background when no drive was present. The difference between both measurements could be used to estimate G_{max} from the increase in the measured $|S_{21}|$ parameter when driving. This is referred to as background subtraction.

Operational Bandwidth

The operational bandwidth of a JPA is the range of frequencies at which the signal is amplified sufficiently to be used in experiments. In JPA literature this is often defined as the frequencies with more than 20 dB of attenuation [15, 20, 26, 69]. We thus define the 20dB-bandwidth BW_{20} as the largest continuous range of frequencies on which a JPA amplifies more than 20dB. When the DJJAA is operated using a the dimer drive, BW_{20} is thus measured on a single resonant mode. In the definition of BW_{20}, a similar problem arise as with maximum gain: due to the use of uncalibrated gain, it is not exactly clear on which range the device achieves 20dB of amplification. This problem was resolved as well by using background subtraction.

Saturation power

Section 2.4.2 discussed the mechanisms that are responsible for amplifier saturation in JPAs. The practical result is that for too large signal power, the maximal achievable gain decreases. During amplifier operation it is relevant to know what is the maximum signal power before gain starts to decrease. To this purpose we

define the 1dB-compression point $P_{1\text{dB}}$. As its name suggests, this is the input power at which the signal gain decreases by 1dB compared to the maximum achievable signal gain for low power input signals.

We can measure $P_{1\text{dB}}$ by selecting an operating point for the DC flux bias Φ_{DC} and AC flux pumps Φ_{AC}. We then start to increase the VNA probe power P_{in} and sweep the frequency. From each frequency sweep we extract the maximum achieved gain and analyze this as a function of VNA probe power. From the resulting plot we can then straightforwardly read out $P_{1\text{dB}}$. The result of this measurement on a DJJAA is presented in 4.1.5.

Noise Performance

A straightforward approach to quantify noise performance of an amplifier is by monitoring the noise output spectrum of the device while the drive tone is respectively turned on and off. The noise added by the amplifier is inferred by subtracting the noise at each frequency while the drive tone is turned off from the data from when it is turned on. Due to time constraints this measurement could unfortunately not be carried out during this thesis project.

To monitor the output noise at a given frequency, the power spectral density (PSD) is measured using a spectrum analyzer. The PSD $S_{xx}$of a signal $x(t)$ at frequency ω is calculated as [19]

$$S_{xx}(\omega) \equiv \int_{-\infty}^{+\infty} \langle x(t)x(0)\rangle \, e^{j\omega t} dt. \tag{3.4}$$

The power spectral density can intuitively be understood as the power emitted by a signal at a given frequency. The power integrated over the entire frequency spectrum yields the variance of the signal. PSD measurements were used to indicate the presence of self-oscillations in section 4.2.3.

4

Results & Discussion

The discussions in the preceding chapter presented the necessary theory and experimental methods that are necessary to understand the results of this thesis. This the point were we can discuss these results. We will demonstrate the performance of a DJJAA as an amplifier, discuss self-oscillations in the device and discuss the performance of DJJAAs fabricated in Delft.

Two DJJAAs were measured in the measurement setup from section 3.4. One DJJAA was send over from Karlsruhe Institute of Technology (KIT). This device is dubbed the KIT-DJJAA. The second DJJAA was produced in the Kavli Nanolab at TU Delft according to the recipe from section 3.2.1. This device was presented in section 3.2.5 and is dubbed the TUD-DJJAA.

This chapter is divided in three parts. The first parts focusses on operating the KIT-DJJAA as was intended in its design: by operating both modes in a dimer at once. We discuss our means of finding the resonance frequency of both dimer modes. We then focus on driving those modes and discuss the optimal driving frequency of a dimer. This part concludes with a discussion on calibrating the attenuation of the input line and the saturation power of the DJJAA.

In the second part, the bichromatic drive is used to measure the effect of changing drive power on signal amplification in the KIT-DJJAA. Measurements obtained on low-drive power are used to understand the workings of the bichromatic drive. Then the drive power is increased enough to induce nonlinear effects, which are presented as well. We demonstrate that these effects are likely self-oscillations of the mode.

The last part of this chapter presents measurements on the TUD-DJJAA. The measurements on this device serve two goals. Firstly, they aim on determining if the fabricated device works and can be used to amplify signals. Secondly, this section assesses if any lessons can be learned on our DJJAA fabrication process.

4.1. Dimer operation of the KIT-DJJAA

The first thing that is investigated in the KIT-DJJAA, is its operation as a nondegenerate amplifier. The aim of this investigation is to infer the maximum gain and VNA saturation power of the DJJAA. We will consider the resonant modes of this device as Kerr-oscillators, which were discussed in section 2.4.1. This is done by analyzing the shifts of the mode resonance frequencies if the drive power and VNA probe power are varied. The frequency shifts are used to calibrate the strength of the drive power at the input of the DJJAA, which is done in section 4.1.4.

The measurement setup used in this section is presented in section 3.4. The KIT-DJJAA was loaded in the measurement setup. At room temperature the output line of the setup was directly connected to a port of the VNA, as illustrated in figure 3.12 (a). The probe signal that the VNA sends has power $P_{\mathrm{VNA}} = -60$ dBm, unless indicated otherwise.

In next section we present flux-modulation measurements to infer the mode resonance frequencies. The effect of applying the dimer drive and the resulting shifts of the mode resonance frequency are discussed in section 4.1.2. In section 4.1.3 we then discuss how the parameters of this dimer drive can be optimized. Section 4.1.4 presents a calibration of the drive power at the input of the DJJAA, which is used to determine the saturation power of the device in section 4.1.5.

4.1.1. Flux-Modulation of Dimer Modes

In order to find the resonant modes in the DJJAA, we performed a sweep of the DC flux as described in section 3.5.1. DC flux was varied by changing a bias current going into the device between −8.0 mA to 12.0 mA. We measured the S_{21} parameter at the VNA in the frequency range 3.5 GHz to 8.5 GHz. This frequency range was limited by the frequencies at which the HEMT operates.

The measured S_{21} amplitude is shown in figure 4.1 (a). In this figure four arcs are visible, which correspond to four resonant modes of the DJJAA. These four modes can be grouped in two dimers. Together, these two dimers can be flux-modulated such that they cover the complete 4-8 GHz frequency range. The modes are labelled according to their resonance frequency. At $|\Phi_{\mathrm{DC}}/\Phi_0| > 0.32$ two additional dips are measured. These correspond to two different modes, which form a third dimer. To distinguish between the different dimers, an index $i = 1,2,3$ is assigned to each dimer. The symbol $f_{i,+/-}$ is used to refer to the resonance modes of a dimer pair. The subscripts $+,-$ are used to refer to the higher and lower frequency mode in a dimer pair.

figure 4.1 (b) shows a linecut from figure 4.1 (a) at $I_{\mathrm{DC}} = 0$ mA. Various dips in S_{21} amplitude are visible when passing along the frequency axis. In figure 4.1 (a) these dips are visible as well as horizontal ripples. This phenomenon is thus unaffected by a change in DC flux bias. A likely origin for this effect are impedance mismatches at the interface between different components in the measurement setup. Due to impedance mismatches between cables in the input and output lines, standing waves can from in the cables of these lines. Consequently the transmission of different signal frequencies becomes dependent on the frequency of these standing waves and indirectly on the length of the line, as explained in section 2.1.3. This can result in ripples in the S_{21} amplitude of the measurement setup. More thorough calibration of the measurement setup is a means of mitigating this effect.

We saw that it is challenging to determine the resonance frequencies of the different modes from the amplitude in figure 4.1 (b). Therefore, also the complex phase of the same linecut is plotted in figure 4.1 (c). Around $f_{1,-} = 4.54$ GHz and $f_{1,+} = 5.15$ GHz, the slope of the complex phase is steeper compared to the background. This increase is a strong indication that these frequencies are the resonant frequencies of two resonant modes.

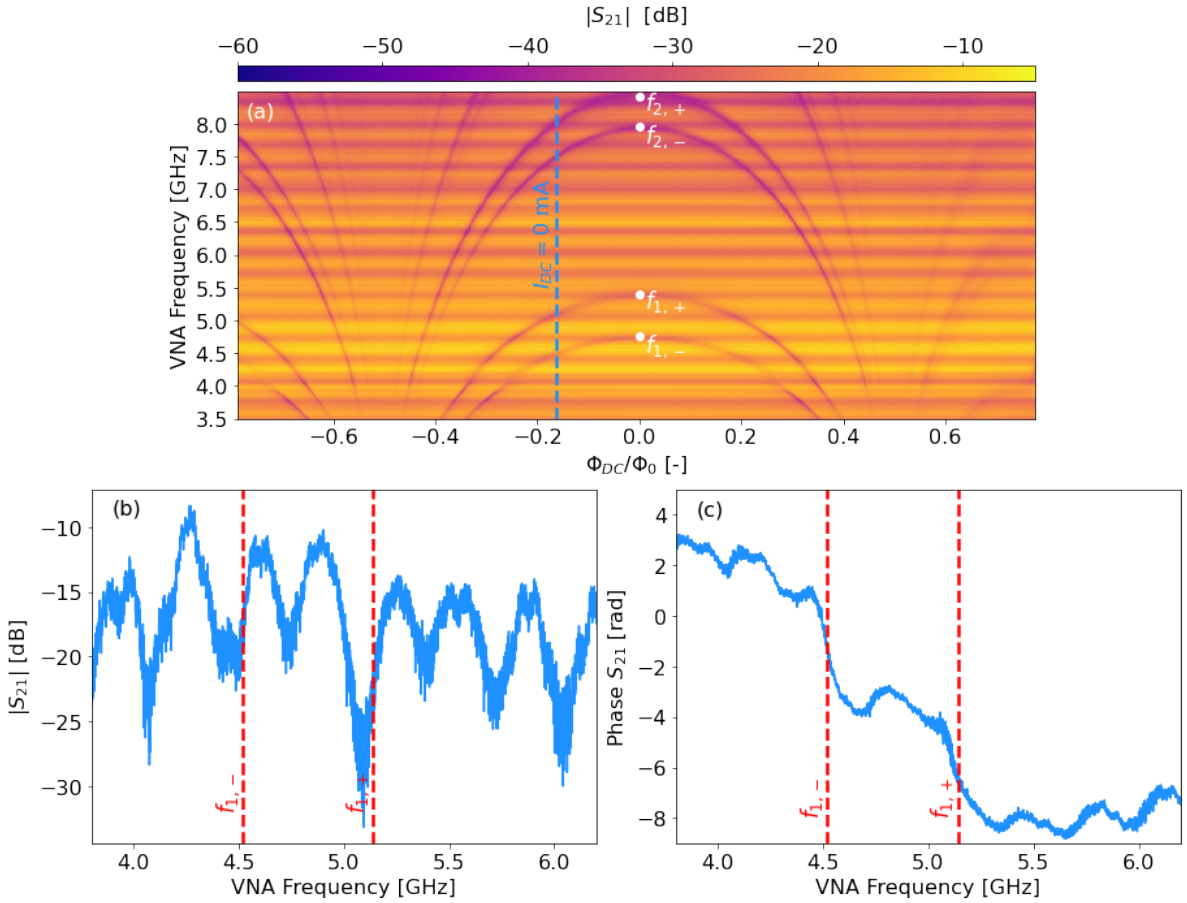

Figure 4.1: Flux-modulation of the resonant modes in the KIT-DJJAA in the 4-8 GHz range. Panel (a) shows a sweep of the DC bias flux of the DJJAA for a range of VNA probe frequencies. The blue line indicates the DC flux operating point in the remainder of the measurements on the KIT-DJJAA. The frequency of the resonant modes is labelled at the flux sweet spot. The S_{21} amplitude (b) and phase (c) are shown for the linecut at $I_{\mathrm{DC}} = 0$ mA. The mode frequencies $f_{1,-}$ and $f_{1,+}$ are indicated by a red dashed line in both plots. The mode frequencies are occulted in the amplitude measurement (in panel (b)), but are clearly distinguished by a steepening of the complex phase (in panel (c)).

Now that we are able to locate the resonant modes of the DJJAA for a given flux bias Φ_{DC}, we can determine their resonance frequency at the flux sweet spot $\Phi_{\mathrm{DC}} = 0$. This result is listed in table 4.1, together with the design values that were simulated in 3.1. From table 4.1 we learn that the resonance frequencies at the sweet spot are all lower than expected from simulations.

Table 4.1: Comparison of measured resonance frequencies of the DJJAA modes in the KIT-DJJAA to the design resonance frequencies

Mode index	$f_{1,-}$	$f_{1,+}$	$f_{2,-}$	$f_{2,+}$
Design	4.565 GHz	5.061 GHz	7.644 GHz	8.129 GHz
Measured	4.760 GHz	5.400 GHz	7.920 GHz	8.420 GHz

To conclude this part of our discussion, we choose an Φ_{DC} operating point for the KIT-DJJAA for further characterization of the device. This operating point was chosen at $I_{\mathrm{bias}} = 0$ mA, which corresponds to $\Phi_{\mathrm{DC}} = -0.3\Phi_0$. At this DC flux operating point and in the absence of an RF pump tone, the dimer resonance frequencies are $f_{1,-} = 4.54$ GHz, $f_{1,+} = 5.15$ GHz, $f_{2,-} = 7.49$ GHz, $f_{2,+} = 8.08$ GHz. The motivation behind this reasoning is practical: operating the device at $I_{\mathrm{DC}} = 0$ mA does not strictly require a current source. However, it should be noted that a different operating point potentially has a better performance in terms of signal gain.

4.1.2. Amplification of Both Dimer Modes

As a next step, we can apply an AC drive tone to amplify a signal in the resonant modes. We aim to create gain in both modes of a dimer by applying a drive tone in between these two modes, as was explained in section 3.5.2. This section presents the spectra that we measured by driving the two resonant modes in a dimer by using this dimer drive. We observe that the drive tone induces a shift of the resonance frequency of the dimer modes. Also, it is demonstrated how the phase of the modes can be used to determine if an applied AC drive tone couples to a resonant mode.

On dimer 1 and 2 we performed the same measurement: we place the drive tone at a frequency f_{drive} and then increase the drive strength P_{drive} stepwise. The frequency f_{drive} was chosen to be exactly half way between the separate dimer modes. After each increment, the VNA sweeps a range of frequencies with a probe signal. We will discuss the results on dimer 2 here. This was done because this dimer can be flux-modulated to have a resonance frequency in the 6-8 GHz range. The same measurements on dimer 1 are presented in appendix B.1.

For the measurement on dimer 2, the drive tone was placed at $f_{\text{drive}} = 7.459$ GHz. In figure 4.2 (a) we can see a sweep of the frequency at $P_{\text{drive}} = 3.80$ dBm. Both dimer modes are visible around $f_{2,-} = 7.178$ GHz and $f_{2,+} = 7.744$ GHz. The maximum gain measured in this sweep is $G_{\text{max}} = 43.6$ dB in dimer $f_{2,-}$. This value was inferred by background subtraction, as was explained in section 3.5.3. The gain in this spectrum is nondegenerate, as was indicated in section 3.5.2.

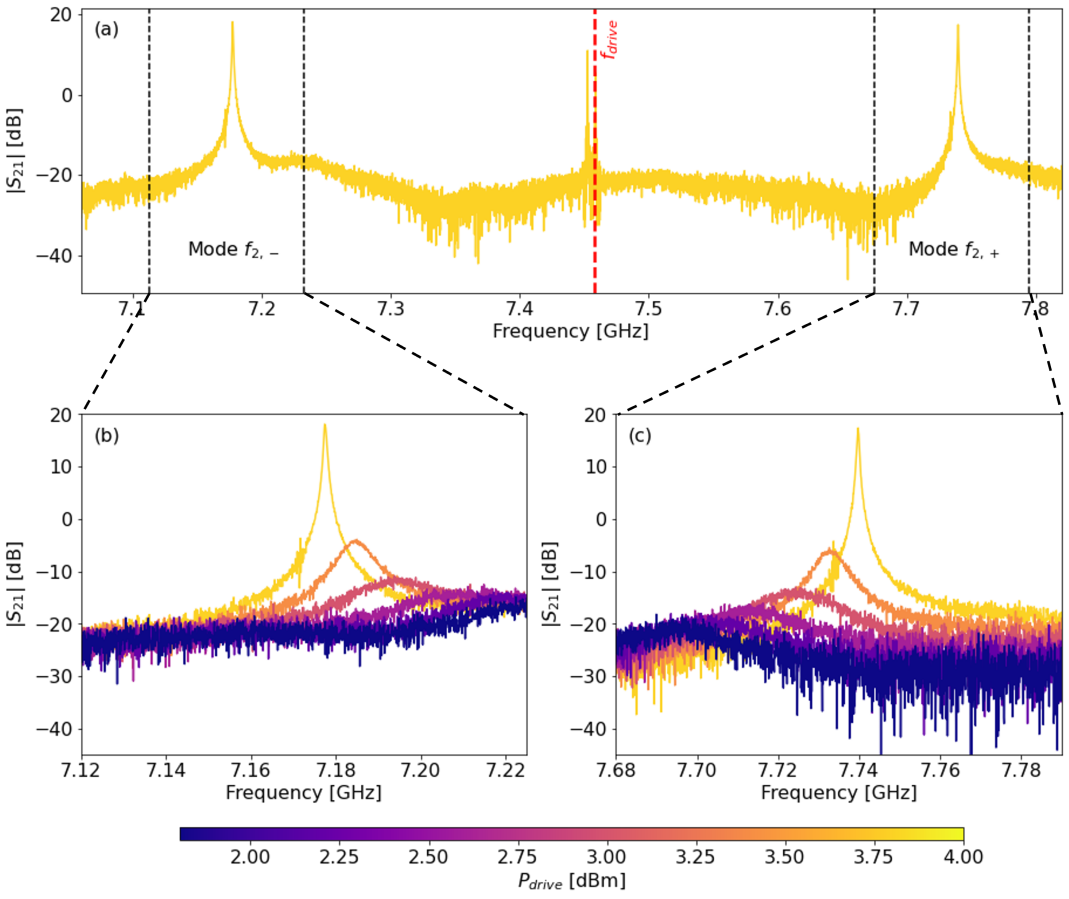

Figure 4.2: $|S_{21}|$-parameter of drive power measurements of dimer 2. The dimer is driven with the dimer drive. When the drive power is increased, an increasingly high and narrow peak emerges at the resonance frequency. The resonance frequency of both peaks is observed to shift further from the drive frequency with increasing drive power (in panel (b) and (c)). Panel (a) shows the frequency spectrum of the whole dimer at drive strength $P_{\text{drive}} = 3.80$ dBm. The drive frequency is indicate by a red dashed line. Dimer modes are at $f_{2,-} = 7.178$ GHz and $f_{2,+} = 7.744$ GHz. Panel (b) and (c) show the effect of increasing drive power on the amplification in both modes.

In figure 4.2 (a), detuning between the drive tone and both modes is approximately 286 MHz at $P_{\text{drive}} = 3.80$ dBm. However, when looking at figure 4.3 (b) and (c), it becomes apparent that the resonance frequency of both modes changes with drive power. The frequencies $f_{2,-}$ and $f_{2,+}$ are pushed away from the drive frequency f_{drive} when the drive power increases.

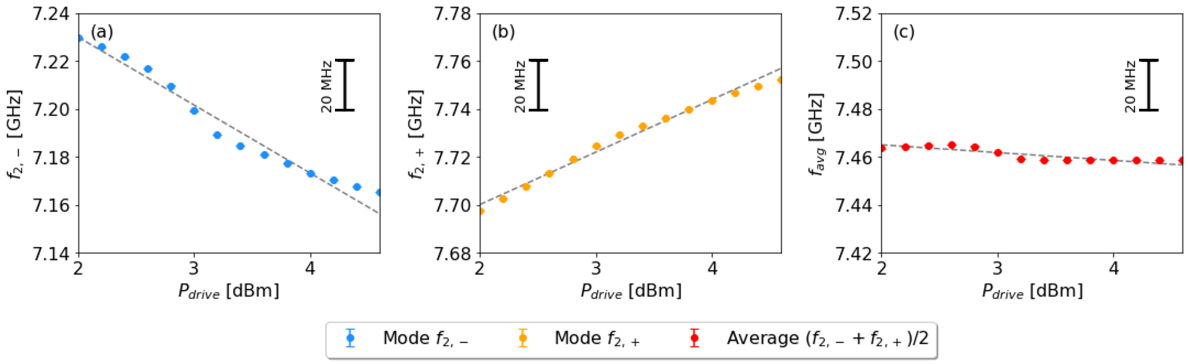

Figure 4.3: Fitted resonance frequencies from the data in figure 4.2. The fitted resonance frequency of the individual modes $f_{2,-}$ (in panel (a)) and $f_{2,+}$ (in panel (b)) shifts in opposite direction with increasing drive power. Panel (c) shows that average of both frequencies has a negative slope, which is much flatter than the slope of the individual modes. This negative frequency shift is induced by the Kerr-nonlinearity.

To better understand the shifts of both dimer modes as a function of drive power, we extracted the resonance frequency at each drive power. This was done using Lorentzian fits. Our fitting protocol is discussed in appendix A.1. The extracted resonance frequencies for mode $f_{2,-}$ and $f_{2,+}$ are plotted in figure 4.3 (a) and (b) respectively. Figure 4.3 (c) displays the average of the frequency of both dimer modes. The average frequency decreases with drive power. This decrease can be explained by considering the individual modes as Kerr-oscillators, as was done in section 2.4. This treatment predicts a downward frequency shift Δf of the resonant modes if their mode population increases. This would result in a downward shift of average of the resonance frequencies of both modes, which was observed in figure 4.3 (c).

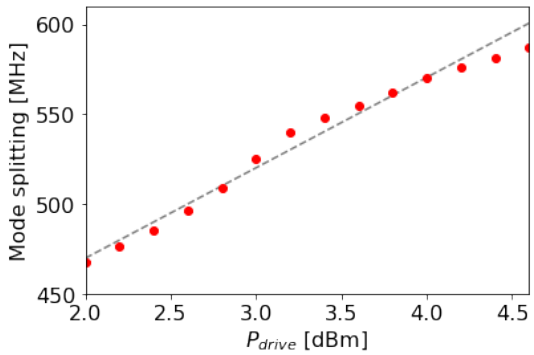

Figure 4.4: Observation of power-dependence of splitting between two dimer modes. The frequency splitting between the resonant modes in figure 4.2 increases with drive power P_{drive} of the dimer drive. The grey dashed line is a fit of the splitting as a function of drive power. The mode splitting was calculated by subtracting the fitted mode frequencies from mode $f_{2,+}$ and $f_{2,-}$ from each other.

However, this decrease has a much smaller slope than the respective shifts of the individual modes. The slopes of the individual dimer modes is opposite, as can be seen in figure 4.3 (b) and (c). This is in line with the observation that mode splitting increases with drive power. By subtracting the resonance frequencies from each other, the exact mode splitting is calculated, as is done in figure 4.4. Here, we can see that mode splitting indeed increases linearly with drive power. The Kerr-oscillator treatment does not predict this increase of the mode splitting as a function of drive power. A possible origin of this effect can be the coupling between two dimer modes. Section 2.5.2 discusses how two modes in a DJJAA can be considered as two coupled harmonic oscillators. In such a system mode splitting increases with drive power, which would explain the observed increase of the mode splitting at higher drive power.

In conclusion, we found that it was possible to parametrically drive both modes in a dimer with the dimer drive. We estimated that the maximum obtained gain $G_{\max} = 43.6$ dB. We observed that the frequency of both dimer modes shifts if the drive power was increased. This is likely a Kerr-induced frequency shift, dependent on the photon population of each mode. Additionally, the mode splitting between the two dimer modes was found to increase with drive power.

Phase Response of Dimer Modes While Driving

The last part of this section focuses on a more practical aspect of driving resonant modes. Section 4.1.1 discussed how the complex phase could be used to identify the resonance frequency of the DJJAA modes. It was observed that the mode frequencies of a dimer shift when the dimer drive is applied. Here we demonstrate that the complex phase is useful for adjusting the drive frequency of the dimer drive to compensate for those frequency shifts.

Figure 4.5 shows the phase corresponding to the data from figure 4.2 (b). This data was taken on mode $f_{2,-}$. At the resonance frequency of the mode a drop in the phase can be observed at each drive power. With each increment of the drive power, this phase drop becomes steeper. In the inset of figure 4.5 it can be observed that the peak value of the S_{21} amplitude also increases with each increment. At the maximum drive power $P_{\text{drive}} = 4.00$ dBm, the phase drop happens instantaneous at the resonance frequency $f_{1,-} = 7.178$ GHz. Additionally, the frequency of the phase drop shifts towards lower frequencies with increasing drive power. This is the same frequency shift that was observed in the amplitude of the S_{21} parameter. If the signal in a mode is only slightly amplified, as is the case at $P_{\text{drive}} = 2.00$ dBm in figure 4.2 (b) and 4.5, no peak is visible in the amplitude of the mode. However, the mode frequency can be inferred from the phase drop at this drive power. In practice, this allowed us to use the phase of the modes as a means to adjust the drive frequency f_{drive}.

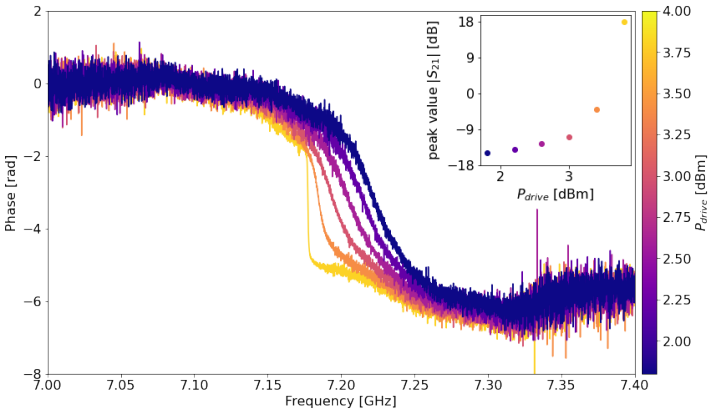

Figure 4.5: The complex phase of the resonant modes becomes steeper if the gain in a mode increases. The main figure shows the complex phase of mode $f_{2,-}$ during the measurements in figure 4.2. Subsequent traces are taken with an increased drive strength P_{drive}. The inset shows the peak value of the S_{21} amplitude in each trace. The steepening of the phase drop around the resonance frequency $f_{2,-}$ can be used to adjust the drive frequency of the parametric drive.

This section measured the $|S_{21}|$ parameter in a dimer while the dimer drive was applied. It was found that the splitting between both dimer modes increases with drive power. The average frequency of both modes decreases with drive power. This frequency shift is induced by the Kerr-effect when mode population increases. In order to obtain maximum amplification of signals the drive frequency can be adjusted for these shifts by observing the phase drop of the driven resonant modes.

4.1.3. Optimal Point of Operation of the Dimer Drive

In section 4.1.2 we showed that we can create amplification of an input signal in both dimers in the KIT-DJJAA and an estimate of the maximum achieved gain was made. As a next step we investigate if we can achieve more signal amplification by optimizing the drive parameters and discuss the effect of varying these parameters.

For this purpose, again a drive tone is placed in between the two modes of dimer 2. Both the power P_{drive} and frequency f_{drive} of this drive are varied. For each combination of P_{drive} and f_{drive}, the maximum value of the S_{21} parameter is extracted. The drive power P_{drive} is varied from 0 to 5 dBm and the drive frequency is varied between 7.38 GHz and 7.50 GHz. the VNA sends a probe signal along the range 7.0 GHz to 7.9 GHz. From each frequency sweep of the VNA, the maximum signal amplitude is extracted as the gain, while excluding a 5 MHz range around the drive frequency.

The resulting measurement is displayed in figure 4.6. The maximum $|S_{21}|$ parameter can be used to estimate the maximum gain. This maximum gain was estimated to be $G_{\text{max}} = 53.4$ dB for the combination $f_{\text{drive}} = 7.459$ GHz and $P_{\text{drive}} = 4.0$ dBm. This was done using background subtraction as explained in section 3.5.3.

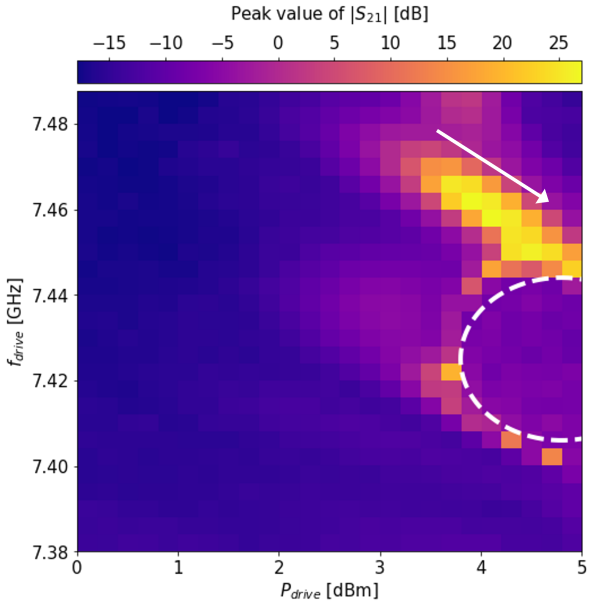

Figure 4.6: At higher drive power P_{drive} the drive frequency f_{drive} has to be adjusted to a lower frequency for maximum signal amplification. The figure shows the peak value of the S_{21} amplitude as a function of drive parameters f_{drive} and P_{drive}. This value is inferred from a VNA measurement in the frequency range 7.0 GHz to 7.9 GHz for each combination of drive parameters. Around $f_{\text{drive}} = 7.475$ GHz a region of large amplification is visible. The shift of the optimal drive frequency with increasing drive power is indicated with a white arrow. The white circle indicates a region where the maximum $|S_{21}|$ parameter sharply decreases.

In figure 4.6 a white arrow indicates an area where the signal is strongly amplified. In this area the measured peak value in the $|S_{21}|$ parameter exceeds 20 dB. The onset of this area is observed around drive power $P_{\text{drive}} = 3.8$ dBm, with corresponding drive frequency $f_{\text{drive}} = 7.475$ GHz. An interesting feature of this area is, that the drive frequency of maximum gain, shifts towards lower frequencies with increasing drive power. It is plausible that this shift is due to a mode population-dependent Kerr-shift, that was discussed in section 2.5. When the drive power increases, the number of photons in both dimer modes increases as well. As a consequence, the resonance frequency decreases proportionally to the increase in photon population n_{mode} of the mode: $\Delta f \propto K/\kappa n_{\text{mode}}$, where K is the self-Kerr coefficient and κ the decay rate of the mode. This Kerr-shift was observed in section 4.1.2. From figure 4.6 it now follows that the drive frequency can be adjusted to compensate for this shift. This way, large signal amplification can still be obtained with a strong RF drive.

At the top of figure 4.6, a white circle marks an area where the maximum gain is much lower than outside the circle. Inside the circle, the maximum returned gain is decreased and fluctuates more than outside of the

circle. At $f_{\text{drive}} = 7.42$ GHz, the edge of the circle is at drive power $P_{\text{drive}} \approx 3.7$ dBm. Figure 4.7 shows a VNA measurement just inside and outside this region at drive frequency $f_{\text{drive}} = 7.42$ GHz. The S_{21} amplitude is plotted on a linear scale. At $P_{\text{drive}} = 3.60$ dBm, two Lorentzian peaks are visible around $f_{2,-} = 7.143$ GHz and $f_{2,+} = 7.699$ GHz. These peaks indicate that an incoming signal is amplified in the DJJAA. At the higher drive strength ($P_{\text{drive}} = 3.80$ dBm), the measured frequency spectrum becomes chaotic: the Lorentzian peaks have disappeared and the fluctuations in the background have increased. This chaotic behaviour was found to be unpredictable. As such it is not suitable for reliable amplification of signals.

To understand what this regime is, further measurements are necessary. A possible explanation is that the device becomes self-oscillating. This phenomenon was discussed in section 2.4.3. A similar effect as what we observed here, occurs at high drive strength when using a bichromatic drive on a single DJJAA mode. This is investigated in section 4.2.

In summary, we observed that the optimum drive frequency f_{drive} of the dimer drive decreases when the drive power P_{drive} is increased. If the drive power is increased above a threshold power, the measured signal gain suddenly decreases and the output spectrum becomes chaotic. This is likely the result of self-oscillations.

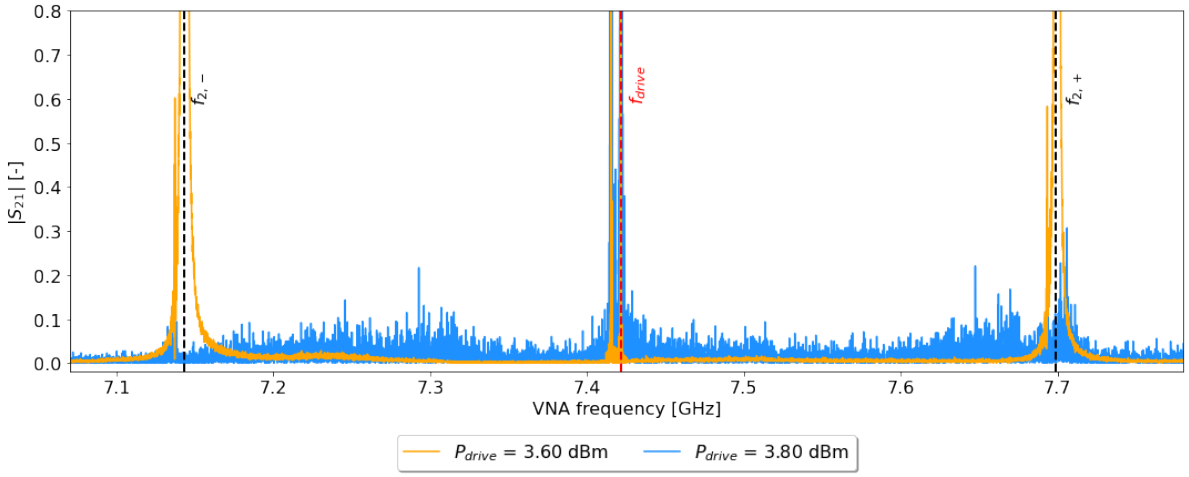

Figure 4.7: The signal amplification disappears and background fluctuations increase if the drive power increases beyond a undefined threshold. The plot shows two trace from the VNA, which were used to estimate the peak S_{21} amplitude in figure 4.6. Both traces were taken with $f_{\text{drive}} = 7.42$ GHz. The trace with $P_{\text{drive}} = 3.60$ dBm is outside the white circle in figure 4.6, the trace with $P_{\text{drive}} = 3.80$ dBm is just inside the white circle.

4.1.4. Measuring the Kerr Shift of a Resonant Mode for Absolute Power Calibration

Before we can characterize the saturation power of a DJJAA, it is necessary to know the signal power at the input of the device. We exploit the Kerr-induced frequency shift that was discussed in the preceding sections to infer this. The frequency shift can be used to calibrate the number of photons resonating in a mode, which in turn can be used to calibrate the drive power at the input of the DJJAA. This is called the cold drive power P_{cold}.

In order calibrate the cold drive power P_{cold}, we first need to know the resonance frequency for a given drive power. Therefore, we place a weak drive tone at a frequency several linewidths above the mode $f_{2,-}$. Then the power of this drive tone is increased stepwise. After each increment a VNA probe sweeps the frequency range from 7.0 GHz to 7.6 GHz. From the complex phase of each VNA trace, we can extract the resonance frequency of the mode $f_{2,-}$ at each specific drive power.

The complex phase of this measurement is presented in figure 4.8 (a). A white arrow marks the resonance frequency $f_{2,-}$. This frequency decreases when the drive power increases. Around $P_{\text{drive}} = -3.00$ dBm, the phase drop becomes narrower. In section 4.1.2, we saw how such a narrowing of the phase drop can indicate that the mode amplifies the VNA signal. It was discussed in section 4.1.2 that once a mode is amplified, the Kerr-shift is not the only effect that changes the resonance frequency of the modes. Therefore, we limit our analysis to $P_{\text{drive}} < -3.00$ dBm

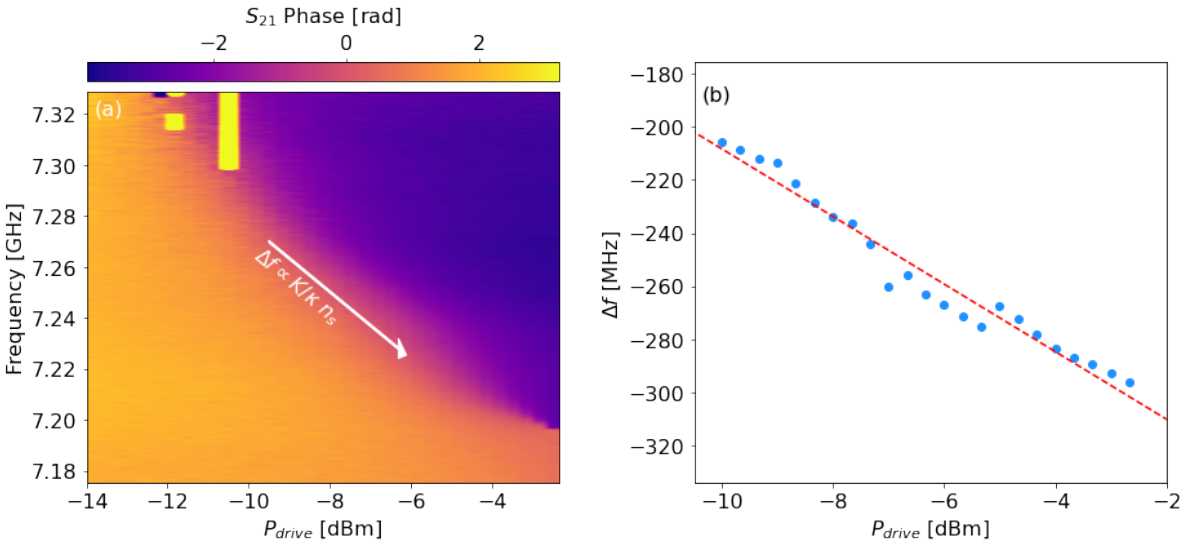

Figure 4.8: A negative frequency shift of the mode frequency $f_{2,-}$ is observed if the photon population of this mode increases in panel (a). This is demonstrated by plotting the complex phase drop of the mode as a function of drive power P_{drive}. The shift is indicated with a white arrow. Panel (b) presents the magnitude of the mode frequency shift Δf as a function of drive power P_{drive}. The red line is a fit to measured data.

Having found the resonance frequency of the mode as a function of drive power, it is possible to calculate the frequency shift Δf by subtracting the resonance frequency of the undriven mode. This frequency is $f_{2,-} = 7.49$ GHz. The frequency shift Δf is plotted in figure 4.8 (b). In addition to the measurement points, a linear fit of Δf as a function of drive power is shown. This fit was made using drive power up to $P_{\text{drive}} = -3.00$ dBm. Having found the mode frequency shift Δf as a function of drive power, we can estimate the photon population in mode $f_{2,-}$.

To make this estimate, we express the frequency shift Δf in terms of the mode population n_{mode} in mode $f_{2,-}$:

$$\Delta f \propto \frac{K_{\text{self}}}{\kappa} n_{\text{mode}}. \tag{4.1}$$

Only mode $f_{2,-}$ is considered, which has a self-Kerr coefficient K_{self} and decay rate κ. Both parameters stem from the design from section 3.1. For the considered mode $f_{2,-}$ the self-Kerr is $K_{\text{self}} = 13.985$ kHz and the decay rate is $\kappa = 106.4$ MHz. Using these parameters in our estimate for the cavity population, assumes their

design value is approximately correct. In turn the mode population can now be used to calculate the cold drive power of the mode [19]:

$$P_{\text{cold}} = \frac{\hbar\omega_{\text{drive}} n_{\text{mode}}}{\kappa}\left(\Delta\omega^2 + (\kappa/2)^2\right) \tag{4.2}$$

The angular frequency (difference) ω ($\Delta\omega$) can be converted in linear frequency f (Δf) by dividing it by 2π. The result is that we can link the applied drive power at room-temperature to the cold drive power P_{cold} at the entrance of the DJJAA.

The calculated cold drive power P_{cold} is plotted as a function of room-temperature drive power P_{drive} in figure 4.9. Fitting the calculated points with a first order polynomial, reveals that the estimated attenuation of the line is -42.50 dB. This is in good agreement with the nominal value of the attenuation on the input line, which is -40 dB. The difference can be explained by taking into account the attenuation of the wires. This estimate of the attenuation is not an exact calibration of the input line, which requires a more precise calibration technique. However, the resulting value is used as an indication of the attenuation down the input line.

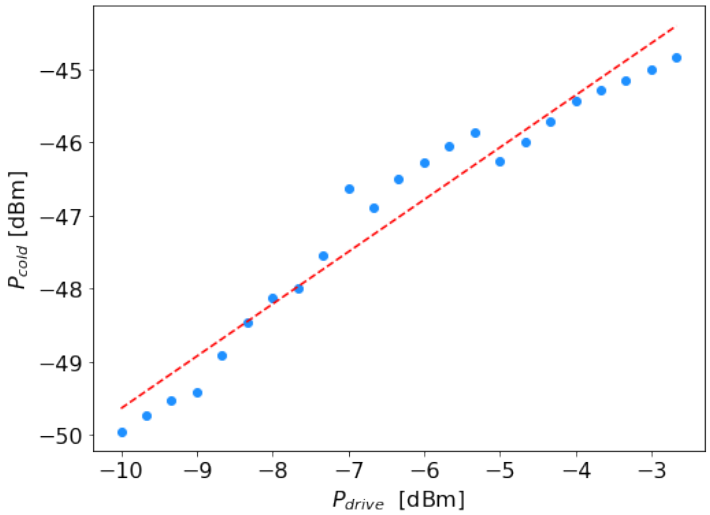

Figure 4.9: Calculated cold drive power P_{cold} as a function of room-temperature drive power P_{drive}. The data points are calculated from the frequency shift presented in figure 4.8. The red line is a fit of this data. The proportionality constant of this fit indicates that the attenuation of the input line is −42.5 dB.

4.1.5. Amplifier Saturation

The calculations for the DJJAA assumed that it is operated in the small-signal limit. For large signal powers, the amplifier saturates and gain decreases. Here, a measurement was done to determine the inset of amplifier saturation and calculate 1dB-compression point $P_{1\mathrm{dB}}$. This was done using the measurement protocol from section 3.5.3.

First the dimer drive is used to amplify an input signal in modes $f_{2,-}$ and $f_{2,+}$. Figure 4.10 (a) shows a measurement where the power of this input signal is increased stepwise. The input power of the DJJAA P_{cold} is acquired by combining the VNA power with the attenuation calibration from the previous section. In figure 4.10 (a), in both mode $f_{2,-}$ and $f_{2,+}$ the maximum signal gain decreases with increasing input power.

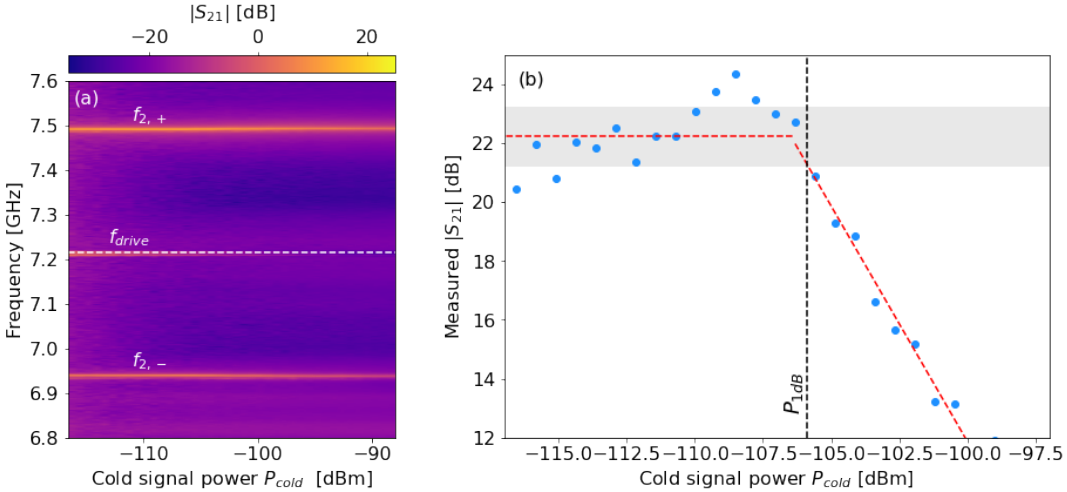

Figure 4.10: The S_{21} amplitude decreases by 1 dB above the saturation power. From a fit of the data in panel (b), it follows that $P_{1\mathrm{dB}} = -105.9$ dBm, which is indicated by a black dashed line. Panel (a) shows a measurement of the $|S_{21}|$ amplitude when the cold signal power P_{cold} from the VNA signal is increased stepwise. The mode frequencies $f_{2,-}$ and $f_{2,+}$ are indicated. In panel (b) the measured $|S_{21}|$ amplitude at the mode resonance as a function of signal power. The grey shaded area indicates a range of ±1dB around the nominal amplification.

Figure 4.10 shows the maximum $|S_{21}|$ value at each signal power in mode $f_{2,+}$. A similar plot for mode $f_{2,-}$ is found in appendix B.2. The measured data for mode $f_{2,+}$ indicates that $P_{1\mathrm{dB}} = -105.9$ dBm. This is in good agreement with the value found by Winkel et al., which is - 108 dBm [18]. At signal power below $P_{1\mathrm{dB}}$, the measured maximum $|S_{21}|$ increases with signal power. A plausible cause is that the signal-to-noise ratio of measurements at lower signal power is lower. This results in a lower measured $|S_{21}|$. A means to compensate for this effect, is by decreasing the IFBW for measurements at low signal power. By lowering the IFBW of a measurement, the noise integration time increases proportionally.

Section 2.4.2 predicted that amplifier saturation occurred due to a downward, Kerr-induced mode shift. We return to figure 4.10 (a) and look at the signal power larger than $P_{1\mathrm{dB}}$. No downward shift of the resonance frequency of both modes is visible with the bare eye. This is in contrast to the measurements presented in section 4.1.2, where an increase of the mode splitting was observed with increasing drive power. An increase in signal power leads to an increase in the mode population in the same way that an increase in drive power does. This would mean that mode splitting also increases if signal power increases. However, drive and signal power are both expressed in dBm, which is logarithmic. An increase in signal power, which is much lower than drive power, thus increases the mode population with a lower number of photons. The resulting increment in mode splitting would also be lower.

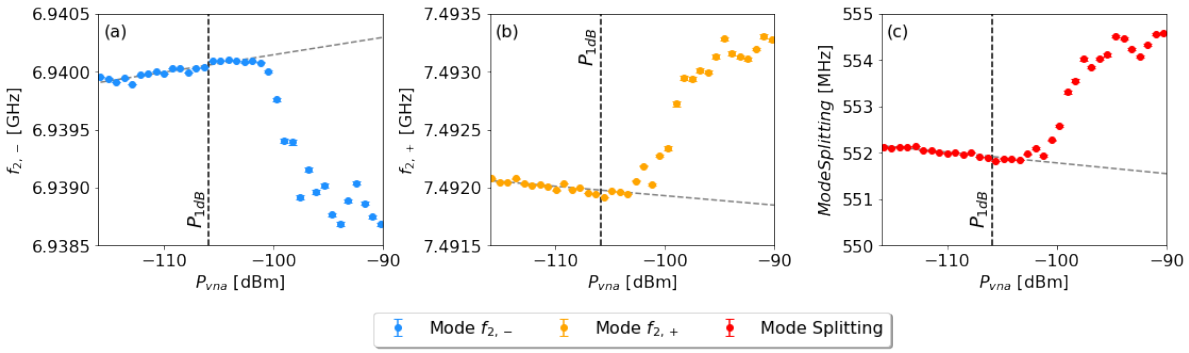

Figure 4.11: If signal power is increased above $P_{1\mathrm{dB}}$, a transition in the frequency of both modes is observed. This transition is not visible in the average resonance frequency. The resonance frequencies of mode $f_{2,-}$ (in panel (a)) and $f_{2,+}$ (in panel (b)) were fitted from the data in figure 4.10 (a). Panel (c) plots the average of the fitted mode frequencies. Dashed grey lines indicate a fit of the resonance frequencies below $P_{1\mathrm{dB}}$. The splitting between both modes initially decreases linearly below $P_{1\mathrm{dB}}$.

To confirm this hypothesis, fits of the resonant modes as a function of VNA signal power were made. This was done using the fit protocol in appendix A.1. The resulting resonance frequencies from these fits are plotted in figure 4.11 (a) and (b). The average frequency of both mode is plotted in figure 4.11 (c). Above $P_{1\mathrm{dB}}$ a transition in the frequency of the individual modes is visible. However, this transition is absent in the average frequency. It thus follows from these plots that mode splitting increases above the measured $P_{1\mathrm{dB}}$. It is possible that this abrupt increase in mode splitting is related to the onset of amplifier saturation. This would indicate that the coupling between both modes affects the saturation power.

In conclusion, the saturation power of the DJJAA was estimated to be $P_{1\mathrm{dB}} = 105.9$ dBm. It was not possible to conclude from our data what the mechanism is that causes saturation. A Kerr-induced frequency shift is known from theory to cause amplifier saturation. In addition, a change in the mode splitting between both resonant modes with pump power is observed. This change likely has an effect on the saturation measurements.

4.2. Observation of Self-Oscillations with a Bichromatic Drive

This part of the results chapter presents measurements on a single resonant mode when a bichromatic drive is applied. The bichromatic drive was presented in section 3.5.3. These measurements focus on understanding the relation between drive power and the strength of the measured output signal. Special attention was paid to the high drive power regime, where the measured amplification starts to decrease. In this regime we observed that the DJJAA started to emit microwave radiation at the mode resonance frequency.

In section 4.2.1, we present the amplified spectrum that is obtained by applying a bichromatic drive to a resonant mode of a DJJAA. Section 4.2.2 then discusses the low drive power regime of this mode, where the VNA signal is amplified. Subsequently, the effects of increasing the drive power are discussed in section 4.2.3. Here, we see that the DJJAA starts to send microwaves in a narrow band around the mode frequency.

4.2.1. Frequency Spectrum of the Bichromatic Drive

A different means of driving the DJJAA compared to the dimer drive, is by driving a single mode at once. As discussed in section 3.5.2 this can be done by using two drive tones, which are respectively red- and blue-detuned by an equal amount from the mode resonance frequency. This is the bichromatic drive.

A single frequency trace, with the bichromatic drive applied, is shown in figure 4.12. The drive power is expressed using the quantity P_{avg}, which is the average of the drive powers of both RF drives. The separation between the drive tones $2\Delta = 208$ MHz. The resonance frequency of mode $f_{2,-} = 7.104$ GHz and has $|S_{21}| = 13.24$ dB. At opposite detuning Δ of both drive tones, two smaller lineshapes are visible. These lineshapes are referred to as idler resonances. Idler resonances emerge if there is constructive interference between the VNA probe signal and an idler-sideband, which exists due to four-wave mixing between the drive tone and mode $f_{2,-}$. The emergence of idler resonances is investigated by Fani-Sani et al. [70].

Near both drive tones a measurement artifact is visible. In addition to a peak at the drive frequency, a second peak is visible at a slightly lower frequency. For both drive tones the detuning between these peaks is 6.00 MHz. This second peak is an artifact that emerges due to the way the VNA processes signals. This artifact is called image leakthrough.

In figure 4.12, a comparison to the background away from resonance indicates that $G > 20$ dB at the mode frequency $f_{2,-}$. The next part of this section will focus on the relation between signal amplification and drive power while using the bichromatic drive.

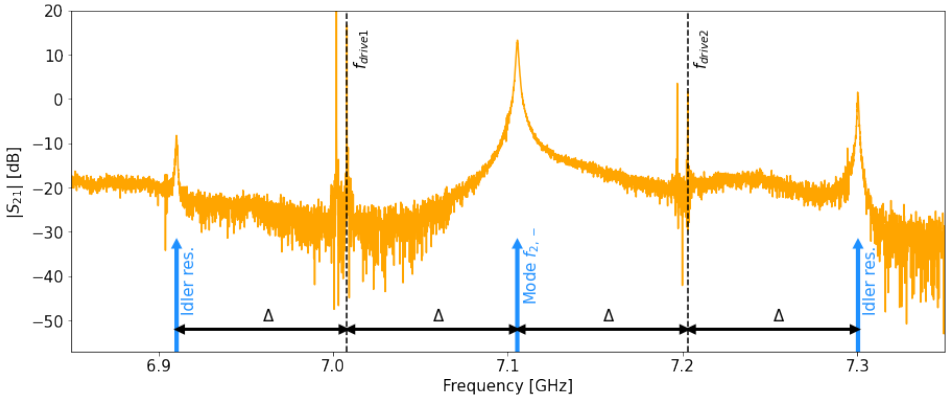

Figure 4.12: Measurement of the S_{21} amplitude around mode $f_{2,-}$ when a bichromatic drive is applied. Black dotted lines mark the drive frequencies $f_{\text{drive 1}} = 7.004$ GHz and $f_{\text{drive 2}} = 7.208$ GHz. Two peaks are visible near each drive frequency. One at the each drive frequency and a second peak detuned below both drive frequencies. The second peak is the result of image leakthrough. The detuning between both drive peaks is 6 MHz. Blue arrows indicate the mode resonance frequency $f_{2,-} = 7.104$ GHz and idler resonances. The detuning $\Delta = 104$ MHz between different features is indicated with black arrows.

4.2.2. Drive Power Dependence of Amplification in a Resonant Mode

For the measurement in the remainder of this section, a change in the measurement setup was made. In addition to the VNA, a spectrum analyzer (SA) was connected to the output line of the cryostat, as illustrated in figure 3.12 (b). This setup facilitates power spectral density (PSD) measurements using the spectrum analyzer.

The first measurements that were carried out with this setup, investigate the relation between the drive power and the measured amplification. The drive power is increased stepwise. The average drive power P_{avg} is calculated from the drive strength of both drive tones. They are driven with unequal power to correct for the attenuation in the directional coupler that combines both drive tones. After each increment of the drive power, a VNA sweep is performed. The drive frequencies have been manually fine-tuned with respect to the previous measurements, to compensate for shifts of the mode frequency between different thermal cycles of the cryostat.

Figure 4.13 shows the result of this measurement. The data is centered around the mode frequency $f_{2,-} = 7.118$ GHz to highlight increments in measured $|S_{21}|$ amplitude with increasing drive power. The width of the peak is observed to become narrower when its amplitude increases. Figure 4.13 (b) plots the largest measured value for the $|S_{21}|$-parameter as a function of average drive power . This is an indication of the maximum gain. A clear decrease in the measured gain is seen once the average drive power exceeds $P_{\text{avg}} = -2.0$ dBm. Above this power, a sharp decrease in the measured $|S_{21}|$ parameter is observed. It returns to similar values as when no RF drive is applied.

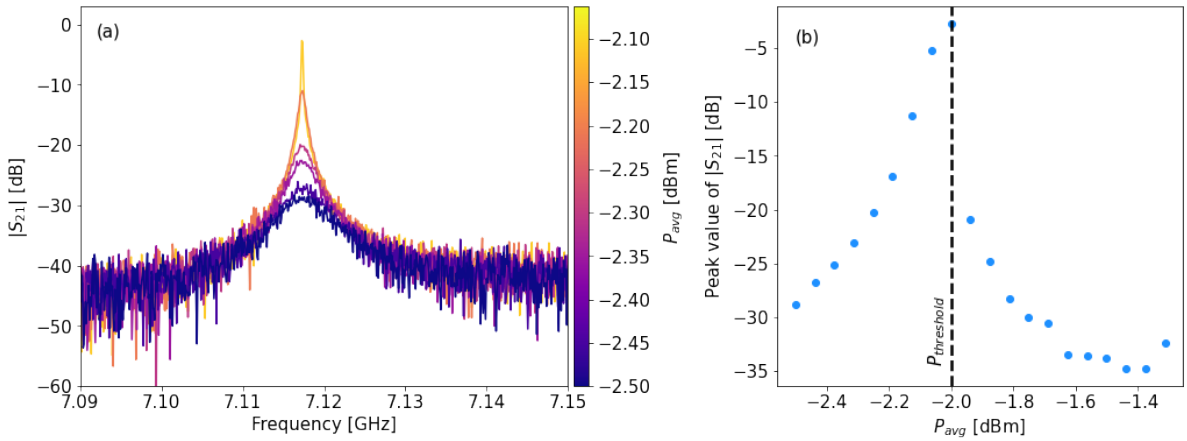

Figure 4.13: Increasing the drive power P_{avg} increases the measured amount of amplification in mode $f_{2,-}$ until the drive power increases beyond a threshold. In panel (a) different-coloured linecuts show the response of mode $f_{2,-}$ to a probe signal at increasing drive power. An increasingly high and narrow peak emerges. Panel (b) shows the value of S_{21} amplitude at the mode resonance frequency $f_{2,-}$ in each trace. A black dotted line indicates the threshold power $P_{\text{threshold}}$. Above $P_{\text{threshold}}$ a sharp decrease of the peak value of the $|S_{21}|$ is observed.

Our treatment of DJJAA modes as Kerr-oscillators in section 2.4.2 predicted that if the mode population becomes too large, the mode frequency shifts down. This leads to a reduction in the amount of signal amplification. However, for drive power up to $P_{\text{avg}} = -2.00$ dBm, no shift of the mode resonance frequency is observed. This is conflicting with this explanation. An explanation is that at high drive power, the device is driven into a regime where it becomes self-oscillating. This would cause signal amplification to decrease as well, because the drive power is dissipated through amplified vacuum fluctuations. In the next subsection this hypothesis will be investigated further.

4.2.3. Observation of Self-Oscillations in a Resonant Mode

In section 4.2.2 a clear decrease in measured signal strength was observed if the RF drive power was increased above $P_{\text{avg}} = -2.00$ dBm. As an hypothesis it was proposed that above this drive strength, the mode becomes self-oscillating. It then dissipates drive power through amplified vacuum fluctuations at the resonance frequency.

To investigate this hypothesis, the drive power measurement that was proposed in section 4.2.2 is repeated. The average drive power is increased to a maximum of $P_{\text{avg}} = -0.75$ dBm. After each increment of the drive power, two measurements are done: First, the VNA measures the response of the DJJAA to a probe signal along a frequency range around the mode $f_{2,-}$. The VNA probe has power $P_{VNA} = -60$ dBm. Then the SA is used to perform a measurement of the PSD along the same frequencies. During SA measurements no probe signal is send into the device. This subsection first presents the measurements on the VNA and subsequently the complementing PSD measurements.

VNA measurements

Figure 4.14 shows the measured data that was obtained in the VNA. In panel (a), the $|S_{21}|$ response is mapped as a function of VNA probe frequency and drive power. Panel (b) and (c) each display a single linecut from (a), which indicate the different responses of the mode when drive power is increased. An important difference is that the plot in panel (a) is on a logarithmic scale, whereas the linecuts in panel (b) and (c) are displayed on a linear scale.

In panel (a), no amplification of the VNA probe is visible at drive power lower than $P_{\text{avg}} = -2.60$ dBm. A maximum in the amplified spectrum is observed once the drive is increased to $P_{\text{avg}} = -2.08$ dBm. A peak can can be distinguished around $f_{2,-} = 7.117$ GHz, indicating that this is the mode frequency $f_{2,-}$. If the drive power is further increased above this, the measured $|S_{21}|$ value initially decreases. However, at high enough drive power, two lineshapes emerge at frequency 7.111 GHz and 7.117 GHz. Both lineshapes are visible on a linear scale in panel (c), which is taken at drive power $P_{\text{drive}} = -1.49$ dBm. If we return to panel (a), we see that these peaks become brighter with increasing drive power. This tells us that the returned $|S_{21}|$ increases as well. A comparison between the peaks in figure (b) and (c) shows us that the linewidth in the peak at lower drive power (panel (b)) is smaller than at higher drive power (panel (c)).

The emergence of a second lineshape above $P_{\text{avg}} = -2.00$ dBm cannot be explained by the Kerr-oscillator treatment of the DJJAA in section 2.5. A possible explanation can be inferred from the detuning between both peaks, which is equal to 6.00 MHz. This is the exact same value as the detuning between the two peaks of each drive tone in section 4.2.1. This indicates that it is likely that the emerging lineshape at 7.111 GHz in figure 4.14 (a) is the result of image leakthrough. This artifact suggests that the lineshape at $f_{2,-} = 7.117$ GHz is not solely the result of the amplified VNA probe signal. Instead, this radiation is emitted by a source external to the VNA. This source likely is the mode $f_{2,-}$. This supports the hypothesis that the resonant modes becomes self-oscillating if the drive power is increased above -2.00 dBm.

SA measurements

At each drive power, VNA measurements are complemented with PSD measurements along the same frequency range on the SA. These measurements are shown in figure 4.15. Panel (a) maps the PSD for different measurement frequencies and drive powers. Panel (b) and (c) again show a linecut from panel (a). These linecuts were measured at the same drive powers as the linecuts in figure 4.14 and are again plotted on a linear scale.

One can see in panel (a) that at drive power below $P_{\text{avg}} = -2.60$ dBm only background fluctuations are measured. At drive power $P_{\text{avg}} = -2.08$ dBm, there is a region where power is emitted around the resonance frequency. This region coincides with a region of amplification visible in figure 4.14 (a). Around $P_{\text{avg}} = -1.50$ dBm, a brighter line emerges. Panel (b) shows a linecut in which the corresponding peak is visible. This peak has an amplitude that is approximately twice the amplitude of the peak at $P_{\text{drive}} = -2.08$ dBm, which is plotted in panel (c). The frequencies range around which the peaks is visible, is observed to be approximately the same. This indicates that the peak at high drive power (panel (b)) has a linewidth that is much smaller than the peak at lower drive power.

A comparison of figure 4.14 and 4.15 is made to link the VNA and SA measurements. We first focus on the amplified region that is visible around drive powe $P_{\text{avg}} = -2.08$. In figure 4.14 (a), the slope of the peak is smooth until it increase to a maximum. This indicates that this is the result of amplification of the VNA probe signal and that the emitted power measured by the SA at $P_{\text{avg}} = -2.08$ dBm is due to amplification of thermal noise.

If we turn to the linecuts at high drive power ($P_{\text{avg}} = -1.49$ dBm), we observe that the slope of the peaks is less smooth. Combined with the emitted power that was measured on the SA at this drive power, this indicates that it is possible that the hypothesis that the mode is self-oscillating is correct . The observed narrowing of the measured linewidth of the peak is in agreement with this conclusion.

The observed self-oscillations, indicate that the DJJAA should be driven with sufficiently low power when operating it as an amplifier. However, it also reveals another manner of operation for the device. The DJJAA could be used as a source of cryogenic microwave radiation at a tunable frequency. This requires to investigate of the bandwidth if the emitted radiation has a bandwidth smaller than the bandwidth of the applied RF drive tones. Additionally, it should be verified that the noise of the emitted radiation is uncorrelated with the noise in both drive tones. These experiments are interesting for further research.

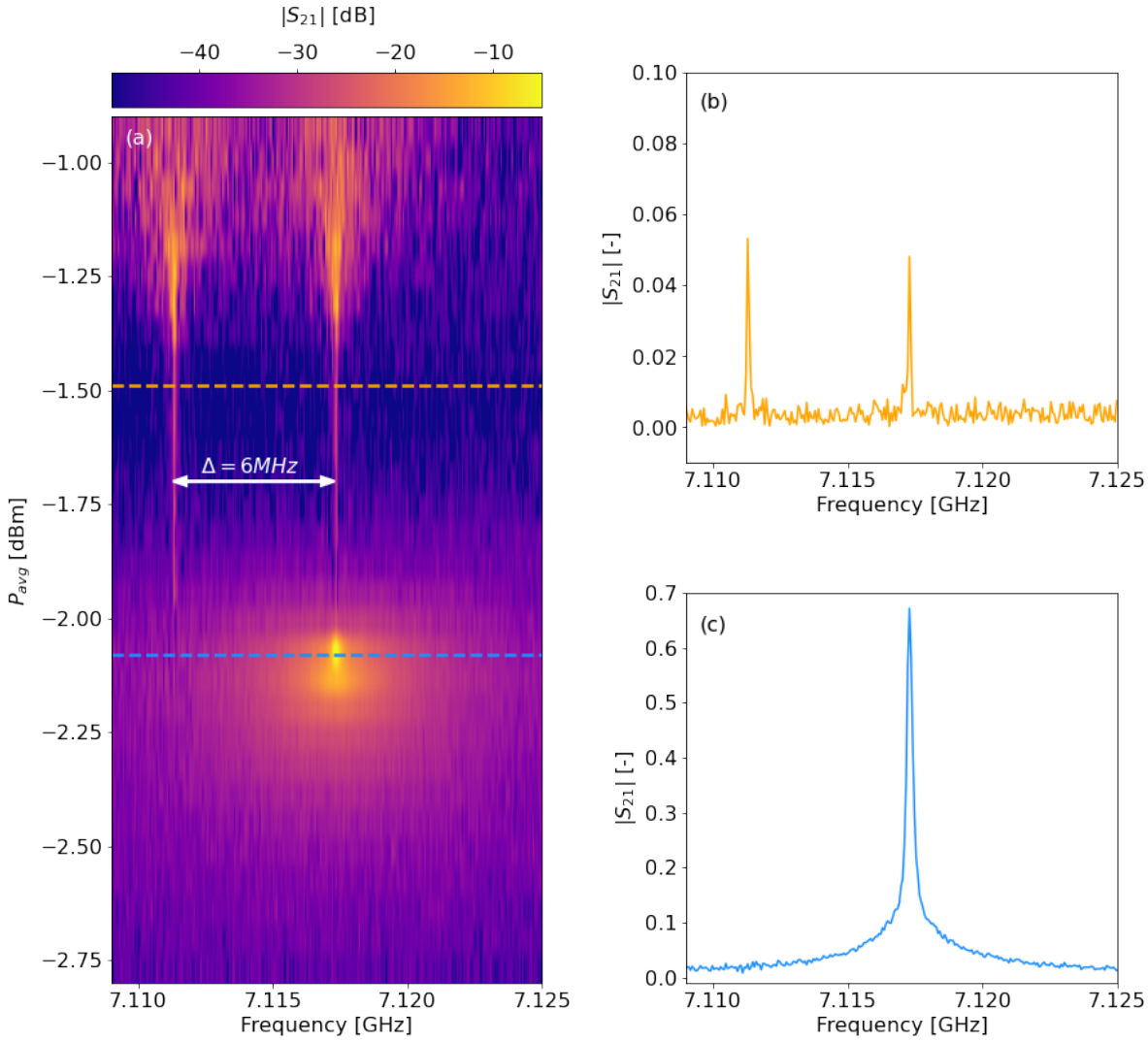

Figure 4.14: A peak emerges due to image leakthrough if the drive power is increased above $P_{\text{drive}} = -2.00$ dBm. Below $P_{\text{drive}} = -2.00$ dBm a signal at the input of the DJJAA is amplified. Panel (a) shows the measured $|S_{21}|$ parameter for VNA traces at increasing drive power. Linecuts from panel (a) indicate the different drive power regimes in panel (b) and (c). A region of large amplification is visible below $P_{\text{avg}} = -2.00$ dBm at frequency $f_{2,-} = 7.117$ GHz. If the drive power is increased, this amplification initially disappears, At higher drive power two peaks emerge, which are detuned by $\Delta \approx 6$ MHz. The peak at frequency 7.111 GHz is the result of image leakthrough in the VNA.

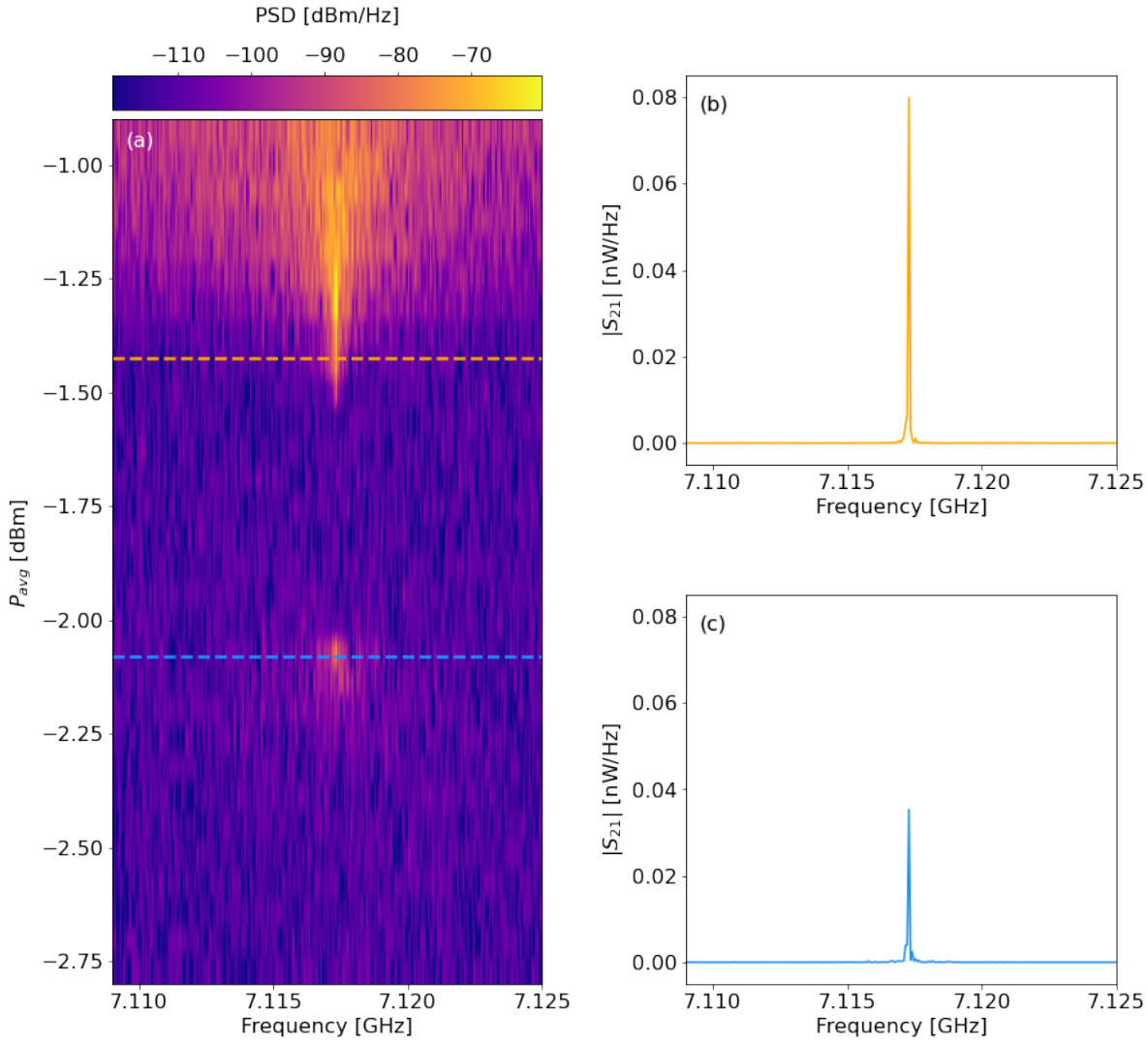

Figure 4.15: Measurements of the PSD using the same drive parameters as the VNA measurements from figure 4.14. Panel (a) displays PSD measurements at increasing drive power P_{avg}. Panel (b) and (c) display two linecuts at different drive powers P_{avg} from panel (a). The origin of the peaks in figure (b) and (c) is likely to be different. The linecut in panel (b) was made at $P_{\text{avg}} = -1.40$ dBm and is likely the result of amplified thermal noise. the linecut in panel (c), at $P_{\text{avg}} = -2.10$ dBm, is the result of self-oscillations. In panel (a) this peak emerges around the mode frequency $f_{2,-}$ at high drive power ($P_{\text{avg}} = -1.60$ dBm), indicating that the DJJAA emits power at this frequency.

4.3. Measurements on the TUD-DJJAA

Part of this thesis project to develop a recipe for DJJAA fabrication in the Kavli Nanolab. A DJJAA that was fabricated according to this recipe was presented in section 3.2.5. We will now discuss the measurements that were done to characterize this device. The first measurement was a flux-modulation measurement, to verify if the resonant modes of the device could be measured. This was followed by an attempt to amplify a probe signal from the VNA using the bichromatic drive. This measurement is discussed in section 4.3.2.

For the measurements on the TUD-DJJAA, the measurement setup is connected directly to the VNA, as illustrated in figure 3.12 (a).

4.3.1. Observation of the Resonant Modes

As a first means of testing if the fabricated device functions as intended by its design, is to perform a flux-bias sweep. This serves two purposes: firstly, it tells us if we can measure any resonant modes at all. Secondly, it contains information on the resonance frequency of the measured dimer modes. During the measurement, the VNA frequency range was set from 3.5 GHz to 8.5 GHz. The DC bias current was varied between -9.5 mA to +6.5 mA. A VNA probe with power $P_{\text{VNA}} = -60$ dBm was used.

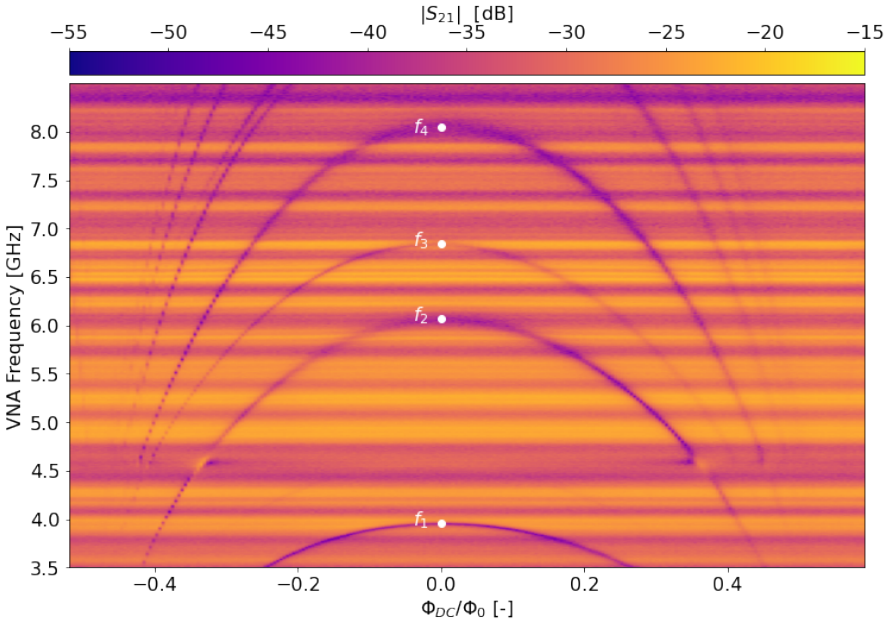

Figure 4.16: Four resonant modes can be flux-modulated by changing the DC flux bias. From the mode-spacing it is not apparent which modes form dimer pairs. The individual modes are labelled according to their frequency at the flux sweet-spot. The plot displays the amplitude of the S_{21} parameter

Figure 4.16 shows the resulting measurement. Four arcs are visible ,which correspond to a single resonant mode each. Two additional modes are visible for $|\Phi_{DC}| > 0.25\Phi_0$. The four complete arcs are labelled with indices $i = 1$, to 4. This notation is different than for the modes in the KIT-DJJAA, for reasons that will be explained later in this section. The mode frequencies at the flux sweet spot are extracted from figure 4.16. They are listed in table 4.2. As in the measurements in section 4.1.1, horizontal lines are seen, which originate from impedance mismatches in the input and output lines of the cryostat. The effect of impedance mismatches on transmission is discussed in section 4.1.1.

Table 4.2: Measured resonance frequencies of the modes in the TUD - DJJAA.

Mode Index	f_1	f_2	f_3	f_4
Measured	3.935 GHz	6.045 GHz	6.815 GHz	7.985 GHz

By comparison of the resonance frequencies in table 4.2 with the design resonance frequencies in table 3.1, it becomes clear that they are different. A plausible origin of this discrepancy is an offset in the normal state resistance measurements on this DJJAA. In section 3.2.5 it was stated that for this device $R_{\text{top}} = 51.95$ kΩ and $R_{\text{bot}} = 57.89$ kΩ. Both are larger than the design values in table 3.1, which are $R_{\text{top}} = 35.13$ kΩ and $R_{\text{bot}} = 34.55$ kΩ. The effect on the mode frequency of this offset can be understood via the SQUID inductance. Section 2.6.4 explained that the critical current of a SQUID is inversely proportional to the measured normal state resistance. In turn, the SQUID inductance is inversely proportional to the critical current. It follows that a higher normal state resistance leads to a larger SQUID inductance. The resonance frequencies of the device can be calculated as $\omega_{res} = 1/\sqrt{LC}$. The increased normal state resistance results in lower frequencies of the measured resonant modes in the TUD-DJJAA.

In figure 4.16 and table 4.2, it is not immediately clear which modes form dimer pairs. A likely cause is the mismatch in normal state resistance between R_{top} and R_{bot}. The consequence of this mismatch is that the top and bottom part of the DJJAA array resonate at different frequencies. Section 2.5.2 explained that two modes need to resonate at the same frequency in order for them to form a dimer. We thus expected that the resonant modes in the TUD-DJJAA have not dimerized due to a mismatches in their mode frequencies. This is supported by the difference in linewidth that can be observed between mode f_3 on one hand and on the ohter hand mode f_2 and f_4. This difference in linewidth suggests they correspond to two different resonators with a different coupling to the feedline of the DJJAA.

In conclusion, it is possible to locate the different resonant modes in the TUD-DJJAA. The spacing between the separate modes is larger than the 600 Mhz between two dimer modes intended in the design. It is likely that the different modes do not form dimers. This can potentially be verified by applying a dimer drive to both modes and extracting the observed shifts in resonance frequencies as a function of drive power. If the modes form a dimer, the splitting between their mode frequencies will increase with drive power, as explained in section 2.5.2. If they do not form a dimer, both modes will only shift down in frequency. This experiment would be interesting for further research. Measurements using the bichromatic drive were done on the TUD-DJJAA, which are presented in the next subsection.

4.3.2. Signal Amplification in a Resonant Mode

The previous section demonstrated that it was possible to locate resonant modes in the TUD-DJJAA, but that these modes do likely not form dimers. In order to drive these modes, it was thus chosen to drive a single mode using the bichromatic drive. Here we will discuss the amplified spectrum that was measured while driving.

It was decided to drive mode f_3. No DC bias current was applied ($I_{\text{bias}} = 0$ mA). AC drive tones were placed at $f_{\text{drive 1}} = 6.650$ GHz and $f_{\text{drive 2}} = 6.858$ GHz. A VNA probe signal was send and measured at frequencies between 6.63 GHz and 6.87 GHz with power $P_{VNA} = -60$ dBm. A trace of the background was done with the same VNA settings while both drive tones were turned off.

The resulting measurement is presented in figure 4.16. A peak is visible in the center of this graph, which correspond to the mode frequency. A fit of this spectrum, which is discussed in appendix A.2, reveals that the mode frequency $f_3 = 6.754$ GHz. At first glance it appears that the amplitude of this peak is > 20dB compared to the background. To estimate the maximum gain, the background trace was subtracted from this measurement (see appendix A.2). This led to an estimate of the maximum gain of $G_{\text{max}} = 27.7$dB. An estimate of the frequency range, over which amplification larger than 20 dB is achieved, is $BW_{20} = 2.5$ MHz.

The DJJAA can be modelled as two separate oscillators coupled through a center capacitor, as explained in section 2.5.2. The resonant mode of both oscillators are coupled capacitatively to form dimers. In section 4.3.1 it was argued that the resonant modes in the TUD-DJJAA likely do not form dimers due to a mismatch in normal state resistance of the oscillators. This would mean the amplification field, which was measured in figure 4.17, is amplified in only one of the two resonators of the DJJAA. The other resonator can potentially act as an additional loss channel for the fields, which limits the gain in the mode.

In this section we demonstrated that it was possible to achieve more than 20 dB of gain in a resonant mode in the TUD-DJJAA. More measurements on the fabricated DJJAA are necessary to fully characterize its performance as an amplifier. In section 4.3.1 we saw that the resonant modes in this device are likely do not form dimer pairs. This is a consequence of a mismatch in the normal state resistance of the junction array, which in turn is the result of a too thick junction oxide barrier. Improving this issue requires improvements in the fabrication recipe that was set apart in section 3.2.1. This discussion on the performance of DJJAAs fabricated at TU Delft marks the end of this results chapter. In the next chapter of this we will summarize the conclusions from this thesis project and discuss possible goals for further research.

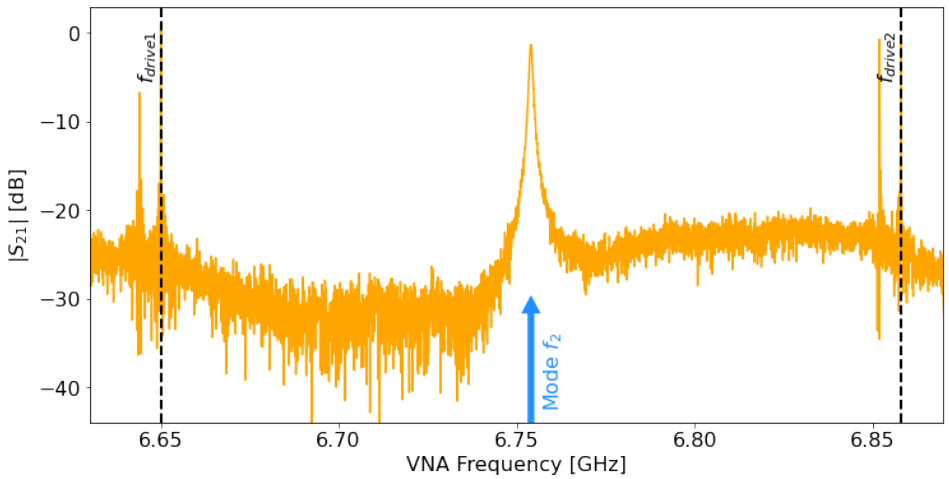

Figure 4.17: A peak emerges at the mode frequency f_2 if two drive tones are applied around it. The drive frequencies $f_{\text{drive 1}}$ and $f_{\text{drive 2}}$ are marked by black dashed lines. The mode frequency $f_3 = 6.754$ GHz is indicated by a blue arrow. Background subtraction reveals that at this frequency $G > 20$ dB over an estimated bandwidth $BW_{20} = 2.5$ MHz.

5

Conclusions & Outlook

The goal of this thesis was to characterize and fabricate dimer Josephson junction amplifier arrays (DJJAAs). The behaviour of a DJJAA was described by modelling it as a Kerr-oscillator and characterized in terms of maximum gain and saturation power. By driving a single mode of this device using two RF drive tones, the onset of self-oscillations was observed. The fabrication of DJJAAs was done using overlap Josephson junctions. Several issues with the fabrication process of overlap junctions were resolved. From measurements of the resonant modes in a fabricated DJJAA, the quality of the fabrication process was assessed.

The conclusions and recommendations are divided in two parts. The first part treats the conclusions relating to characterization of a DJJAA fabricated in Karlsruhe Institute of Technology (KIT). The second part treats the fabrication of DJJAAs during this thesis project.

Characterization of a DJJAA
The performance of a DJJAA as a parametric amplifier was assessed. This device was fabricated by Ioan Pop [18] at KIT. In this device two dimers, consisting of two resonant modes each, could be flux-modulated with a DC flux bias to cover the complete 4 to 8 GHz frequency range.

The two resonant modes in a dimer were parametrically driven by applying a drive tone in between their resonance frequencies. In this manner a maximum gain $G_{\mathrm{max}} = 43.6$ dB was measured. If the power of the drive tone was increased, the average of the dimer resonance frequencies was found to decrease. This negative frequency shift is induced by the Kerr-nonlinearity and is dependent on the photon population of the dimer modes. On top of this shift, the frequency splitting between both modes in a dimer increased as a function of drive power. It was demonstrated that the frequency of the parametric drive has to be adjusted to these shifts of the mode resonance frequencies, in order to obtain maximum signal amplification.

A calibration of signal power at the input port of the DJJAA was done in order to estimate the saturation power. This calibration exploited the Kerr-shift of a resonant mode to calculate the photon population of the mode. The photon number in the mode could then be converted in the cold signal power at the input of the DJJAA. By comparison with the drive power at room temperature, it was found that the attenuation of the input line was -42.50 dB. This value is close to the nominal value of the attenuation on the input line, which was -40 dB. The difference was explained via attenuation in the cables connecting the different plates in the dilution refrigerator. Using the calibrated attenuation of the input line, a measurement of the saturation power found that the 1dB-compression point was $P_{\mathrm{1dB}} = -105.9$ dBm.

The onset of self-oscillations was studied in a single resonant mode of the device. This was done by placing two drive tones, with equal but opposite detuning, around a single resonant mode. If the drive power increased above a threshold, it was observed that the signal amplification in this mode dropped sharply. Measurements of the power spectral density revealed that above this threshold, the mode started emitting power at its resonance frequency in the absence of an input signal. This indicated that the mode was self-oscillating. In measurements with the vector network analyzer, which sends an input signal into the DJJAA, these self-oscillations were discerned by the emergence of a second line shape at a fixed detuning below the

resonance frequency. This second lineshape is the result of image leakthrough. Image leakthrough indicates the presence of a strong microwave signal, which does not originate from the vector network analyzer.

Fabrication of DJJAAs
In this thesis project the focus of DJJAA fabrication was on fabricating working overlap junctions. The Josephson barrier was grown by flowing oxygen on the junction area A. This process was calibrated to happen at 30 mbar for 3:15 min. This calibration was necessary due to the large size of the Josephson junctions ($A = 16$ μm^2). The normal state resistance of the resulting junction arrays were measured to be 51.95 kΩ and 57.89 kΩ, whereas they were designed to be 35.13 kΩ and 34.55 kΩ. This deviation is the consequence of a too high oxidation pressure.

A DJJAA resulting from this fabrication process was measured. By varying a DC-flux bias, it was possible to flux-modulated four resonant modes, which together covered the 4-8 GHz frequency range. These four resonant modes had a lower resonance frequency than intended in their design and did not form dimers. This was the result of a mismatch in the Josephson junction inductance, which was inferred through measurements of the normal state resistance of the junctions. A single resonant mode was driven using by applying two RF drive tones around the mode. In this manner maximum gain $G_{\max} = 27.7$ dB with a 20dB bandwidth of 2.5 MHz was observed. Further characterization of fabricated DJJAAs is necessary to assess their performance as parametric amplifiers.

Outlook
In this thesis multiple directions for further research were identified. First of all characterization of DJJAAs can be done with more extensive calibration of the background, such as a short-open-load calibration. This could serve to extract amplifier benchmarks, such as the gain-bandwidth product and noise visibility, more accurately in DJJAAs.Further measurements on the observed self-oscillations could potentially demonstrate the applicability of DJJAAs as a flux-tunable source of cryogenic microwave radiation. This would require to accurately determine the bandwidth, drive power-dependence and noise correlations of the emitted radiation.

The fabrication process of overlap junctions in this thesis leaves room for further improvements. First of all, the oxidation of the Josephson barrier should be calibrated such that the thickness of the grown barrier saturates during oxidation. This requires that this step is performed at a lower oxidation pressure. Additionally, it re-calibrating the amount of time that argon milling is done, could limit damage to the aluminum on the bottom layer of Josephson junctions.

A

Data Processing

A.1. Fit Protocol

The results chapter of this thesis presents measured data on the resonant modes of a DJJAA. If these modes are driven, the resulting lineshape is approximately Lorentzian. This appendix elaborates on the fitting method that was used to extract the resonant frequency of these modes.

Fits were made of the spectrum measured on the VNA. This fit was made on $\left|\mathrm{Re}(S_{21}) + j\,\mathrm{Im}(S_{21})\right|$. The fits ware made using a Lorentzian function $f(\omega)$

$$f(\omega) = A\frac{\sigma}{(\omega-\omega_0)^2+\sigma^2}. \tag{A.1}$$

In this function ω_0 is the center frequency of the Lorentzian, σ is a parameter that specifies the width of the Lorentzian and A is used to scale the height of the lineshape. The fitting error was estimated by taking the square root of the covariance of each fitted parameter. Only the fitted resonance frequency was used in our data analysis.

An example of a fit made on the data presented in figure 4.3 is shown in figure A.1. This fit was made on mode $f_{2,-}$, while a dimer drive was applied at $f_{drive} = 7.459$ GHz with drive power $P_{drive} = 3.6$ dBm. The resonance frequency found from this fit was 7.181 GHz ±5.158 kHz.

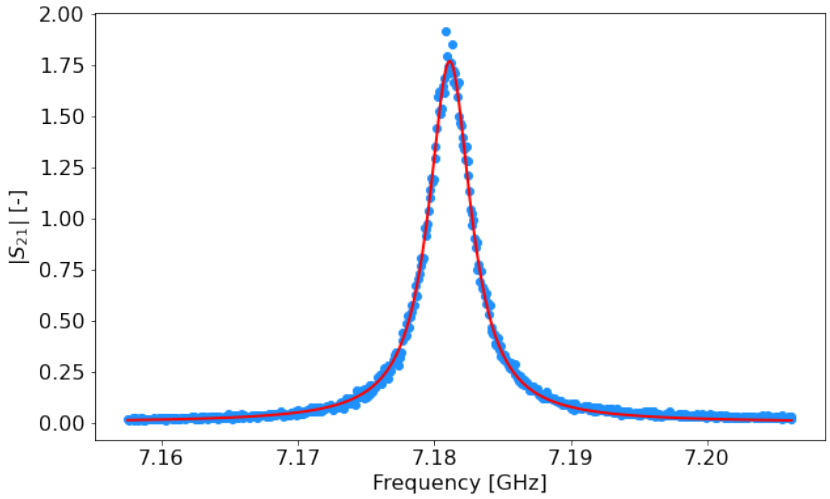

Figure A.1: A fit of the linear $|S_{21}|$ amplitude of mode $f_{2,-}$ while it is driven with the dimer drive. The measured data is indicated with blue dots, the fit of the mode as a red line.

A.2. Estimation of Gain in the TUD-DJJAA

Section 4.3.2 discussed S_{21} measurements that were done on the TUD-DJJAA when it was driven using the bichromatic drive. In order to assess if this device can amplify a signal sufficiently for use in an experiment, we needed an estimate of its gain and operational bandwidth at the resonance frequency. In order to estimate these parameters, two measurements were done. In the first measurement, the resonant mode is driven using the bichromatic drive to create significant gain. During the second measurement no drive is applied, so that only the background is measured. Both measurements are plotted on top of each other in figure A.2 (a).

To extract the resonance frequency, we followed the procedure discussed in A.1. For an estimate of the gain we subtracted the background from the measurement when the drive was applied. The result in figure A.2 shows that a ripple in the background, which was present in figure A.2 (a), has disappeared. The maximum gain G_{max} is defined as the maximum rise compared to the undriven background. From this plot it is estimated as $G_{max} = 27.7$ dB. The 20dB-bandwidth BW_{20} is the continuous bandwidth above which the signal gain is larger than 20dB. From figure A.2 it is estimated that $BW_{20} \approx 2.05$ MHz

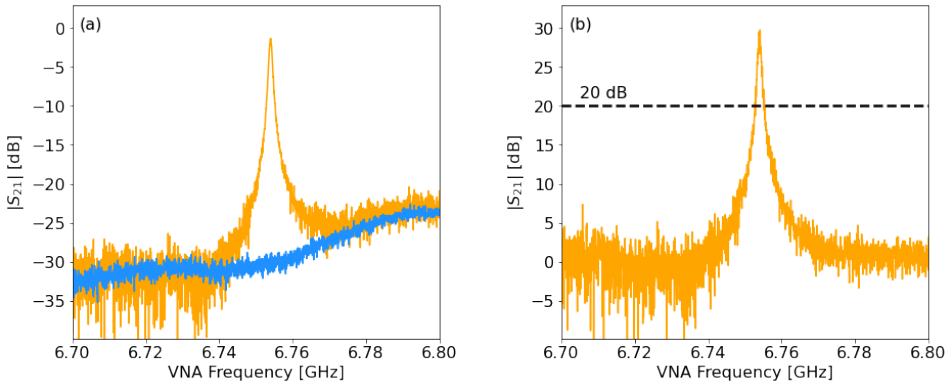

Figure A.2: Panel (a) shows the measured S_{21} spectrum of the mode f_3 in the TUD-DJJAA when it is driven (orange) using the bichromatic and the undriven background (blue). In panel (b) the background is subtracted from the driven mode. A black dashed line indicates gain larger than 20 dB.

B

Dimer Drive Measurements

B.1. Drive Power Measurements on Dimer 1

Section 4.1.2 presents measurements on the drive power-dependence of amplification in dimer 2 using the dimer drive. Here we present the same measurements done for dimer 1. A drive tone was applied at f_{drive} = 4.495 GHz. A single trace of the whole spectrum is shown in figure B.1 (a). At this drive power the resonant modes have frequencies $f_{1,-}$ = 4.175 GHz. and $f_{1,+}$ = 4.815 GHz. The detuning at P_{drive} = 9.5 dBm is close to 320 MHz.

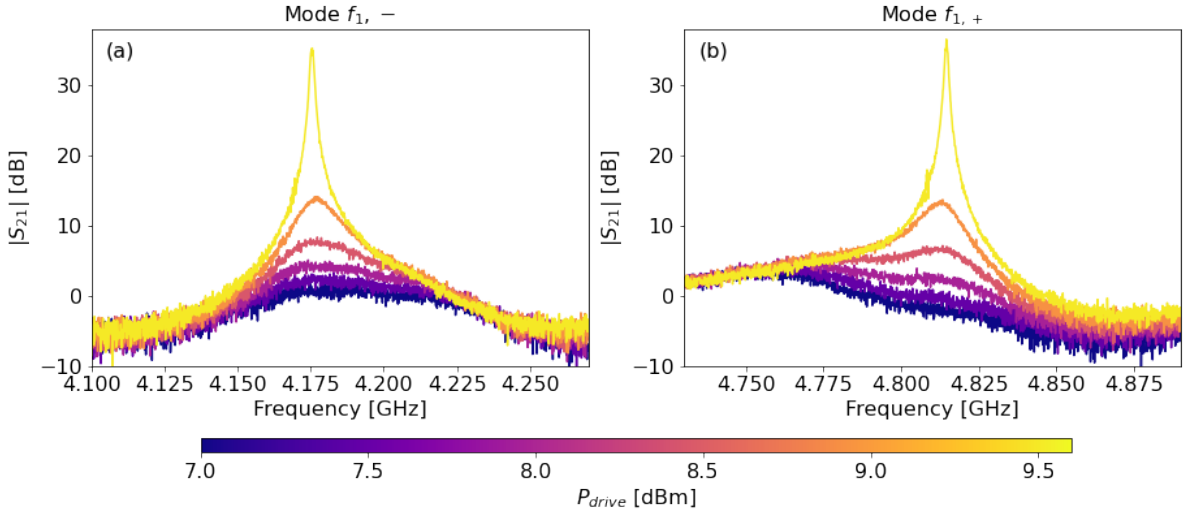

Figure B.1: Gain spectrum of mode $f_{1,-}$ (panel (a)) and $f_{1,+}$ (panel (b)). When drive strength is increased, an increasingly high and narrow peak emerges.

The measured $|S_{21}|$ parameter is plotted as function of drive power for mode $f_{1,-}$ (panel (b)) and mode $f_{1,+}$ (panel (c)). An immediate difference with the same measurement on the modes of dimer two (presented in figure 4.2) is that the resonance frequencies $f_{1,-}$ and $f_{1,+}$ stay approximately constant as a function of drive power. The fitted resonance frequencies are plotted as a function of drive power in figure B.2. The upward shift of the average mode frequency in panel (c) of this figure is due to fitting errors on mode $f_{1,+}$, which result in too high reported resonance frequencies. The lessed extend to which dimer 1 mode splits with increased drive power is attributed to a small Kerr-nonlinearity of both dimer modes. The Kerr-nonlinearity was calculated from the DJJAA design in section 3.1.

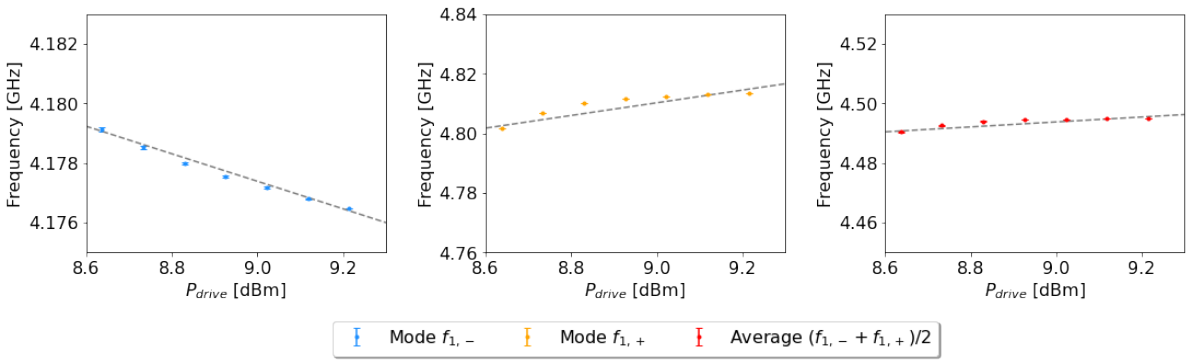

Figure B.2: Fits of the mode resonance frequencies of dimer 1 as a function of drive power. The upward shift of the average mode frequency is the result of fitting errors due to large background fluctuations.

B.2. Saturation Power Measurements on Mode $f_{2,-}$

Section 4.1.5 presented saturation power measurements on the uncalibrated gain on dimer mode $f_{2,+}$. Here the same measurements are presented for the mode $f_{2,-}$, which is the other mode in the same dimer. This is shown in figure B.3. The saturation power of the dimer drive that was extracted from this mode is $P_{1dB} = -104.9$ dBm. It is likely that this difference in saturation power disappears if a calibration of the input/output lines is done to account for impedances mismatches.

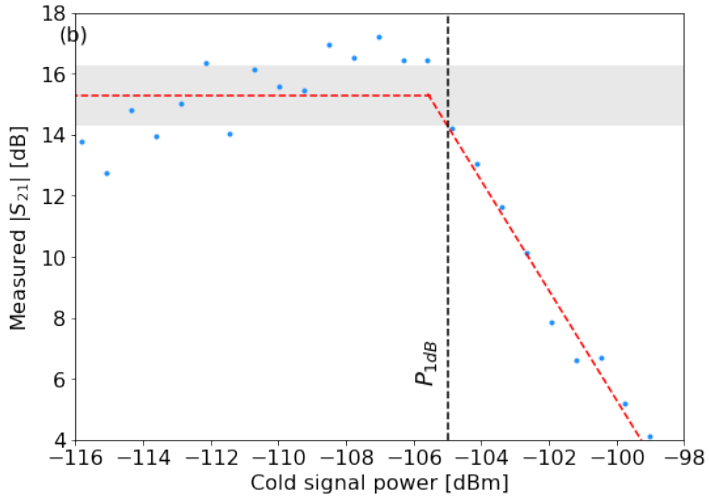

Figure B.3: Saturation power measurement on dimer mode $f_{2,-}$. The shaded gray area indicates the nominal value of amplification before amplifier saturation sets in.

C

DJJAA Recipe

This section contains the complete recipe for overlap junctions that was used to fabricate the last iteration of DJJAAs during this thesis project. This recipe was carried out in the Kavli Nanolab. This recipe considers the situation, where a 330 µm thick, 2-inch sapphire wafer is processed, on which multiple DJJAAs are fabricated.

Step 1: Evaporation of the platinum groundplane.
Use a qutip dipped in IPA to wipe the surface of the wafer. Place in IPA for 2x 5 min. Load the wafer into the Temescal. Use tape to place attach the wafer to the sample holder. Once it is pumped vacuum, evaporate first 5 nm of titanium on the wafer as a sticking layer. Second evaporate in total 140 nm of platinum on top. Unload the wafer from the Temescal. Clean the residuals from the tape with a qutip dipped in acetone. Submerge 3 min in acetone and 3 min in IPA. Blow dry immediately when removing from IPA. The topside of the wafer is the side without platinum on it.

Step 2: Bottom Aluminium layer.
Spin resist LOR-5B at 5000 rpm on the topside of the wafer. Immediately bake for 3 minutes at 180 °C. On top spin a second layer of resist - AZ5214 at 6000 rpm. Bake 1 minute at 110 °C. Write the pattern for the bottom layer of the junctions in the Heidelberg µMLA with dose 117 mJ/cm^2. Use pneumatic focussing. Develop the resist in MF321 for 75 seconds. Rinse in demiwater for 2 times 30 seconds. Immediately blowdry when removing from water.

Load the sample in the Tepla for an O_2 descum for 2 min. Use 200 W and 200 sccm of O_2. Load the wafer into the Plassys. Once the Plassys is pumped vacuum, do a 20 nm titanium gethering of the oxidation chamber to further decrease the pressure. Deposit 30 nm of aluminium on the chip at zero angle and rate 0.5 nm/s. Finish the process with an oxide capping layer at 1.3 mbar for 11 minutes. Remove the wafer from the Plassys.

Place the wafer in NMP for overnight liftoff. Before removing from NMP, use a pipet to blow large aluminium flakes of the chip surface. Then place the beker with NMP on sonicator for 3 min. Remove the wafer from NMP and immeidately place in IPA for 2 x 5 min. Again sonicate with P3.

Step 3: Top aluminium layer.
Spin resist LOR-5B at 5000 rpm on the topside of the wafer. Immediately bake for 3 minutes at 180 °C. On top spin a second layer of resist - AZ5214 at 6000 rpm. Bake 1 minute at 110 °C. Write the pattern for the top layer of the junctions in the Heidelberg µMLA with dose 117 mJ/cm^2. Use pneumatic focussing. Develop the resist in MF321 for 75 seconds. Rinse in demiwater for 2 times 30 seconds. Immediately blowdry when removing from water.

Load the sample in the Tepla for an O_2 descum for 2 min. Use 200 W and 200 sccm of O_2. Load the wafer into the Plassys. Once the Plassys is pumped vacuum, do an argon mill for 4 minutes. Use U = 400 V, I = 15 mA and $U_{\text{acceleration}}$ = 90 V. The sample now transfer to the oxidation chamber. Now oxidize the junction barrier at 30 mbar for 3:15 minutes. Next do a 20 nm titanium gethering of the oxidation chamber to lower the pressure. Deposit 40 nm of aluminium with rate 0.5 nm/s. Finish the process with an oxide capping layer

at 1.3 mbar for 11 minutes.

Place the wafer in NMP for overnight liftoff. Before removing from NMP, use a pipet to blow large aluminium flakes of the chip surface. Then place the beker with NMP on sonicator for 3 min. Remove the wafer from NMP and immeidately place in IPA for 2 x 5 min. Again sonicate with P3.

Step 4: Dicing the wafer.
Load the sample into the dicer. The wafer can now be diced in 4 x 8 mm DJJAA chips. The blade that was used in this process was 200 nm thick. Clean the resist of the DJJAA chips by placing in Acetone for 3 min and then in IPA for 3 min. Blow dry immediately after.

References

[1] Paul Benioff. “The computer as a physical system: A microscopic quantum mechanical Hamiltonian model of computers as represented by Turing machines”. In: Journal of statistical physics 22 (1980), pp. 563–591.

[2] Richard P Feynman. “Simulating physics with computers”. In: International Journal of Theoretical Physics. Springer, 1981, pp. 467–488.

[3] Tomi H Johnson, Stephen R Clark, and Dieter Jaksch. “What is a quantum simulator?” In: EPJ Quantum Technology 1.1 (2014), pp. 1–12.

[4] David Deutsch. “Quantum theory, the Church–Turing principle and the universal quantum computer”. In: Proceedings of the Royal Society of London. A. Mathematical and Physical Sciences 400.1818 (1985), pp. 97–117.

[5] Peter W Shor. “Algorithms for quantum computation: discrete logarithms and factoring”. In: Proceedings 35th annual symposium on foundations of computer science. Ieee. 1994, pp. 124–134.

[6] Daniel R Simon. “On the power of quantum computation”. In: SIAM journal on computing 26.5 (1997), pp. 1474–1483.

[7] Vikas Hassija et al. “Present landscape of quantum computing”. In: IET Quantum Communication 1.2 (2020), pp. 42–48.

[8] Ananda Roy and Michel Devoret. “Introduction to parametric amplification of quantum signals with Josephson circuits”. In: Comptes Rendus Physique 17.7 (2016), pp. 740–755.

[9] Aashish A Clerk et al. “Introduction to quantum noise, measurement, and amplification”. In: Reviews of Modern Physics 82.2 (2010), p. 1155.

[10] Kenneth Chang. Quantum Computing Advance Begins New Era, IBM Says. 2023. URL: `https://www.nytimes.com/2023/06/14/science/ibm-quantum-computing.html`.

[11] Michael Faraday. “XVII. On a peculiar class of acoustical figures; and on certain forms assumed by groups of particles upon vibrating elastic surfaces”. In: Philosophical transactions of the Royal Society of London 121 (1831), pp. 299–340.

[12] Brian Josephson. “Possible new effect in superconductive tunnelling”. In: Physics Letters 1.7 (1962), pp. 251–253.

[13] Richard Phillips Feynman, RB Leighton, and M Sands. The Feynman Lectures on Physics, Volume III: Quantum Mechanics. Basic Books, 1995. Chap. 21, pp. 578–610. ISBN: 978-0-465-02417-9.

[14] VV Sivak et al. “Kerr-free three-wave mixing in superconducting quantum circuits”. In: Physical Review Applied 11.5 (2019), p. 054060.

[15] Leonardo Ranzani et al. “Wideband Josephson parametric amplifier with integrated transmission line transformer”. In: 2022 IEEE International Conference on Quantum Computing and Engineering (QCE). IEEE. 2022, pp. 314–319.

[16] Manuel A Castellanos-Beltran et al. “Amplification and squeezing of quantum noise with a tunable Josephson metamaterial”. In: Nature Physics 4.12 (2008), pp. 929–931.

[17] TC White et al. “Traveling wave parametric amplifier with Josephson junctions using minimal resonator phase matching”. In: Applied Physics Letters 106.24 (2015), p. 242601.

[18] Patrick Winkel et al. “Nondegenerate parametric amplifiers based on dispersion-engineered josephson-junction arrays”. In: Physical Review Applied 13.2 (2020), p. 024015.

[19] F. Marquardt M. Aspelmeyer T. Kippenberg. “Cavity Optomechanics”. In: Reviews of modern physics (2014).

[20] Christopher Eichler and Andreas Wallraff. “Controlling the dynamic range of a Josephson parametric amplifier”. In: EPJ Quantum Technology 1.1 (2014), pp. 1–19.

[21] Xian Wu et al. “Overlap junctions for high coherence superconducting qubits”. In: Applied Physics Letters 111.3 (2017), p. 032602.

[22] Pim Duivestein. “Wafer scale fabrication of Josephson junctions”. PhD thesis. 2020.

[23] Mathijs de Jong. “Fabrication and characterization of Josephson parametric amplifiers”. PhD thesis. 2019.

[24] Jasper Franse. “Design and fabrication of a Josephson Parametric Amplifier based on nanobridge junctions”. PhD thesis. 2019.
[25] Stefanos Basili. “Development of Josephson Parametric Amplifiers for quantum applications”. PhD thesis. 2020.
[26] Wouter Wesselink. “Design and characterisation of an impedance engineered Josephson parametric amplifier”. PhD thesis. 2022.
[27] David M Pozar. Microwave engineering. John wiley & sons, 2011.
[28] Daniel Bothner. Resonator Response Functions. 2015.
[29] Digby D Macdonald. “Reflections on the history of electrochemical impedance spectroscopy”. In: Electrochimica Acta 51.8-9 (2006), pp. 1376–1388.
[30] Charles K Alexander. Fundamentals of electric circuits. McGraw-Hill, 2013, pp. 629–635.
[31] Iosif Demirtzioglou et al. “Frequency comb generation in a silicon ring resonator modulator”. In: Optics express 26.2 (2018), pp. 790–796.
[32] Oliver Heaviside. “XIX. On the extra current”. In: The London, Edinburgh, and Dublin Philosophical Magazine and Journal of Science 2.9 (1876), pp. 135–145.
[33] Dirk Van Delft and Peter Kes. “The discovery of superconductivity”. In: Physics Today 63.9 (2010), pp. 38–43.
[34] John Bardeen, Leon N Cooper, and John Robert Schrieffer. “Theory of superconductivity”. In: Physical review 108.5 (1957), p. 1175.
[35] Vitaly L Ginzburg and Lev D Landau. “On the theory of superconductivity”. In: On superconductivity and superfluidity. Springer, 2009, pp. 113–137.
[36] Michael Tinkham. Introduction to superconductivity. Courier Corporation, 2004.
[37] John Clarke and Alex I Braginski. The SQUID handbook. Vol. 1. Wiley Online Library, 2004.
[38] Fritz London and Heinz London. “The electromagnetic equations of the supraconductor”. In: Proceedings of the Royal Society of London. Series A-Mathematical and Physical Sciences 149.866 (1935), pp. 71–88.
[39] ED Reed. “The variable-capacitance parametric amplifier”. In: IRE Transactions on Electron Devices 6.2 (1959), pp. 216–224.
[40] National Institute of Informatics. Chapter 11 Parametric Amplifiers and Oscillator. last access 14 June 2023. URL: https://www.nii.ac.jp/qis/first-quantum/forStudents/lecture/pdf/noise/chapter11.pdf.
[41] Hermann A Haus and JA Mullen. “Quantum noise in linear amplifiers”. In: Physical Review 128.5 (1962), p. 2407.
[42] Carlton M Caves. “Quantum limits on noise in linear amplifiers”. In: Physical Review D 26.8 (1982), p. 1817.
[43] Archana Kamal, Adam Marblestone, and Michel Devoret. “Signal-to-pump back action and self-oscillation in double-pump Josephson parametric amplifier”. In: Physical Review B 79.18 (2009), p. 184301.
[44] Luca Planat et al. “Understanding the saturation power of Josephson parametric amplifiers made from SQUID arrays”. In: Physical Review Applied 11.3 (2019), p. 034014.
[45] Bogdan A Kochetov and Arkady Fedorov. “Higher-order nonlinear effects in a Josephson parametric amplifier”. In: Physical Review B 92.22 (2015), p. 224304.
[46] Gangqiang Liu et al. “Josephson parametric converter saturation and higher order effects”. In: Applied Physics Letters 111.20 (2017), p. 202603.
[47] Waltraut Wustmann and Vitaly Shumeiko. “Nondegenerate parametric resonance in a tunable superconducting cavity”. In: Physical Review Applied 8.2 (2017), p. 024018.
[48] VE Manucharyan et al. “Microwave bifurcation of a Josephson junction: Embedding-circuit requirements”. In: Physical Review B 76.1 (2007), p. 014524.
[49] Andreas Bengtsson et al. “Nondegenerate parametric oscillations in a tunable superconducting resonator”. In: Physical Review B 97.14 (2018), p. 144502.
[50] Zhaoyou Wang et al. “Quantum dynamics of a few-photon parametric oscillator”. In: Physical Review X 9.2 (2019), p. 021049.
[51] Thomas Weißl et al. “Kerr coefficients of plasma resonances in Josephson junction chains”. In: Physical Review B 92.10 (2015), p. 104508.
[52] Sami Franssila. Introduction to microfabrication. John Wiley & Sons, 2010.
[53] Yang Liu. “Novel Parylene Filters for Biomedical Applications”. PhD thesis. 2016.

[54] Per G Glöersen. “Ion- beam etching”. In: Journal of Vacuum Science and Technology 12.1 (1975), pp. 28–35.
[55] Lukas Grünhaupt et al. “An argon ion beam milling process for native AlOx layers enabling coherent superconducting contacts”. In: Applied Physics Letters 111.7 (2017), p. 072601.
[56] Vinay Ambegaokar and Alexis Baratoff. “Tunneling between superconductors”. In: Physical Review Letters 10.11 (1963), p. 486.
[57] Ioan Pop and Nicolas Zapata. DJJAA recipe. 2020.
[58] Patrick Winkel. DJJAA manual. unpublished. 2017.
[59] Kavli Nanolab. Temescal FC-2000. Last access 25 April 2023. 2023. URL: https://www.tudelft.nl/tnw/over-faculteit/afdelingen/quantum-nanoscience/kavli-nanolab-delft/equipment/deposition/temescal-fc-2000.
[60] LOR and PMGI Resists for Bilayer Lift-off Processing. Last access 9 June 2023. Kayaku Advanced Materials. URL: https://www.allresist.com/wp-content/uploads/sites/2/2020/03/AR-N4400_english_Allresist_product_information.pdf.
[61] AZ 5214 e Photoresist. Last access 4 June 2023. Merck Performance Materials GmbH. URL: https://www.microchemicals.com/micro/tds_az_5214e_photoresist.pdf.
[62] Kavli Nanolab. Heidelberg Instruments Laserwriter. Last access 25 April 2023. 2023. URL: https://www.tudelft.nl/tnw/over-faculteit/afdelingen/quantum-nanoscience/kavli-nanolab-delft/equipment/lithography/heidelberg-instruments-laserwriter.
[63] Kavli Nanolab. Tepla300. Last access 25 April 2023. 2023. URL: https://www.tudelft.nl/tnw/over-faculteit/afdelingen/quantum-nanoscience/kavli-nanolab-delft/equipment/dry-etching/tepla-300.
[64] Kavli Nanolab. Plassys. Last access 25 April 2023. 2023. URL: https://www.tudelft.nl/tnw/over-faculteit/afdelingen/quantum-nanoscience/kavli-nanolab-delft/equipment/deposition/plassys.
[65] AR-N 4400 photoresist series for high film thickness values. Last access 9 June 2023. Allresist GmbH. URL: https://www.allresist.com/wp-content/uploads/sites/2/2020/03/AR-N4400_english_Allresist_product_information.pdf.
[66] Kavli Nanolab. Bruker WLI. Last access 12 June 2023. 2023. URL: https://www.tudelft.nl/tnw/over-faculteit/afdelingen/quantum-nanoscience/kavli-nanolab-delft/equipment/inspection/bruker-wli.
[67] EPO-TEK H20E Technical Data Sheet. Rev. 18. Epoxy Technology, INC. Feb. 2021. URL: https://www.epotek.com/docs/en/Datasheet/H20E.pdf.
[68] Entropy Cryogenics. Cryostat with Sorption Unit. Last access 3 May 2023. 2023. URL: https://www.entropy-cryogenics.com/products/sorption/.
[69] Ananda Roy and Michel Devoret. “Quantum-limited parametric amplification with Josephson circuits in the regime of pump depletion”. In: Physical Review B 98.4 (2018), p. 045405.
[70] F Fani Sani et al. “Level attraction and idler resonance in a strongly driven Josephson cavity”. In: Physical Review Research 3.4 (2021), p. 043111.